

AD-A170 749

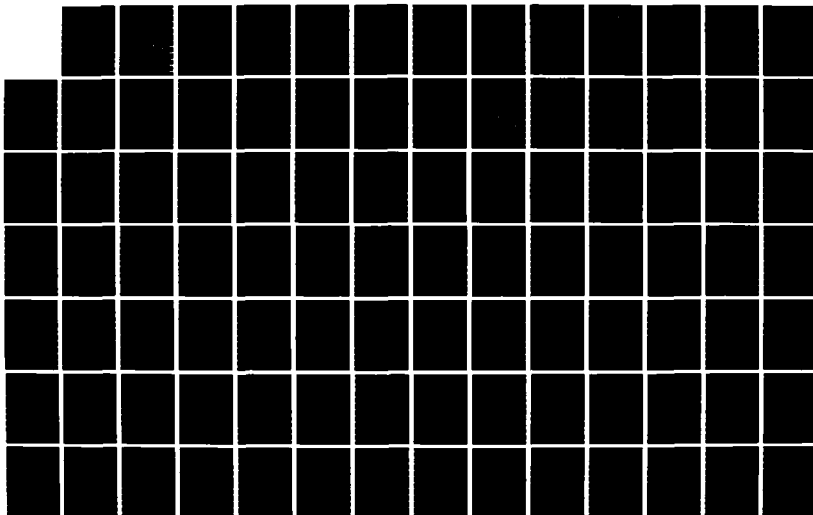
AIDED-AIRBORNE GRAVITY GRADIMETER SURVEY SYSTEM (GBSS) 1/2  
STUDY(U) ANALYTIC SCIENCES CORP READING MA  
S J BRZEZOWSKI ET AL. MAR 86 TASC-TR-4769-2

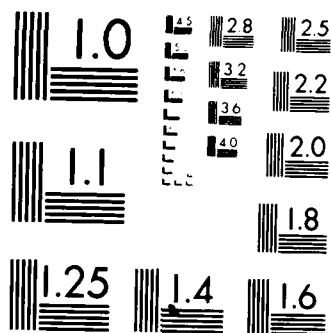
UNCLASSIFIED

AFGL-TR-86-0059 F19620-03-C-0146

F/G 17/7

NL





MICROCOPY RESOLUTION TEST CHART  
NATIONAL BUREAU OF STANDARDS 1963-A

AFGL-TR-86-0059

12

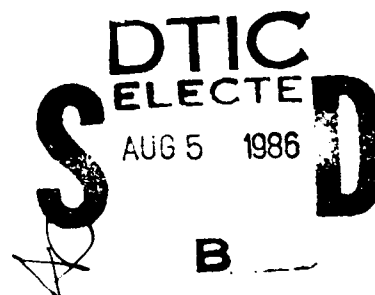
# AIDED-AIRBORNE GRAVITY GRADIOMETER SURVEY SYSTEM (GGSS) STUDY: FINAL REPORT

Steven J. Brzezowski  
Robert C. Merenyi

THE ANALYTIC SCIENCES CORP.  
One Jacob Way  
Reading, MA 01867

March 1986

Final Report  
September 1983 - September 1985



Approved for public release; distribution unlimited

Prepared for:  
AIR FORCE GEOPHYSICS LABORATORY  
AIR FORCE SYSTEMS COMMAND  
United States Air Force  
Hanscom Air Force Base, Massachusetts 01731

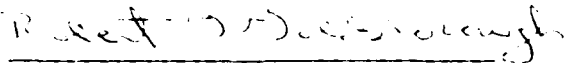
06 8 5 010

AD-A170 749

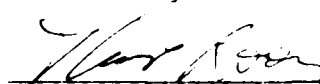
DTIC FILE COPY

The views and conclusions contained in this document are those of the authors, and should not be interpreted as representing the official policies, either expressed or implied, of the United States Government.

This technical report has been reviewed and is approved for publication.

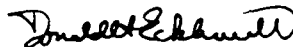


ROBERT G. GOLDSBOROUGH  
Contract Manager



THOMAS P. ROONEY, Chief  
Geodesy & Gravity Branch

FOR THE COMMANDER



DONALD H. ECKHARDT, Director  
Earth Sciences Division

This report has been reviewed by the ESD Public Affairs Office (PA) and is releasable to the National Technical Information Service (NTIS).

Qualified requestors may obtain additional copies from the Defense Technical Information Center. All others should apply to the National Technical Information Service.

If your address has changed, or if you wish to be removed from the mailing list, or if the addressee is no longer employed by your organization, please notify AFGL/DAA, Hanscom AFB, MA 01731-5000. This will assist us in maintaining a current mailing list.

Do not return copies of this report unless contractual obligations or notices on a specific document requires that it be returned.

UNCLASSIFIED

ADD 170749

SECURITY CLASSIFICATION OF THIS PAGE

## REPORT DOCUMENTATION PAGE

Form Approved  
OMB No. 0704-0188  
Exp. Date: Jun 30, 1986

1a. REPORT SECURITY CLASSIFICATION Unclassified			1b. RESTRICTIVE MARKINGS None	
2a. SECURITY CLASSIFICATION AUTHORITY N/A			3. DISTRIBUTION/AVAILABILITY OF REPORT Approved for Public Release; Distribution Unlimited	
2b. DECLASSIFICATION/DOWNGRADING SCHEDULE N/A				
4. PERFORMING ORGANIZATION REPORT NUMBER(S) TR-4769-2			5. MONITORING ORGANIZATION REPORT NUMBER(S) AFGL-TR-86-0059	
6a. NAME OF PERFORMING ORGANIZATION The Analytic Sciences Corp.		6b. OFFICE SYMBOL (If applicable)	7a. NAME OF MONITORING ORGANIZATION Air Force Geophysics Laboratory	
6c. ADDRESS (City, State, and ZIP Code) One Jacob Way Reading, MA 01867			7b. ADDRESS (City, State, and ZIP Code) Hanscom AFB MA 01731	
8a. NAME OF FUNDING/SPONSORING ORGANIZATION Defense Mapping Agency		8b. OFFICE SYMBOL (If applicable)	9. PROCUREMENT INSTRUMENT IDENTIFICATION NUMBER F19628-83-C-0146	
8c. ADDRESS (City, State, and ZIP Code) Washington, D.C. 20305			10. SOURCE OF FUNDING NUMBERS	
			PROGRAM ELEMENT NO 63701B	PROJECT NO 3204
11. TITLE (Include Security Classification) Aided-Airborne Gravity Gradiometer Survey System (GGSS) Study: Final Report				
12. PERSONAL AUTHOR(S) Steven J. Brzezowski and Robert C. Merenyi				
13a. TYPE OF REPORT Final		13b. TIME COVERED FROM 9/83 TO 9/85	14. DATE OF REPORT (Year, Month, Day) 1986 March	15. PAGE COUNT 136
16. SUPPLEMENTARY NOTATION				
17. COSATI CODES			18. SUBJECT TERMS (Continue on reverse if necessary and identify by block number) Gravity, Gravity Gradiometer, Gravity Gradiometer Survey System, GGSS, Global Positioning System, GPS, Radio Interferometry, Gravimeter, Master INS	
FIELD	GROUP	SUB-GROUP		
19. ABSTRACT (Continue on reverse if necessary and identify by block number) Several mechanization variants of the GGSS baseline configuration have been analyzed to assure an optimal and robust design and to establish confidence in the various navigation back-up modes. The analysis determined the current and anticipated performance of several sensors, individually and then in appropriate combination with the GGSS. Until more of the full Global Positioning System (GPS) constellation is in place, the currently planned precise reference clock and altimeter aides are capable of providing the increased visibility intervals and navigation accuracies required for GGSS airborne testing and initial survey operations. Moving-receiver radio interferometry to GPS is the most promising approach for satisfying the stringent navigation accuracies which may be required for GGSS surface testing. Furthermore, an improved measurement of gravity can be attained by augmenting a GGSS-aiding gravimeter with interferometrically derived position and velocity.				
20. DISTRIBUTION/AVAILABILITY OF ABSTRACT <input type="checkbox"/> UNCLASSIFIED/UNLIMITED <input checked="" type="checkbox"/> SAME AS RPT <input type="checkbox"/> DTIC USERS			21. ABSTRACT SECURITY CLASSIFICATION Unclassified	
22a. NAME OF RESPONSIBLE INDIVIDUAL Robert G. Goldsborough			22b. TELEPHONE (Include Area Code) 617-861-3486	22c. OFFICE SYMBOL LWG

## TABLE OF CONTENTS

	<u>Page</u>
List of Figures	v
List of Tables	vi
1. INTRODUCTION	1-1
1.1 GGSS Background	1-1
1.2 Study Objectives and Report Overview	1-2
2. CONVENTIONAL GPS-AIDING AND BACK-UP MODE ANALYSIS	2-1
2.1 System Description and GGSS Mechanization	2-1
2.1.1 GGSS Mechanization	2-2
2.1.2 GGSS Navigation Accuracy Requirements	2-3
2.2 Analysis Approach and Results	2-4
2.2.1 Approach	2-4
2.2.2 Six-Satellite Analysis Results	2-6
2.3 Technical Risk and Recommendations	2-9
2.3.1 Technical Risk	2-9
2.3.2 Recommendations	2-10
3. ANALYSIS OF MOVING-RECEIVER RADIO INTERFEROMETRY	3-1
3.1 System Description and Mechanization Details	3-1
3.1.1 Mechanization Details	3-3
3.1.2 Sensor Performance	3-4
3.2 Data-Reduction Approach	3-9
3.2.1 Interferometric Analysis	3-9
3.2.2 Doppler Analysis	3-10
3.3 Applicable Error Sources and Models	3-11
3.3.1 Environmental	3-12
3.3.2 Mechanical	3-14
3.3.3 Measurement	3-17
3.4 Analysis Results	3-19
3.4.1 Simulation Details	3-19
3.4.2 Results	3-21
3.4.3 Conclusions	3-31
3.5 Technical Risk and Recommendations	3-33
3.5.1 Technical Risk	3-33
3.5.2 Recommendations	3-34

## LIST OF TABLES

<u>Table</u>		<u>Page</u>
2.2-1	Summary of GPS Typical Coverage Which Will Occur During GGSS Testing	2-7
3.1-1	Capability of Available GPS Receivers to Support Moving-Receiver Radio Interferometry	3-7
3.1-2	Evaluation of Radio-Meteorological Sensors	3-8
3.3-1	Compilation of Moving-Receiver Radio Interferometry Error Sources	3-18
3.4-1	Nominal Scenario Details	3-21
3.4-2	Measurement Capability of Radio Interferometry	3-22
4.2-1	Red-Noise and White-Noise Parameters	4-9
4.2-2	Gravimeter-Aiding Analysis Results	4-13
5-1	Summary of Master INS Evaluation	5-1

1.

## INTRODUCTION

### 1.1 GGSS BACKGROUND

The Air Force Geophysics Laboratory (AFGL) and Defense Mapping Agency (DMA) are pursuing the development of a moving-base Gravity Gradiometer Survey System (GGSS). The GGSS will use gravity gradients to improve greatly our knowledge of the earth's gravity field and to increase significantly the rate at which we obtain that knowledge. Plans call for incorporation of this new gravity sensor in both a land vehicle and a fixed-wing aircraft. Surface testing is expected to commence in the spring of 1986; airborne testing in the fall. Following completion of flight testing, deployment of the GGSS for transitional test/survey operations will occur immediately.

Updates from the Global Positioning System (GPS) will be used in the aircraft application to augment the positions which are derived from the sensor outputs of the GGSS inertial platform. Since there is a potential for significant misregistration during surface testing, updates from wayside position markers and/or a fifth wheel are being considered by Bell Aerospace. An overview of the currently configured GGSS is presented in Fig. 1.1-1. This overview also indicates the two GPS back-up modes which are a part of the baseline GGSS configuration. The first back-up mode is initiated when only three satellites are visible. In this case, incorporation of an atomic clock allows the full navigation solution (i.e., three positions and time) to be computed. The second back-up mode, which involves the use of both an atomic clock and altimeter, will be called upon when only two GPS satellites are in view.



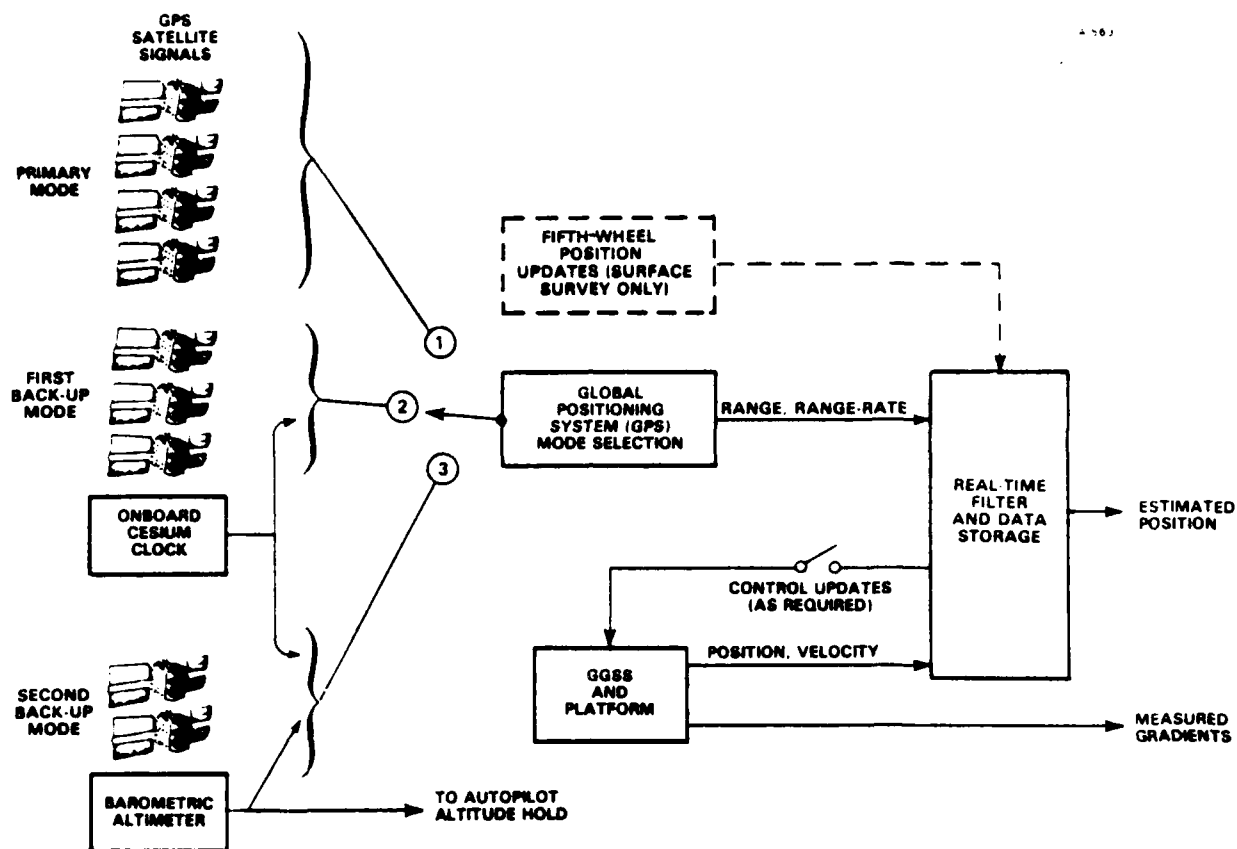


Figure 1.1-1 Baseline GGSS/External Reference Configuration

## 1.2 STUDY OBJECTIVES AND REPORT OVERVIEW

The primary objective of this study is to identify and analyze navigation system configurations which are most appropriate for assuring the immediate and long-range success of the surface and airborne GGSS applications. To accomplish this objective, alternative gravity- and navigation-aided subsystems are investigated; current and anticipated accuracies appropriate to each subsystem are determined; and the resulting accuracy and other benefits which would accrue from using these aides with the GGSS are assessed. The following intermediate study objectives are also addressed:

- Review sensor technology
- Formulate appropriate error models
- Examine relevant mechanization issues
- Calculate resulting benefits (in particular, accuracy improvement)
- Identify technical factors to be overcome
- Recommend areas which merit further research.

Four classes of survey aides are evaluated in this study in terms of their ability to provide significant accuracy improvement compared with the unaided GGSS. The first is conventional GPS and its associated back-up modes (Chapter 2). The second involves radio interferometry using GPS signals and a separate GPS receiver, atomic clock, weather sensor, and data recorder at a convenient fixed location (Chapter 3). The third is a gravimeter which provides an additional (and unique) gravity measurement (Chapter 4). The fourth is a master inertial navigation system (INS) which provides higher accuracy than the GGSS' stabilized platform components can provide (Chapter 5). A diagram illustrating the use of these sensors as GGSS aides is presented in Fig. 1.2-1.

Chapter 5 summarizes only the key master INS analysis results; the complete technical details are presented in Ref. 1. The significant conclusions of the aided-airborne study and recommendations of areas to be pursued further are presented in Chapter 6. Additional support material and methodologies requiring extensive theoretical development are presented in separate appendices. Appendix A contains a GPS description and discussion of anticipated navigation accuracies in support of operational surveying with the GGSS; Appendix B presents a derivation of the doppler-shift observable, an important

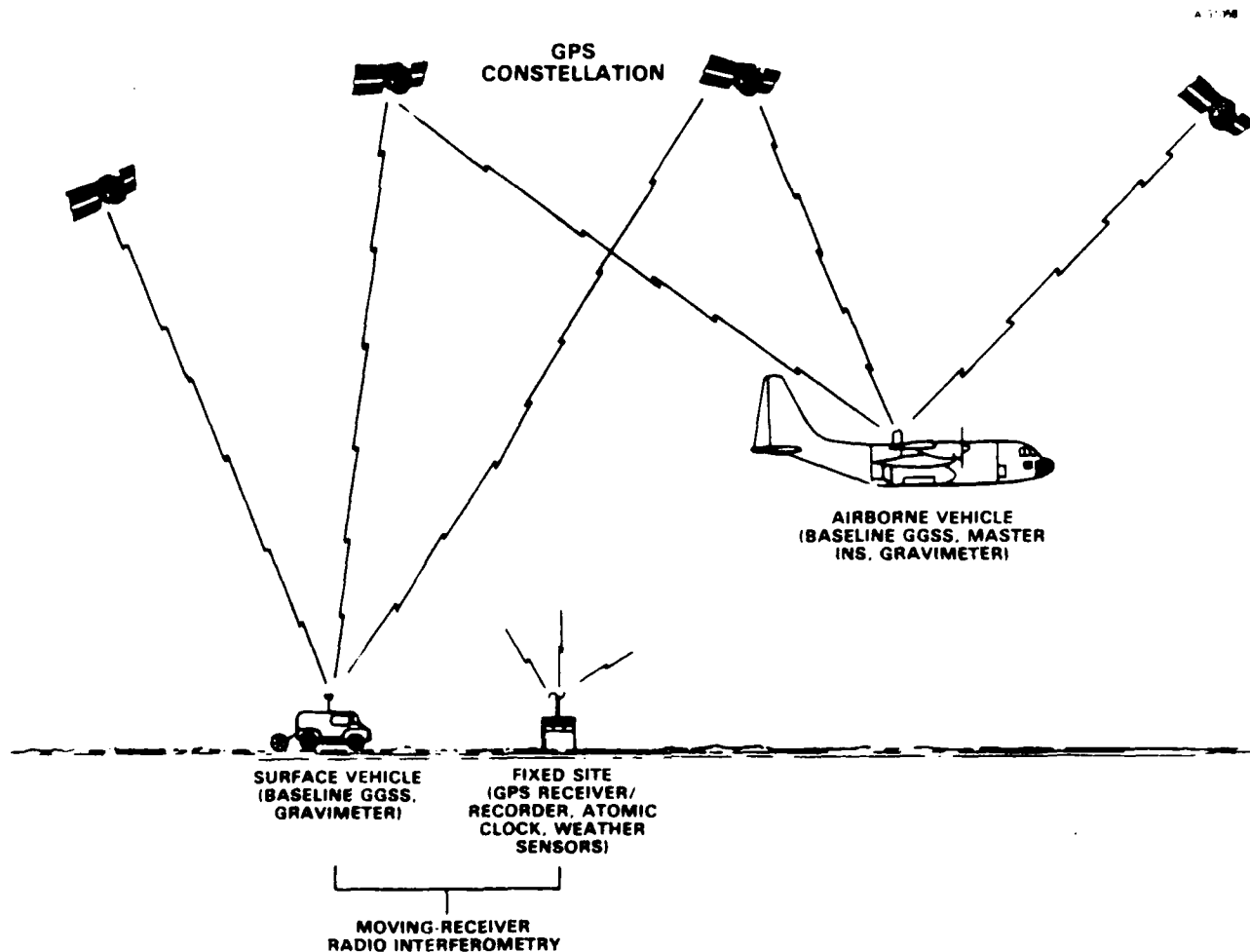


Figure 1.2-1 Aiding Sensors for the GGSS  
(Conceptual Overview)

measurement for moving-receiver radio interferometry to GPS; Appendix C discusses atmospheric signal propagation delay, a significant error source in applications of radio interferometry; and Appendix D presents the state-space representation of a third-order Markov process which is used for atmospheric refractivity modeling.

2.

CONVENTIONAL GPS-AIDING AND BACK-UP  
MODE ANALYSIS

The NAVSTAR Global Positioning System (GPS) is a satellite-based, all-weather, continuous radio navigation system that provides accurate position, velocity, and time information to users anywhere on or near the earth's surface. When the entire 18-satellite constellation is in place and operational (late 1988), conventional pseudoranging techniques are more than adequate for supporting operational GGSS missions. As a minimum configuration, the current constellation of six satellites will be maintained throughout the airborne GGSS test operations scheduled for the fall of 1986. Despite the limited viewing times associated with this current constellation, accurate position-fixing and long-distance navigation using GPS have been demonstrated successfully (Ref. 2). For the GGSS application, satisfactory GPS-aiding performance will be realized during testing through the use of two back-up modes. The first back-up mode involves incorporating an atomic clock; the second involves adding a clock and altimeter. The back-up modes are necessary to extend the intervals of usable GPS coverage (two or more satellites in a favorable orientation) to a sufficient amount for GGSS test sorties.

2.1 SYSTEM DESCRIPTION AND GGSS MECHANIZATION

GPS consists of three major segments: 1) a space segment containing satellites which transmit radio signals; 2) a control segment made up of ground-based equipment to monitor the satellites; and 3) a user segment comprising

equipment which passively receives and converts the satellite-transmitted signals into positioning and navigation information. The first and third segments are most relevant for this analysis and are discussed further in Appendix A. Additional details are presented in Refs. 3-6.

### 2.1.1 GGSS Mechanization

As currently configured, the GGSS includes a TI 4100 GPS Navigator, an atomic clock, and a barometric altimeter (see Fig. 1.1-1). This equipment makes possible the use of the GPS back-up modes when only three or two satellites are visible during GGSS testing and initial survey operations. A ROLM MSE-14 militarized computer controls the real-time data flow and processing associated with the GGSS. A brief description of the TI 4100 Navigator is presented below, followed by a discussion of the navigation accuracies required for the airborne GGSS application.

The TI 4100 NAVSTAR Navigator consists of an antenna assembly, a receiver, and a control/display unit. The antenna accommodates an omnidirectional pattern and can receive both the  $L_1$  and  $L_2$  GPS frequencies\*. The receiver is designed to process the signals from any four visible GPS satellites and can operate in a "degraded" navigation and positioning mode when a user indicates that only three or two satellites are visible. The unique single-channel hardware multiplexing feature of this receiver allows the  $L_1$  and  $L_2$  signals of up to four satellites to be sampled within each 20 msec interval. In a sampled data sense, all the satellite signals are tracked continuously as though multiple hardware receiver channels are present and thus, interchannel measurement bias is avoided.

---

\*GPS transmits on two carrier frequencies, denoted  $L_1$  and  $L_2$ .

These frequencies are 1575.42 MHz and 1227.60 MHz, respectively.

The output data provided by the TI 4100 receiver include the following:

- $L_1$  and  $L_2$  P-code state (pseudorange)
- $L_1$  and  $L_2$  pseudorange-rate (P-code)
- $L_1$  and  $L_2$  (doppler-induced) carrier phase (whole cycles and fractions)
- Instantaneous  $L_1$  and  $L_2$  doppler frequency shift
- Averaged line-of-sight satellite acceleration
- $L_1$  C/A-code state (pseudorange)
- $L_1$  pseudorange-rate (C/A-code)
- Signal-to-noise measures and other data quality indicators.

These data are provided simultaneously for four satellites at three-second intervals. Additional characteristics and attributes of the TI 4100 are presented in Ref. 7; a comparison of the characteristics, capabilities, and performance of several GPS receivers currently available is provided in Refs. 8 and 9.

#### 2.1.2 GGSS Navigation Accuracy Requirements

The core of the GGSS mechanization consists of three gravity gradiometer instruments (GGIs) mounted on a three-axis platform equipped with inertial sensors (gyros and accelerometers) to provide local-level stabilization. This mechanization is depicted in Fig. 2.1-1. Extraction of precise gravity gradients requires 1) accurate positioning and 2) known orientation of each GGI. These requirements levy performance constraints on the inertial platform to maintain misregistration and misresolution at acceptable levels. Of particular interest in this discussion is the adequacy of the planned primary and back-up positioning

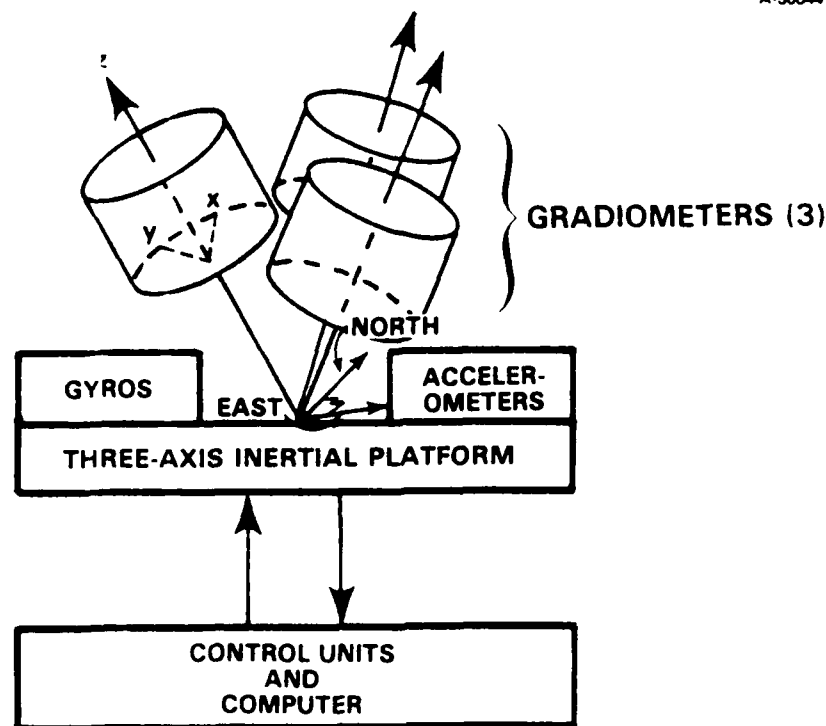


Figure 2.1-1 Schematic of Inertially Stabilized Moving-Base GGSS

system in the presence of misregistration due to navigational position errors (i.e., measured gradients assigned to the wrong location on the surface of the earth). Based on previously derived misregistration sensitivities for an airborne GGSS survey (Ref. 10), navigation accuracies near 100 m rms are required to avoid introducing significant gradient misregistration. The discussion which follows quantifies the capability of conventional GPS-aiding (both primary and back-up modes) to satisfy this navigation accuracy requirement.

## 2.2 ANALYSIS APPROACH AND RESULTS

### 2.2.1 Approach

The analysis approach described herein is based on a simulation of the applicable GPS constellation. Both the planned

18-satellite and the current 6-satellite configurations are considered. The technical details associated with simulating a particular constellation are included in Appendix A. The discussion in this section emphasizes the following two points: 1) quantifying the number of GPS satellite signals which will be available and visible to the airborne GGSS based on the orbital relationships introduced in Appendix A, and 2) assessing the associated measurement geometry and resultant GGSS positioning accuracy.

Signal availability for radio communications systems generally involves consideration of transmitting power levels, transmitting antenna patterns, the distance from transmitter to receiver, interference effects, receiver antenna gains, etc. For near-earth GPS users, in particular for the GGSS, most of these factors are not applicable (Ref. 11). GPS satellite orbits are so high above the earth that differences in transmitter-to-receiver distance are very slight for near-earth users. Transmitting antenna beamwidth is adequate to cover the entire near-earth region in the main lobe. GPS signals, having wavelengths of about 19 cm at the  $L_1$  frequency, travel in a line-of-sight fashion and are blocked by objects having dimensions comparable to a wavelength or larger (e.g., the earth itself or other obstructions near the receiving antenna). Transmitting power levels and processing gains are such that C/A-code acquisition will be possible for any signal coming from a GPS satellite visible to any part of the receiving antenna pattern with a gain of about -4 dB or more. Thus, GPS signal availability for the GGSS is equivalent to satellite visibility.

There are four factors generally involved in satellite visibility:



- The GPS satellite constellation, i.e., the number of operational in-orbit satellites and their orbit relationships
- The GGSS host aircraft flight pattern details
- The earth as a signal block
- The receiving antenna coverage.

The significance of each of these factors is discussed in Appendix A, along with the navigation and positioning accuracies anticipated from the complete 18-satellite GPS constellation. Key analysis results for the six-satellite constellation are described in the pages which follow.

#### 2.2.2 Six-Satellite Analysis Results

As pointed out in Appendix A, it is anticipated that the GPS constellation will consist of only six satellites during airborne GGSS testing scheduled for the fall of 1986. This condition has major implications on the satellite visibility patterns which will occur for the GGSS tests in North Texas. Figure 2.2-1 illustrates a typical coverage pattern which will exist for North Texas during a fall 1986 day. Since the satellites appear about four minutes earlier in the sky each day, the times of adequate visibility will shift accordingly, (e.g., from early morning to late evening of the previous day, etc), but the amount of continuous coverage will not change appreciably.

Table 2.2-1 quantifies the length of continuous coverage associated with the case shown in Fig. 2.2-1. The actual length of usable coverage (i.e., suitable for satisfying the GGSS navigation rms accuracy goal of 100 m) is determined by examining the geometry associated with both the nominal and aiding solutions (see Fig. 2.2-2). The aiding solution is

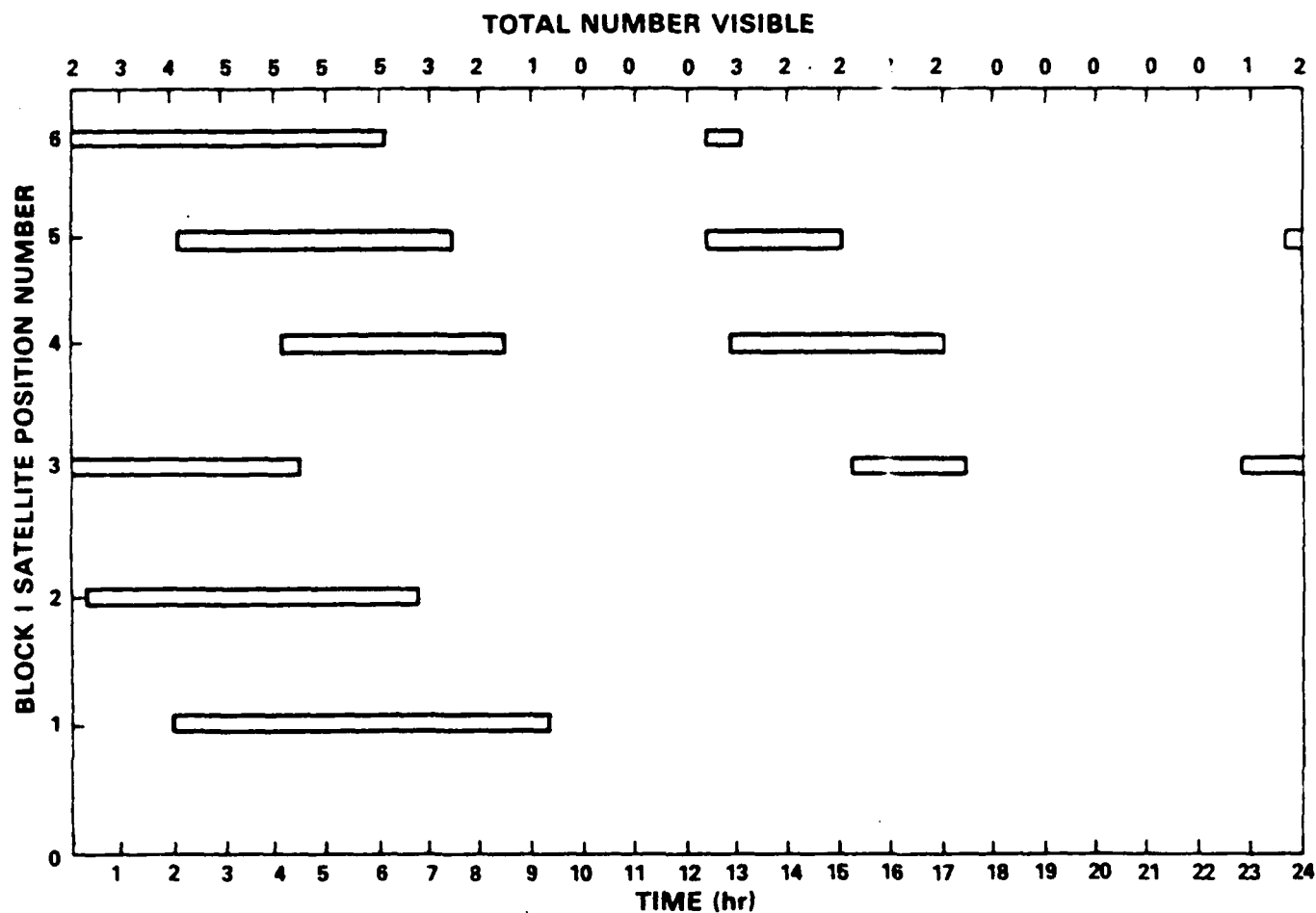


Figure 2.2-1 Predicted GPS Coverage for North Texas During a Typical Fall 1986 Day

TABLE 2.2-1  
SUMMARY OF GPS TYPICAL COVERAGE WHICH  
WILL OCCUR DURING GGSS TESTING\*

MINIMUM NUMBER OF VISIBLE SATELLITES	HOURS OF CONTINUOUS COVERAGE (PRIMARY/SECONDARY INTERVALS)
4	4.8/0.0
3	7.0, 0.2
2	8.5, 4.5

\*When only six satellites are available.

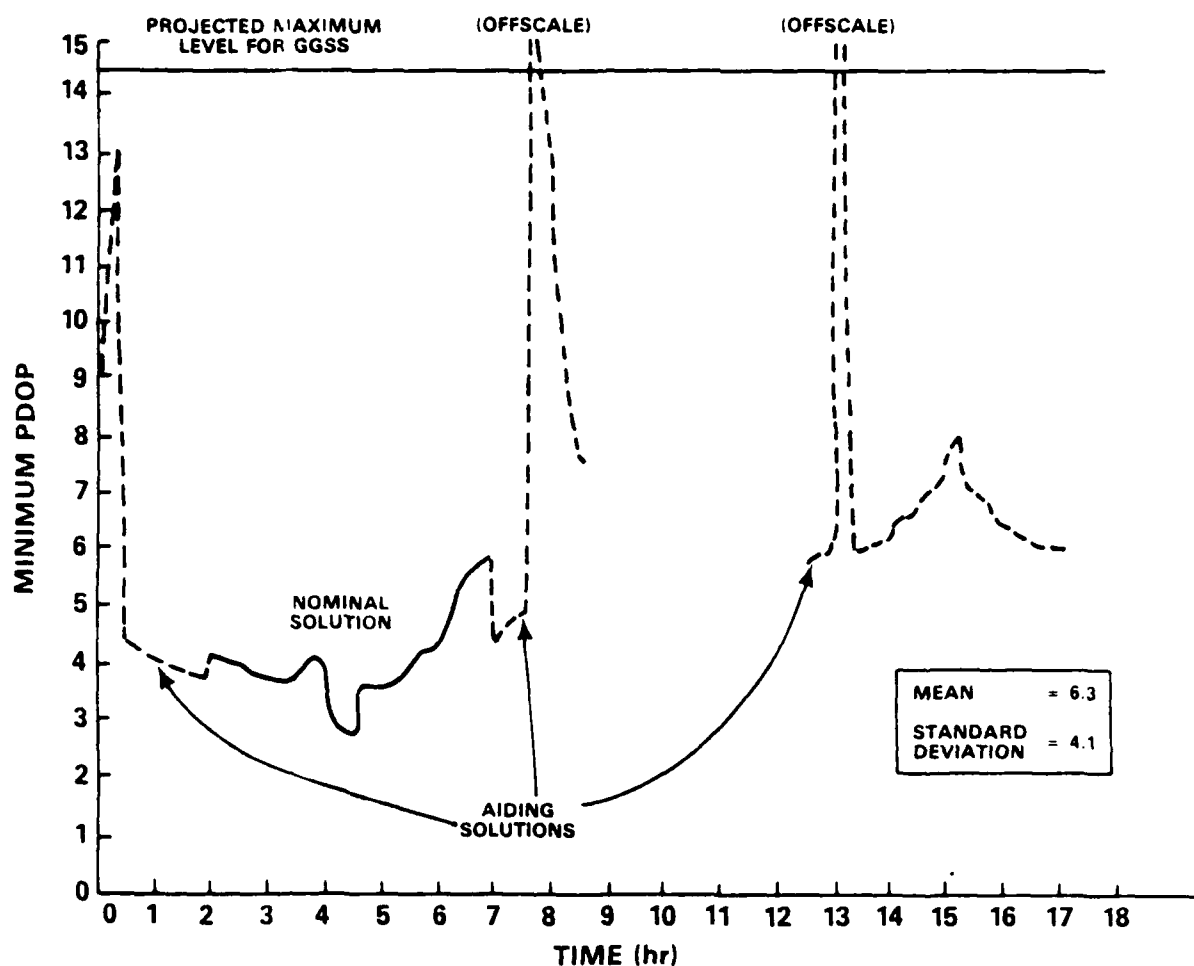


Figure 2.2-2 PDOP Characteristics Associated with Predicted GPS Coverage During GGSS Testing

accomplished using an atomic clock and barometric altimeter whose outputs are two and five times, respectively, less accurate than the corresponding quantities which would be derived from the nominal GPS solution if four satellites were visible. Aiding with a sufficiently accurate atomic clock extends the usable coverage by about 55%. Similarly, aiding with a sufficiently accurate clock and altimeter provides an additional 24% of coverage during the primary interval (hours 0 to 12 in Fig. 2.2-1) for a total of about 8.5 hours. This length of

time is adequate for completing a daily 50-km by 50-km test sortie at 400 km/hr. In fact, four additional hours of adequate navigation are possible by exploiting the secondary interval of GPS coverage (hours 12 to 24 in Fig. 2.2-1). Note that for a typical flight pattern, such as that described in Appendix A (Fig. A.3-1), 7.5 min are needed to fly each data track and thus, 2.75 hr are required to collect all the data. The remainder of the available time can be expended in the turns and travel to and from the calibration site.

Also apparent in Fig. 2.2-2 are two relatively short (e.g., less than 10 min) intervals when the PDOP exceeds the projected maximum value for the airborne GGSS application. Recall from Appendix A (Eq. A.1-3) that the maximum PDOP value is obtained by dividing the three-dimensional GGSS rms position error goal (100 m) by the rms pseudorange error (7 m). Both of these intervals of unfavorable geometry are associated with the aiding solutions and occur near the end or beginning of the visibility regions. Since these intervals are predictable, the GGSS testing schedule can be established to appropriately avoid them, as necessary. In addition, note that the GGSS inertial platform is capable of providing about 5 min of adequate unaided operation (Ref. 1).

## 2.3 TECHNICAL RISK AND RECOMMENDATIONS

### 2.3.1 Technical Risk

Conventional pseudoranging to the NAVSTAR GPS will provide the currently configured airborne GGSS with adequate navigation and positioning information during testing and future survey operations. Nevertheless, some technical and program risk is still associated with GPS. The key risk is

that GPS is not yet fully operational. Fifteen of the planned satellites must still be fabricated, launched, and placed in the proper orbit. Furthermore, these satellites must remain operational as long as expected (recall that clock problems contributed to the failure of an early satellite) and the position of their orbits must be known precisely. Clock stability and ephemeris prediction error sources are the major contributors to the computed user-to-satellite rms ranging error of seven meters rms.

Another area of risk is the current status of GPS user equipment in particular the receiver technology. Although the TI 4100 receiver has been tested successfully on numerous occasions (Refs. 7, 9, and 12), this technology is relatively new and additional tests, particularly in the two- and three-satellite "backup modes", are in order (see below).

### 2.3.2 Recommendations

Based on the analysis results presented herein and published material, the GGSS Program can confidently proceed with its planned use of conventional GPS-aiding. However, to assure successful GGSS testing, mechanization of the three-satellite and two-satellite back-up modes is exceedingly important. In addition, to minimize the risk associated with the TI 4100 receiver, extensive testing (especially in a dynamic environment and in the degraded modes) is needed to fully understand the performance of the receiver hardware and associated software. Finally, in anticipation of more stringent navigation and positioning requirements for the GGSS in surface vehicle applications, differential GPS techniques should be investigated.

3.

### ANALYSIS OF MOVING-RECEIVER RADIO INTERFEROMETRY

Radio interferometry uses to advantage the wave-like nature of radio waves to measure accurately the propagation path length differences of two radio signals transmitted from the same source. The application of doppler-shift and interferometric phase analysis to GPS data collected in a moving-receiver scenario will yield positioning accuracies of a few parts per million (ppm) for geodetic ground surveys and tens of ppm for airborne surveys. Thus, radio interferometry offers a more than adequate backup positioning capability during GGSS testing and survey operations. The potential for measuring acceleration to better than one milligal accuracy for surface vehicle applications is also attractive.

Data for radio interferometer-based measurements are obtained by employing the NAVSTAR carrier frequencies and thus, no access to the GPS codes is required. In addition, the GPS receiver included in the nominal GGSS configuration is uniquely qualified to provide the appropriate data. Radio-meteorological sensors and minor modifications to the current GGSS test plan are necessary for system implementation. The very accurate distance and velocity measurements possible using interferometry can also be used to augment a gravimeter-aided GGSS (see Chapter 4), thereby realizing a more accurate measure of gravity. The following sections explicitly address TASC's analysis of moving-receiver radio interferometry.

#### 3.1 SYSTEM DESCRIPTION AND MECHANIZATION DETAILS

Very high accuracies have been demonstrated repeatedly during the measurement of fixed inter-receiver distances using

GPS-based radio interferometry. Phase observations recorded during geodetic surveys have resulted in accuracies of one ppm (or better) for relative distances up to several thousand kilometers (Refs. 13-15). However, the application of radio interferometry to a moving-receiver scenario is a new area of research. TASC's findings indicate that this new measurement technique holds promise for the GGSS program as well as the entire field of geodesy.

The use of radio interferometry in a dynamic environment is illustrated in Fig. 3.1-1. At both receiver locations, periodically synchronized atomic clocks are used to time mark the GPS signal phase and doppler-shift observations for subsequent post-mission data reduction. In addition to generating very accurate position data in support of geodetic survey missions, this system can serve to supplement post-mission reduction of

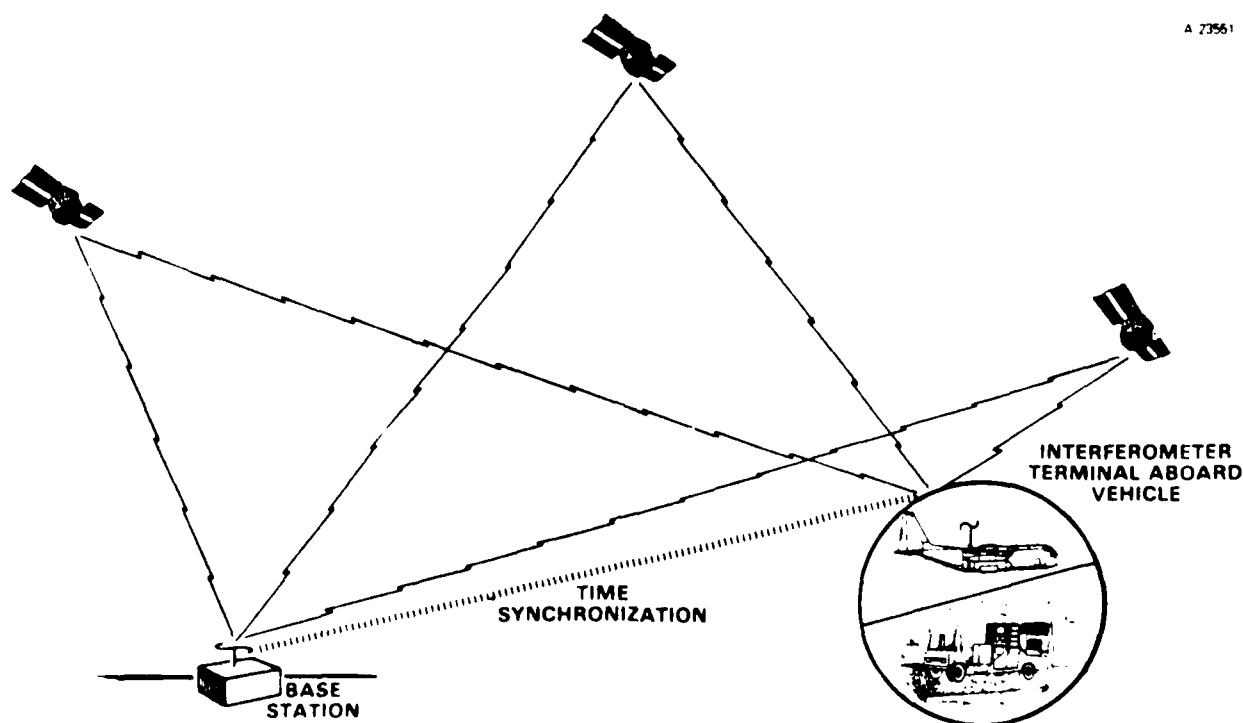


Figure 3.1-1 Summary of Moving-Receiver Radio Interferometry Concept

host vehicle inertial navigation system (INS) data by providing an accurate external velocity reference. Furthermore, by subtracting host vehicle INS<sup>\*</sup> and interferometrically derived accelerations, one can obtain a measurement of gravity. This is theoretically appealing since the accelerometers in the INS actually measure only the difference between vehicle and gravitational accelerations whereas, using interferometry, vehicle accelerations can be measured directly. Analysis results, presented in Section 3.4.2, quantify the accuracy associated with the measurement of these navigation quantities.

### 3.1.1 Mechanization Details

This section addresses the minor modifications to the GGSS mechanization which are required for radio interferometry to provide an appropriate backup positioning capability during GGSS test and survey operations. Depending on the nature of the gravity field, misregistration sensitivity studies indicate that positioning accuracies near 10 m rms may be needed for gravity surveys performed aboard a surface vehicle (Ref. 10). Until appropriate testing procedures are carried out (e.g., Ref. 16) and the collected data are analyzed, this stringent accuracy requirement cannot be confirmed. However, as noted in Section 2.2 and Appendix A (Section A.3), positioning accuracies near 10 m rms will be difficult to attain using standard GPS pseudorange techniques. For these reasons, Bell Aerospace and TASC have considered alternative mechanizations for the surface vehicle implementation. Note that this issue is not important for airborne scenarios in which positioning accuracies near 100 m rms are needed (Ref. 10). Accuracy of 100 m is achievable with the nominal mechanization (Sections 2.2 and A.3).

---

\*Inertial Navigation System.



Bell Aerospace has responded to the possible need for high positioning accuracy during surface applications of the GGSS by incorporating a "fifth-wheel" dead-reckoning mechanization to the surface vehicle design. However, uncertainties remain in the fifth-wheel approach, particularly in regard to the treatment of cross-track errors.

As an alternative back-up approach, TASC examined the use of GPS-based radio interferometry. This positioning system requires modest augmentation of the current GGSS/GPS mechanization. TASC's analysis examined the ability of an interferometry-aided GGSS to provide improved positioning accuracies and more precise gravity disturbance measurements, compared with the nominal GGSS mechanization discussed earlier in this report.

The present GGSS baseline configuration already includes a GPS receiver, atomic clock, and data recording system. Thus, the only new hardware needed at the moving receiver would be a radio-meteorological sensor to determine atmospheric refractivity variations on a continuous basis. In addition, an appropriate GPS receiver, data recording system, refractivity sensor, and atomic clock would be required at a fixed-site location.

### 3.1.2 Sensor Performance

The performance of any system depends on the accuracy of its constituent sensors. For radio interferometry, the necessary equipment consists of GPS receivers and atmospheric refractivity monitors. The dynamic environment further constrains hardware to be rugged and capable of maintaining calibration for the duration of a survey sortie (i.e., up to 8 hours). These constraints limit the equipment available to support applications of moving-receiver radio interferometry.

GPS Receivers - The receiver is required to track the carrier frequency of multiple satellites in a dynamic environment; i.e., the receiver used must maintain GPS signal tracking through doppler shifts. As a result, the hardware chosen must have a wide-band input channel. Neither the SERIES-ISTAC receivers, models 1991 and 2002 (Ref. 17), nor the Macro-meter receivers, models V-1000 and II (Ref. 18) are capable of this since both are designed as stationary, narrow-band receivers.

The primary requirement of a GPS receiver for moving-receiver radio interferometry is to maintain sufficient phase accuracy. Current technology dictates that this requirement can only be satisfied by employing a single-channel multiplexing design. Multichannel receivers, such as the SERCEL TR 55 or the Wild-Magnavox WM-101, produce phase delay differences for each hardware channel due to the different electrical paths encountered by each satellite signal. Attempts have been made to compensate for these errors; however, these compensations are still incapable of delivering the high accuracy required for geodetic survey applications (Ref. 7).

The Texas Instruments TI 4100 GPS receiver, presently configured for the baseline GGSS system, is uniquely qualified to support applications of moving-receiver interferometry. The TI 4100 is the only receiver currently designed with single-channel multiplexing. This capability allows both the GPS  $L_1$  (1.5754 GHz) and  $L_2$  (1.2276 GHz) frequency signals of up to four satellites to be sampled within each 20-msec interval (Ref. 7). In addition, this receiver is designed with a 48-bit software accumulator, sufficient to retain the temporal relationship between carrier phase and time, as measured by a local clock for an entire satellite pass. The accumulated phase (whole cycle and fraction) is provided to the user at 0.0- and 1.2-second intervals via a 9600-baud RS-232 port. The

phase is derived with respect to either the internal receiver oscillator (with 20-nsec accuracy) or an external user-supplied clock which can augment the receiver. (The time can also be recorded along with the signal phase for post-mission processing.) In one demonstration conducted by the Geodetic Survey Division, Surveys and Mapping Branch of Energy, Mines, and Resources of Canada, recorded phase observations from two TI 4100s were used to recover inter-receiver distances up to 102 km in length with accuracies of one ppm in all three coordinates (Ref. 19).

In addition, the TI 4100 outputs the "instantaneous" doppler frequency shift observed for each satellite signal. This measurement is the result of endpoint averaging two frequency shifts 160 msec apart for both the  $L_1$  and  $L_2$  signals. Recording of both the phase and doppler-shift outputs from the TI 4100 can be readily accomplished using the planned 16 or 0.5 Hz sampling rate of the GGSS data acquisition and monitoring system. A summary of the attributes and limitations of the receivers reviewed for this study is presented in Table 3.1-1.

Atmospheric Monitors - The largest source of error for interferometrically derived quantities is due to signal delay in the troposphere. In order to measure inter-receiver distances using radio interferometry, the time delay between the receipt of the same signal at two separate receivers must be recorded. This time delay (which causes the receivers to be "out of phase" with each other) is affected by the differing refractive properties of the atmosphere along the radio path at the two receiver locations.

Atmospheric refractivity is influenced by both electromagnetic conditions in the ionosphere and meteorological conditions in the troposphere. (These affects are described

TABLE 3.1-1  
CAPABILITY OF AVAILABLE GPS RECEIVERS  
TO SUPPORT MOVING-RECEIVER RADIO INTERFEROMETRY

RECEIVER	ATTRIBUTES	LIMITATIONS
ISTAC-SERIES (1991 & 2002)	Codeless, lightweight	Narrow bandwidth, stationary applications
Macrometer (V-1000 & II)	Six-satellite tracking, codeless	Narrow bandwidth, stationary applications
SERCEL TR 55 Wild-Magnavox WM-101	} Accurate dynamic positioning via codes	Multiple hardware channels, limited test results
Texas Instruments TI 4100	Single-channel multiplexing, dynamic environment design, two- and three-satellite degraded mode design	Limited test results

in Appendix C.) Refractivity is measured in N-units which are defined as

$$N = (c/v - 1) \times 10^6 \quad (3.1-1)$$

where  $c$ , the vacuum speed of light, is  $2.9978 \times 10^8$  m/sec and  $v$  is the atmospheric (refracted) speed of light. Thus, a change of one N-unit corresponds to a nanosecond delay for typical atmospheric signal paths (i.e. about 60 km of troposphere). Measurement of, and correction for, atmospheric propagation delays are described in Appendix C.

Ionospheric delays can be compensated by modeling the upper atmosphere or by using dual-frequency radio receivers. The former approach reduces signal delays by 50 to 70 percent (on an rms basis) compared with uncorrected measurements; dual-frequency receivers reduce signal delays by better than 40 percent on an rms basis.

Tropospheric refractivity can be measured using three different atmospheric sensors (i.e., radiosondes, refractometers, and radiometers). Radiosondes, generally employed for weather forecasting, have limited sensitivity and slow response to the varying atmospheric conditions expected during applications of moving-receiver interferometry. Microwave refractometers measure changes in cavity resonance and are most frequently used to record refractivity. Radiometers measure thermal atmospheric emission and have only recently been developed and tested for recording line-of-sight propagation delay times. Although still in an experimental stage, portable radiometers are expected soon.

The three radio-meteorological sensors examined for use in moving-receiver radio interferometry are listed in Table 3.1-2. Subsequent analysis results which are reported herein reflect the availability of refractometers to monitor atmospheric variations.

TABLE 3.1-2  
EVALUATION OF RADIO-METEOROLOGICAL SENSORS

SENSOR FAMILY	PROPERTY MEASURED	LIMITATION	RMS ACCURACY (N-UNITS)
Weather radiosonde	Air pressure, humidity, temperature	Slow response to refractivity variations	1.0
Refractometer	Refractivity variations	Initial calibration required	0.01
Dual-frequency radiometer	H <sub>2</sub> O thermal atmospheric emission at 22.2 and 31.4 GHz	Still in experimental stage, not portable	0.0001

## 3.2 DATA-REDUCTION APPROACH

### 3.2.1 Interferometric Analysis

Radio interferometry requires recording of the time delay between the receipt of the same signal at two separate receivers (see Fig. 3.2-1). The time delay determines the amount of phase retardation present between receivers; i.e., at a given instant in time, how many carrier cycles exist between the two receivers. This observed phase difference,  $\Delta\phi$ , can be related to the perpendicular distance,  $d$ , from the moving receiver to the signal wavefront plane through the equation

$$d = c\Delta\phi/(nf) \quad (3.2-1)$$

where  $f$  is the GPS  $L_1$  signal carrier frequency (1.5754 GHz) and  $n$  is the index of refraction. A subsequent measurement of the phase difference reveals a new value for  $d$  and yields the GPS signal plane's angle of incidence,  $\theta$ , with respect to the

A-31070

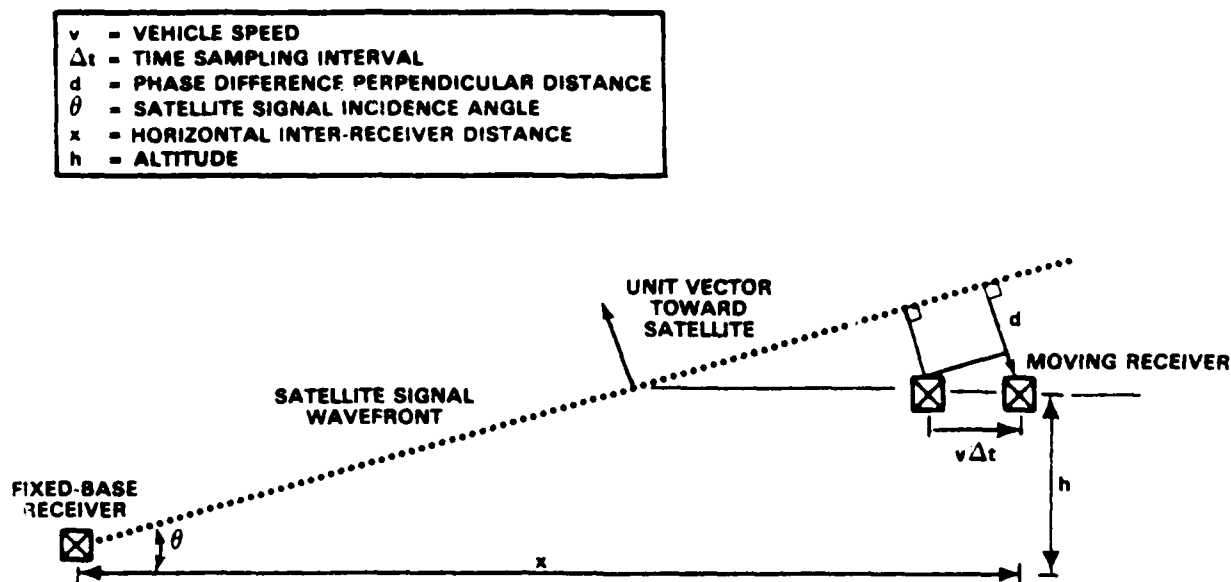


Figure 3.2-1 Overview of Interferometric Phase-Difference Geometry in Two Dimensions

vehicle's direction of motion. The motion is expressed as a function of vehicle velocity,  $v$ , and time between phase measurements,  $t$ . By employing three or more satellites from the GPS constellation, the inter-receiver distance can be uniquely determined (within a constant ambiguity resolved through proper initialization).

The horizontal inter-receiver distance,  $x$ , can be related to the phase difference through  $d$  and the equation

$$x = (h/\tan\theta) + (d/\sin\theta)$$

which is the equivalent to

$$x = (nfh\cos\theta + c\Delta\phi)/(nf\sin\theta) \quad (3.2-2)$$

where  $h$  is the survey vehicle altitude. In terms of  $\Delta\phi$ , Eq. 3.2-2 becomes

$$\Delta\phi = \frac{nf}{c} (x\sin\theta - h\cos\theta) \quad (3.2-3)$$

### 3.2.2 Doppler Analysis

An improved measurement of the vehicle velocity can also be obtained from the GPS signals using a doppler-shift analysis. As a receiver moves with respect to an emitting source, the received frequency is doppler-shifted. For radio interferometry to GPS, satellite motion introduces two doppler-shift frequencies (one at each receiver). These frequencies are inherently different due to the additional velocity associated with the moving receiver, and can be related by the equation

$$f' = f \left[ \frac{1 + nv\cos\theta/c}{1 - nv\cos\theta/c} \right]^{1/2} \quad (3.2-4)$$

where

- $f$  = the doppler-shifted\* frequency as received at the fixed-receiver
- $f'$  = the doppler-shifted frequency as received at the moving receiver and due to the vehicle motion.

The difference,  $\Delta f$ , between the moving-receiver frequency and the fixed-receiver frequency represents the doppler-shift due to moving-receiver velocity alone and can be derived from Eq. 3.2-4 as

$$\Delta f = \frac{fv \cos \theta}{c} \left[ 1 + \frac{v \cos \theta}{2c} \right] \quad (3.2-5)$$

Details of the square-root expansion used to obtain Eq. 3.2-5 are presented in Appendix B.

### 3.3 APPLICABLE ERROR SOURCES AND MODELS

Interferometrically-derived distance measurements require knowledge of the difference between signal receiver paths. Hence, many of the error sources common to pseudorange (single-receiver) techniques do not affect dual-receiver measurement integrity. Error sources inherent to fixed-site radio interferometry and which are also applicable in dynamic applications, include receiver noise, emitted frequency instability, satellite ephemeris error, and clock jitter as well as previously discussed (Section 2.2) satellite geometry constraints (i.e., GDOP effects). In addition, there are mechanical and environmental error sources which are unique to a

---

\*This doppler shifting is due to satellite motion relative to the receivers and is approximately the same for both receivers.



moving-receiver mechanization. These include relative timing drift, atmospheric propagation errors, and multipath effects. The applicable error sources are addressed below by category (i.e., environmental, mechanical, measurement).

### 3.3.1 Environmental

#### Tropospheric Propagation Delay (Horizontal Variations) -

As described in Appendix C (Section C.2), effects in the lower atmosphere are an important contributor to interferometric measurement uncertainty. Tropospheric refractivity varies both temporally and spatially from survey point to point. Furthermore, correct modeling of these fluctuations requires regional (horizontal) atmospheric variabilities to be accounted for. One proposed approach, known as site diversity (Ref. 20), considers an exponential correlation between atmospheric conditions at the two receiver sites. This approach uses only one radio-meteorological sensor and neglects refractivity effects due to pressure fronts and clouds. Based on site diversity, a statistical model can be implemented using a first-order Markov process to characterize the correlation effect. To study interferometry measurement accuracies, empirical data were used to determine appropriate parameters for the Markov process. A correlation distance of 30 km and an rms error of 3 N-units were selected.

An alternative approach to site diversity requires the use of radio-meteorological sensors at both receiver locations. Errors associated with this approach are a function of the particular sensor used (see Table 3.1-2) and can be statistically modeled using a white-noise process. Appropriate parameters for this model are an rms error of 0.01 N-units and an averaging time of 0.1 sec.

#### Tropospheric Propagation Delay (Vertical Variations) -

Since vertical variations (fluctuations) in tropospheric refractivity increase with signal path length (see Appendix C, Section C.2), use of a spherical layer representation of the atmosphere above the earth offers an advantageous modeling geometry. In each layer, the refractivity fluctuations vary as the cosecant of the elevation angle  $\theta$ . These variations can be statistically modeled by a white-noise process with an rms value of 0.4 arc min (30-deg user-to-satellite elevation angle) for six-second averaging times (Ref. 20).

#### Multipath Effects - Moving-receiver radio interferom-

etry data can be corrupted by two sources of multipath errors. The first is due to vehicle-induced scattering of the GPS signal, i.e., temporary signal reflections caused by adjacent structures or emanating from vehicle surfaces. These reflections can be statistically modeled by a random process and require further investigation. For analysis purposes, this error is modeled as white noise with an rms error of  $1 \times 10^{-10}$  m for a 2.5-sec averaging time. The second source of multipath propagation is a result of atmospheric ducting (signal bounces from ground to atmosphere). Such reflections occur at low satellite elevation angles. These errors are avoided by requiring satellite elevation angles to be greater than 30 degrees.

#### Ionospheric Propagation Delay - The propagation delay

caused by the passage of electromagnetic waves through the ionosphere is discussed in Appendix C (Section C.3). For interferometric applications, this signal delay contributes measurement uncertainties whenever the inter-receiver distances are such that the GPS signal travels along two significantly different ionospheric paths (i.e., distances greater than 1000 km). Furthermore, this delay can be adequately compensated through the use of dual-frequency receivers or by appropriately modeling the upper atmosphere during data preprocessing

(see Appendix C). For this reason, effective compensation of ionospheric signal delay is assumed in TASC's analysis.

### 3.3.2 Mechanical

Clock Errors - To minimize timing errors when recording signal-phase differences, a moving-receiver interferometry-based system requires that the atomic clocks at the receiver sites be periodically synchronized. For cesium time standards, synchronization can be accomplished by phase-matching and time-averaging clock sine waves, resulting in correlation between the time pieces of one part in  $10^{11}$  for 100-second averaging times (Ref. 21). After synchronization, the clocks will decorrelate. The short-term loss of synchronization ("uncompensated relative drift") is statistically modeled using a random-ramp analysis. A random ramp is typically used to describe errors which exhibit time-growing behavior. The growth rate of the random ramp is a random quantity with a given probability density (Ref. 22).

In addition, the clocks have individual "jitter." This error can be characterized using a random walk analysis. A random walk process results when uncorrelated signals are integrated. This situation occurs when determining the cumulative effect of clock noise. For cesium clocks (e.g., the HP 5061A), the rms error is  $1 \times 10^{-13}$  sec (Ref. 23); thus, in six hours (a typical GGSS survey sortie) the system timing noise is two nanoseconds. This introduces a 10-cm error in inter-receiver distance measurements.

Emitted Frequency Instability - Analysis of the oscillators aboard the GPS satellites (Ref. 24) has demonstrated a stability of the emitted frequency to one part in  $10^{10}$  for averaging times of  $10^5$  sec. This instability yields distance

measurement errors on the order of  $10^{-9}$  m. Thus, this error source can be neglected for the accuracy level anticipated for the GGSS application.

Altitude Perturbations - Any variation in the altitude of the moving receiver between two sampling times will perturb the observed signal incidence angle,  $\theta$ . This phenomenon can be seen in Fig. 3.3-1. The observed distance,  $\Delta S_o$ , from the satellite signal wavefront to the second measurement point B can be written

$$\Delta S_o = \Delta S_t + \Delta S_e \quad (3.3-1)$$

where the subscripts t and e refer to the true and error portions of the observed distance. To a close approximation, the error contribution to the observed perpendicular distance is given by

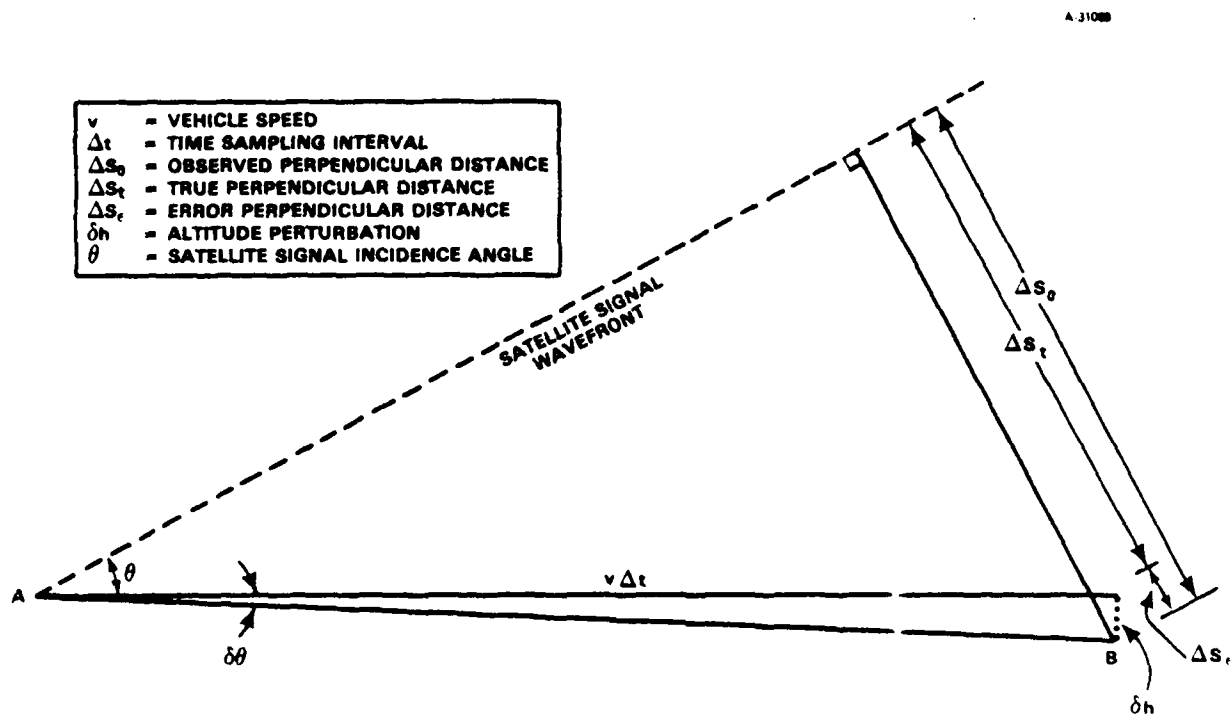


Figure 3.3-1 Effect of Altitude Perturbation on Signal Incidence Angle

$$\Delta S_{\varepsilon} = \delta h / \cos \theta \quad (3.3-2)$$

Employing small-angle approximations, the error for the incident angle,  $\delta \theta$ , can be written

$$\delta \theta = \Delta S_{\varepsilon} / (v t \cos \theta)$$

or equivalently,

$$\delta \theta = \delta h / (v t \cos^2 \theta) \quad (3.3-3)$$

The altitude perturbation,  $\delta h$ , is a vehicle-dependent error source representing the amount a vehicle will "bounce" away from the nominal trajectory. This error source can be statistically modeled using a white-noise process with an rms error of 1.0 m over a 2.5-sec averaging time.

The theoretical effect of the  $(1/\cos^2 \theta)$  factor in Eq. 3.3-4 is to create a singularity at  $\theta = 90^\circ$ ; i.e., the situation when a satellite is directly above the two receivers. In practice, as a satellite climbs to the overhead position, the GDOP degrades until another satellite is selected (yielding a more favorable geometry).

Satellite Ephemeris Error - Radio interferometry to GPS satellites is a generalization of quasar-based stellar interferometry. In actuality, the GPS satellites are not very distant, compared with quasars, so that the satellite signals arrive at the earth as spherical wavefronts. To apply the experience gained from very long baseline interferometry (VLBI) geodesy to the case of GPS signal sources, the actual spherical wavefronts must be reformulated into a plane wave with a correction term requiring explicit range information. The departure of the GPS wavefronts from plane waves is functionally represented by

$$\Delta S \propto b^2/r$$

(3.3-4)

where  $b$  is the inter-receiver distance and  $r$  is the satellite orbit radius ( $r \approx 26 \times 10^6 \text{ m}$ ). The ephemeris error is proportional to  $\Delta s/r$  and leads to an error of one millimeter for inter-receiver distances of 1000 km. This contributor to navigation error can be statistically modeled by a random constant for inter-receiver distances greater than 1000 km. For scenarios involving distances shorter than this, satellite ephemeris error can be neglected.

### 3.3.3 Measurement

Receiver Limitations - Accurate measurement of the phase difference and doppler shift between two receiver sites ultimately depends on the GPS receiver design. The TI 4100 receiver incorporates a time-sharing digital oscillator for multiple satellite signal tracking and requires precise carrier phase initialization at the start of each satellite signal sampling period. This carrier phase preset introduces a phase-tracking rms error (Ref. 7) of  $1.525 \times 10^{-5}$  cycles per cycle (averaging time of 2.5 sec) and is included as measurement noise (Ref. 22) in the interferometry analysis.

The GPS receiver is designed with phase lock loop (PLL) circuitry. By necessity, the PLL tracking bandwidth must be wide enough to accept frequency shifts caused by the relative motions of the satellite and receiver. The design of the receiver introduces a doppler-shift measurement error of 0.7 Hz rms for an averaging time of 2.5 sec. During the navigation analysis, this effect is modeled as measurement noise.

Summary of Error Sources - A compilation of the error sources associated with moving-receiver radio interferometry is presented in Table 3.3-1. For each source, the error model

TABLE 3.3-1  
COMPILATION OF MOVING-RECEIVER  
RADIO INTERFEROMETRY ERROR SOURCES

T-369

DESCRIPTION	MODEL STRUCTURE/ PARAMETERS	VALUE	UNITS
<u>ENVIRONMENTAL</u>			
Tropospheric Propagation Delay:			
Horizontal Variations: *			
Single-site monitoring	Markov process/ Correlation distance	30	km
	RMS error	3	N-units
Dual-site monitoring	White noise/ RMS error	0.01	N-units
	Averaging time	0.1	sec
Vertical Variations	White noise/ RMS error	0.4	arc min
	Averaging time	6.0	sec
Multipath Effects:			
Vehicle-induced	White noise/ RMS error	$1 \times 10^{-10}$	m
	Averaging time	2.5	sec
Ground-induced	Masked out by elevation angle requirements	---	---
Ionospheric Propagation Delay	Not modeled <sup>†</sup>	---	---
<u>MECHANICAL</u>			
Clock Errors:			
Uncompensated relative drift*	Random ramp/ RMS ramp slope	$1 \times 10^{-11}$	sec/sec
Compensated relative drift (clock jitter)	Random walk/ RMS error	$1 \times 10^{-13}$	sec
Emitted Frequency Instability	White noise/ RMS error	$1 \times 10^{-10}$	Hz
	Averaging time	$1 \times 10^5$	sec
Altitude Perturbation	White noise/ RMS error	1.0	m
	Averaging time	2.5	sec
Satellite Ephemeris Error	Not Modeled <sup>†</sup>	---	---
<u>MEASUREMENT</u>			
Phase-Tracking Error	White noise/ RMS error	$1.525 \times 10^{-5}$	cycles/cycle
	Averaging time	2.5	sec
Doppler-shift Measurement Error	White noise/ RMS error	0.7	Hz
	Averaging time	2.5	sec

\*Not part of nominal analysis; included for separate sensitivity analyses.

†Not applicable for inter-receiver distances less than 1000 km.

and associated parameter values which were used in TASC's analysis are provided in the table. Discussion of study results follows.

### 3.4 ANALYSIS RESULTS

#### 3.4.1 Simulation Details

The position, velocity, and acceleration measurement capability of moving-receiver radio interferometry was assessed using covariance analysis techniques and the error models described in the previous section. In this analysis, a coplanar base-station, host vehicle trajectory, and single-satellite flight path were simulated. Optimal Kalman smoothing techniques (Ref. 22) were applied to: 1) determine the interferometer system's ability to measure navigation quantities and 2) study the sensitivity of measurement accuracy to vehicle velocity, atmospheric refractivity sensor availability, timing drift compensation, and vehicle-to-satellite elevation angle. Both surface and airborne vehicle surveying applications were simulated.

The error dynamics of the moving-receiver system are represented by the linear first-order vector-matrix differential equation

$$\dot{\underline{x}}(t) = F(t) \underline{x}(t) + \underline{w}(t) \quad (3.4-1)$$

where  $\underline{x}(t)$  is the system state vector,  $\underline{w}(t)$  is the random forcing function, and  $F(t)$  is the system dynamics matrix. Using this form, the following expressions can be written for the vehicle horizontal position ( $\delta p$ ), velocity ( $\delta v$ ), and acceleration ( $\delta a$ ) errors:



$$\begin{aligned}
\delta \dot{p} &= -v/n \delta n + v \tan \theta \delta \theta + \xi v/f \delta f \\
\delta \dot{v} &= -v/(nt) \delta n + v \tan \theta / t \delta \theta + \xi v/(ft) \delta f - v/t^2 \delta t \\
\delta \dot{a} &= -v/(nt^2) \delta n + v \tan \theta / t^2 \delta \theta + \xi v/(ft^2) \delta f - v/t^3 \delta t
\end{aligned}$$

(3.4-2)

where

$v$  = nominal vehicle speed (50 km/hr - surface van; 450 km/hr - aircraft)  
 $n$  = nominal index of refraction (1.00035)  
 $\theta$  = receiver to satellite elevation angle (30 deg)  
 $f$  = nominal GPS transmitting frequency (1.5754 GHz)  
 $t$  = averaged measurement interval (1.2 sec)  
 $\xi = [c^2 - (nv \cos \theta)^2] / (c n \cos \theta)$   
 $\delta n$  = tropospheric refractivity error  
 $\delta \theta$  = signal elevation angular error  
 $\delta f$  = emitted frequency instability  
 $\delta t$  = clock errors.

The velocity-dependent term,  $\xi$ , and the differential equation for  $\delta p$  are derived in Appendix B.

The simulation scenario incorporates a single GPS satellite, a TI 4100 receiver at a fixed-site, and a TI 4100 receiver aboard a moving vehicle (surface van and aircraft). The moving receiver travels at a constant velocity and altitude away from the fixed receiver. In addition, the flight paths of the satellite and the vehicle are coplanar and inter-receiver distances less than 1000 km were maintained. Note that for distances larger than this, the flat-earth approximations implicit in the dynamics equations (e.g., identical

satellite frequencies and elevation angles at both receivers) are no longer valid. In all simulations, the atomic clocks are considered synchronized within nominal phase-tracking error limits at survey initialization (see clock error models listed in Table 3.3-1). A summary of the nominal scenario simulated in TASC's analysis of moving-receiver radio interferometry is presented in Table 3.4-1.

### 3.4.2 Results

This section describes the results associated with TASC's study of moving-receiver radio interferometry to support moving-base gravity field survey activities. In particular, the relative distance, velocity, and acceleration measurement capability of the system for both surface vehicle and airborne applications is addressed. For these analyses, the simulation explicitly accounts for the use of dual-site refractivity monitors and presumes that post-mission compensation for relative

TABLE 3.4-1  
NOMINAL SCENARIO DETAILS

ITEM	DESCRIPTION
<u>Hardware</u>	
Gravity Sensor	GGSS
Clock	Atomic (at fixed site and aboard moving vehicle; relative timing drift compensated for)
GPS Receiver	TI 4100 (at fixed site and aboard moving vehicle)
Radio-Meteorological Sensor	Microwave refractometer (at both receiver locations)
<u>Operating Conditions</u>	
Vehicle Type	Surface van, aircraft
Van Speed	50 km/hr
Aircraft Speed	450 km/hr
Aircraft Altitude	600 m
Vehicle Flight Path	Coplanar with satellite; away from fixed receiver
Signal Elevation Angle	At least 30 deg

clock drift can be performed to accuracies already demonstrated by other investigations (Ref. 15). In addition, the sensitivity of the measurement accuracy to key operational elements (vehicle speed, atmospheric refractivity sensor availability, timing drift compensation, and signal elevation angle) is quantified.

The navigation accuracies associated with surface vehicle and airborne applications of radio interferometry are presented in Table 3.4-2. These results indicate that for a 50-km survey track, position accuracy to better than one-meter can be anticipated; similarly, for a 500-km track, less than 10 m error is expected. Results associated with varying the vehicle speed up to 450 km/hr are presented in Fig. 3.4-1. Note that for near-stationary receivers, the positioning accuracy approaches about 1-2 ppm, which is the accuracy level typically reported from fixed-site investigations (Refs. 13-15). These encouraging positioning accuracies demonstrate the adequacy of using this approach as a back-up during GGSS testing, particularly in surface vehicle testing scenarios where stringent positioning accuracies may be required.

TABLE 3.4-2  
MEASUREMENT CAPABILITY OF RADIO INTERFEROMETRY

NAVIGATION QUANTITY (HORIZONTAL AXIS)	UNITS	RMS ERROR	
		SURFACE VEHICLE APPLICATION	AIRBORNE APPLICATION
Relative Distance	ppm	11	72
Velocity	cm/sec	0.002	0.02
Acceleration	mgal	0.4	4.4

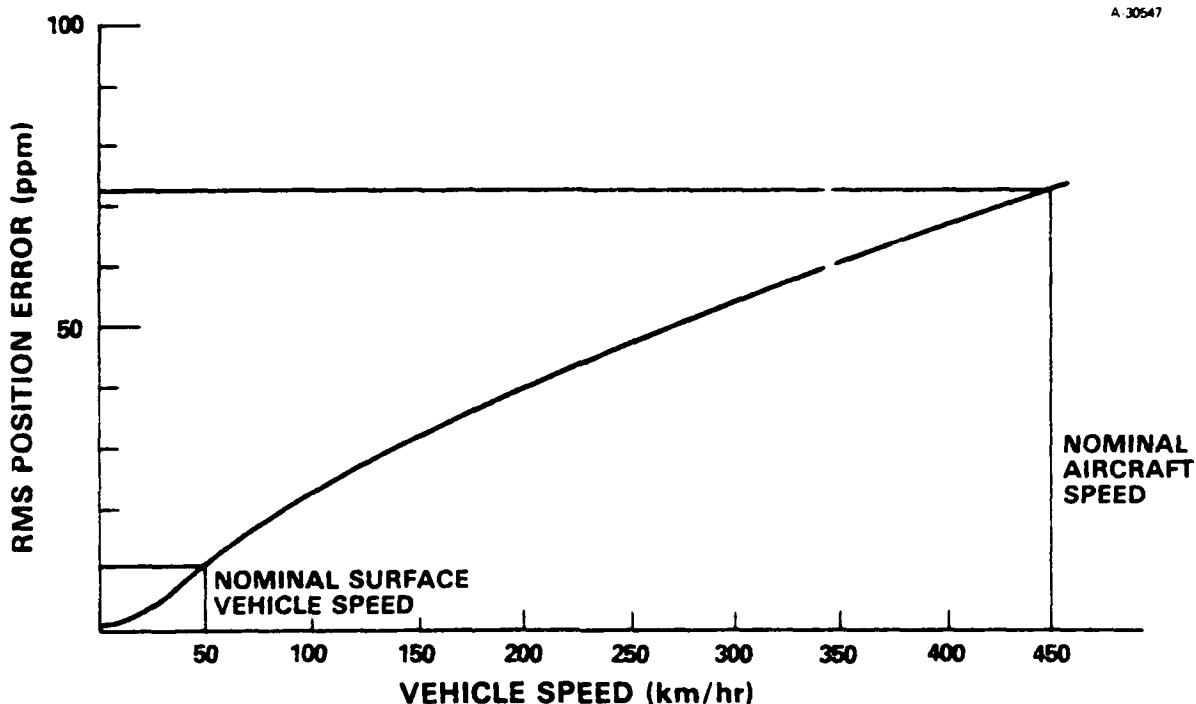


Figure 3.4-1 Sensitivity of Position Measurement Accuracy to Vehicle Speed

Vehicle speed has a significant effect on the acceleration measurement capability of radio interferometry. This effect is illustrated in Fig. 3.4-2. For slowly moving surface vehicles, a theoretical accuracy level on the order of that anticipated from the GGSS is anticipated. The degradation of acceleration measurement accuracy to 4.4 mgal for the airborne application is necessarily due to the increased vertical position and velocity uncertainty (typically, an order of magnitude difference) at the higher speeds.

Sensitivity of Measurement Accuracy to Atmospheric Refractivity Sensor Availability - The effect of tropospheric refractivity on interferometric measurement accuracy has been the subject of extensive error modeling (Refs. 20 and 25) and hardware development (Refs. 26 and 27). The signal delay caused by the lower atmosphere requires at least one monitor

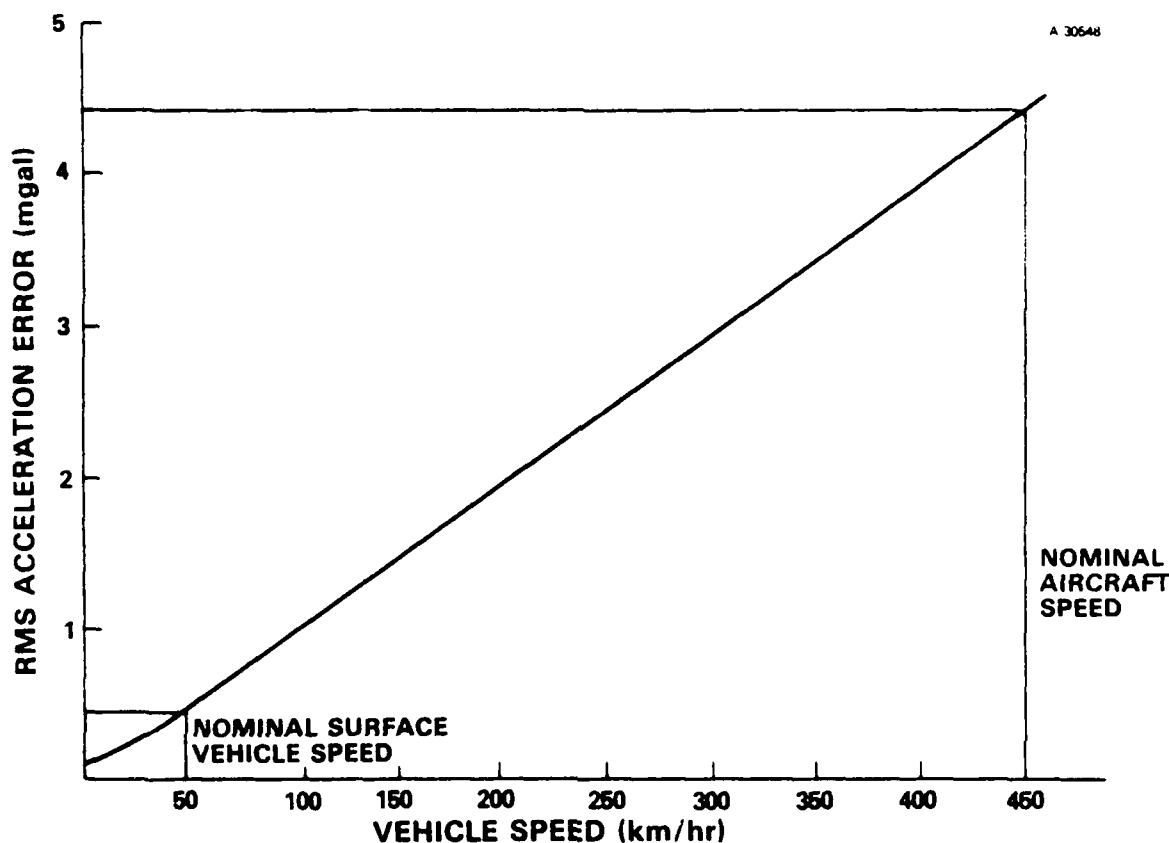


Figure 3.4-2 Sensitivity of Acceleration Measurement Accuracy to Vehicle Speed

(situated at either receiver location) to record local atmospheric variations. However, since a moving-receiver application of radio interferometry increases the probability of encountering tropospheric conditions significantly different from fixed-site applications (hence, different refractive indices), atmospheric monitoring at both receiver sites is appropriate. The implications of single vs dual-site monitoring on measurement accuracy are discussed in the paragraphs which follow.

As noted in Section 3.1.1 and summarized in Table 3.1-1, error models for tropospheric signal delay are included in the

analysis. Two scenarios were simulated as part of this sensitivity study. The first considered a single microwave refractometer monitoring local atmospheric fluctuations at the fixed-site receiver. A third-order Markov process (see Table 3.3-1) was used to provide the necessary correlation between the atmospheric conditions at the two receiver sites. (The derivation of the matrices associated with the state-space form of a third-order Markov process is included in Appendix D.) The second scenario simulated the case involving microwave refractometers located at both receiver locations. (Note that this is the nominal system configuration considered in TASC's analyses as indicated in Table 3.4-1.) Refractivity measurement inaccuracy is modeled as white noise (see Table 3.3-1) in this case. Other details of the simulated scenario were unchanged from the nominal case identified in Table 3.4-1.

The distance measurement accuracies for both atmospheric monitoring situations are presented in Fig. 3.4-3. For single-site monitoring, the Markov correlation distance of 30 km (see Table 3.1-1) is traveled in 240 seconds. From the upper curve in Fig. 3.4-3, this "correlation time" corresponds to the time at which the position measurement accuracy begins to degrade. This degradation is necessarily due to a lack of additional information regarding the varying atmospheric conditions between receivers.

The sensitivity of the interferometry analysis results to unmodeled atmospheric property variations can be reduced by using more than one refractometer. Specifically, multiple fixed-site atmospheric sensors can be positioned throughout the survey area. Data collected from these sensors can be used to extrapolate the changing atmospheric conditions between the receivers. An extension of this multisensor situation involves dual-site monitoring (i.e., refractometers at both

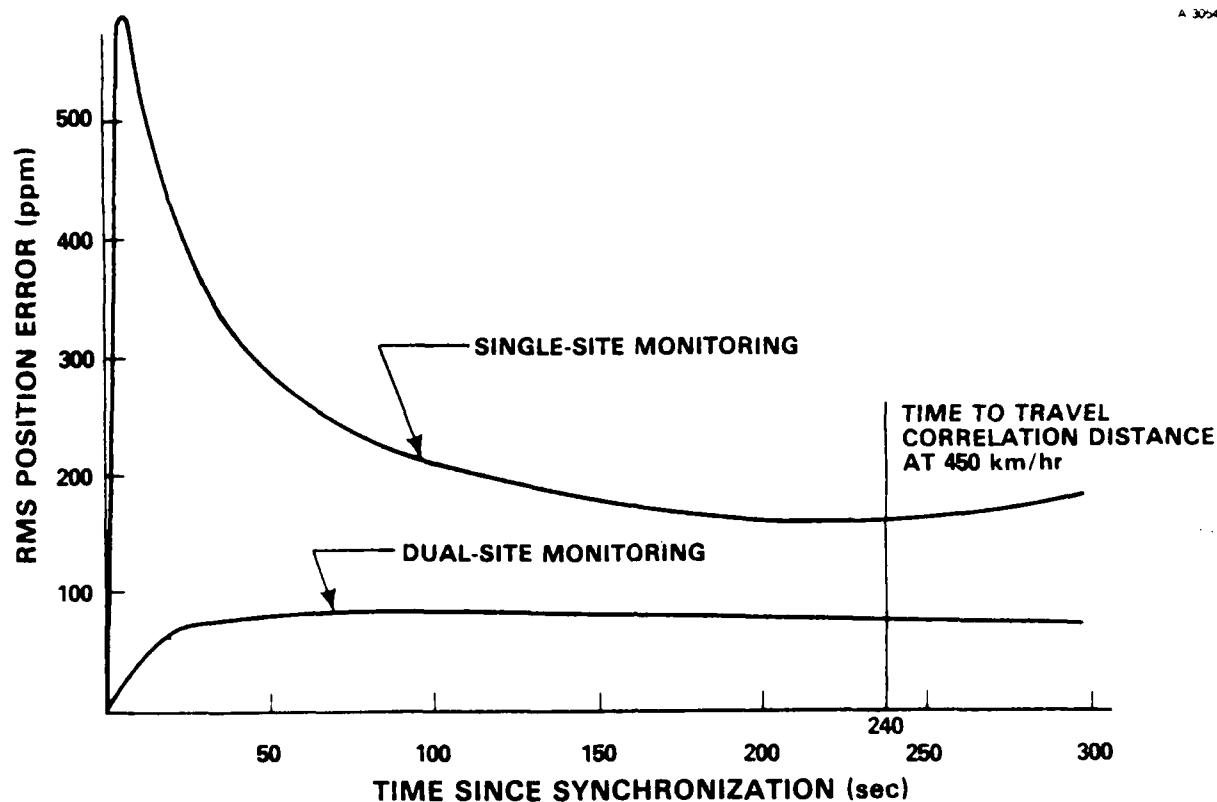


Figure 3.4-3 Sensitivity of Position Measurement Accuracy to Atmospheric Monitoring

the fixed- and moving-receiver locations). The results of simulating this scenario are reflected in the lower curve of Fig. 3.4-3. With atmospheric monitors at both receivers, position accuracy based on radio interferometry to GPS approaches 75 ppm rms.

The same effects are observed in the acceleration measurement error results which are illustrated in Fig. 3.4-4. For single-site monitoring, the rms measurement error is 11.0 mgal. When the vehicle nears the correlation distance of the Markov process (at 240 sec), acceleration measurement accuracy degrades rapidly. This is expected due to the lack of additional information regarding varying atmospheric conditions between receivers. Dual-site monitoring reduces the acceleration rms error by nearly a factor of three.

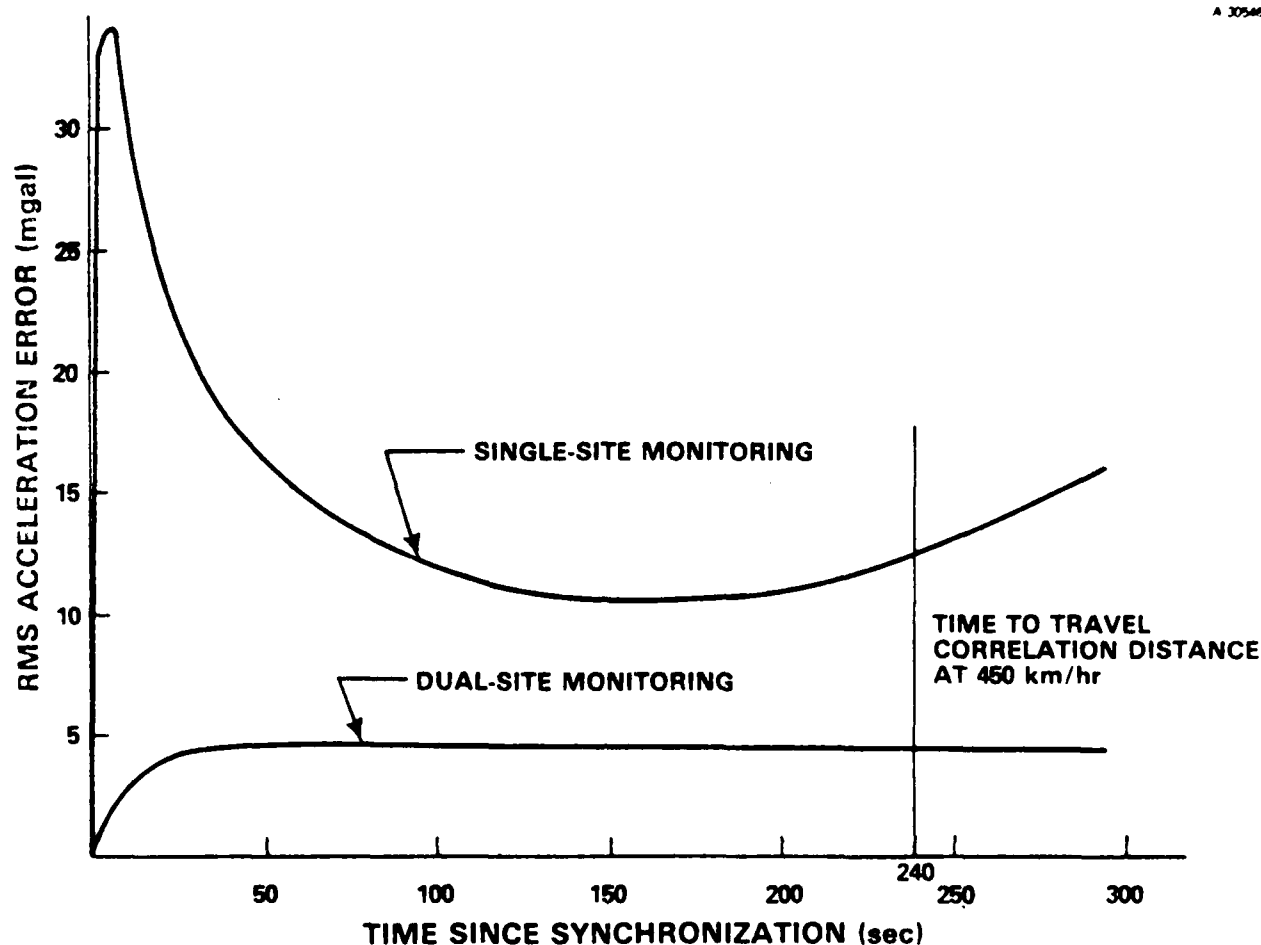


Figure 3.4-4 Sensitivity of Acceleration Measurement Accuracy to Atmospheric Monitoring

These two simulations illustrate "worst-case" scenarios in which a receiver is traveling directly away from an atmospheric monitor positioned at a fixed-site. As part of the preparation for analysis of radio interferometry data to be recorded during a survey of a particular area during a particular time of year, a statistical model can be formulated to describe accurately the varying atmospheric conditions between receivers. For example, the parameters of a Markov process (correlation distance and rms noise) can be fitted using previously collected data to portray the conditions expected at the particular test site during the relevant time-of-year. In practice, the vehicle trajectory can be carefully planned



so that the moving receiver is within the correlation distance of the fitted Markov process for sufficiently long time intervals. For example, the monitor can be positioned in the center of the area to be surveyed or more than one fixed-site monitor can be employed in the area. In this situation, navigation accuracies sufficient for the GGSS application would be maintained for longer times during the course of a survey mission.

Preliminary analyses indicate that the correlation distance parameter is quite region-sensitive. Thus, during actual surveys, a single fixed-site refractometer may not be adequate to correct for tropospheric signal delays throughout the entire survey area. Furthermore, as the results in Figs. 3.4-3 and 3.4-4 demonstrate, single-site monitoring would not produce the desired navigation accuracies. In addition, dual-site monitoring using microwave refractometers only leads to a factor of two improvement in measurement accuracies compared with single-site monitoring. However, should portable, line-of-sight, dual-frequency radiometers be available for survey use (see Section 3.1.1), vehicle navigation accuracies can be expected to improve by an order of magnitude for dual-site monitoring situations. Sensitivity analyses show that this improvement results in single-digit ppm distance and sub-milligal acceleration measurement rms accuracies for the airborne application.

Sensitivity of Measurement Accuracy to Timing Drift Compensation - To compare the effects of clock jitter and loss of synchronization between two atomic clocks on measurement accuracy, two different models were employed in the analysis (see Table 3.3-1). A random ramp process was included to model the loss of synchronization. The effect of clock jitter on vehicle navigation accuracy was studied by setting the ramp slope parameter to zero. This latter case simulates the anticipated post-survey data-reduction situation which would occur

following an accurate timing drift correction. Additional modeling details are discussed in Section 3.3 and summarized in Table 3.3-1; a description of the nominal analysis scenario is presented in Table 3.4-1.

Although typical survey missions require six to eight hours, the effect of timing errors on navigation accuracy is observable after only five minutes. The rms error associated with measuring vehicle acceleration is illustrated in Fig. 3.4-5 for the two situations described above. The ability to measure

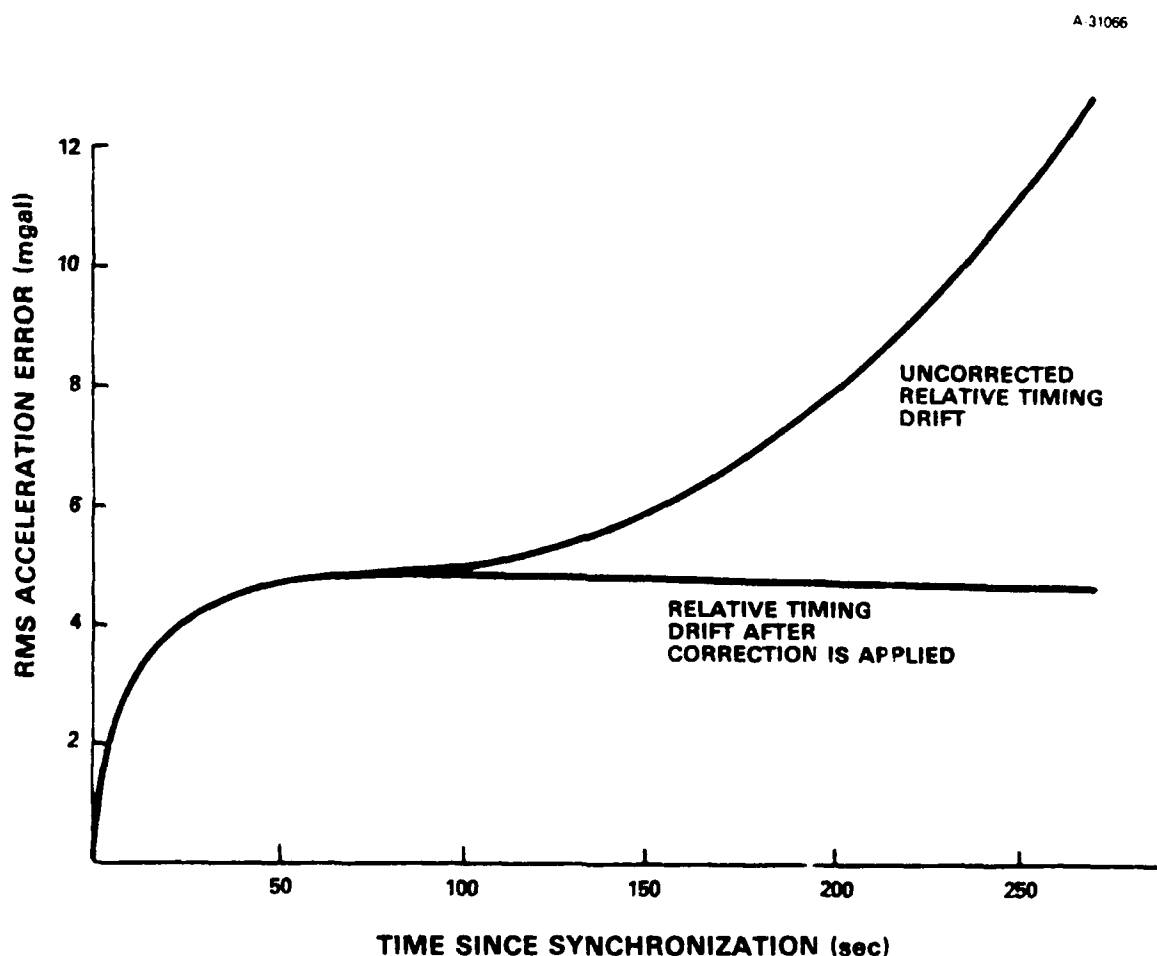


Figure 3.4-5 Sensitivity of Acceleration Measurement Accuracy to Adequacy of Timing Drift Compensation

accurately acceleration is degraded by clock drift even when atomic frequency standards are used and synchronized at the start of a survey mission. After five minutes, the accuracy of the uncorrected measurements is observed to be 30 percent worse than the case in which the relative timing drift is adequately compensated. Thus, to ensure accurate velocity and acceleration measurements using radio interferometry, a correction must be applied to the data to compensate for loss of synchronization.

Figure 3.4-5 also illustrates the minimal effect of clock noise on acceleration uncertainty after the recorded data are corrected for relative timing drift. The error due to clock jitter ultimately determines the maximum time interval between synchronizations. As noted earlier, survey operations can last as long as eight hours. During this time, clock noise can be expected to increase to approximately three nanoseconds. Such a timing error contributes a one percent error in acceleration measurement accuracy (0.04 mgal rms error at 450 km/hr). Accordingly, an eight-hour resynchronization schedule is appropriate for ensuring the negligible contribution of clock error to navigation error.

Sensitivity of Measurement Accuracy to Signal Elevation Angle - The sensitivity of measurement accuracy to the elevation angle of the satellite-transmitted signal was also analyzed. Signals from satellites near the horizon are subject to high refractivity errors while interferometry-related errors increase whenever a tracked satellite approaches the zenith and the vehicle trajectory becomes more parallel to the GPS signal wavefront. The effect of these two extremes was studied to determine the satellite "drop" angle, i.e., the angle at which greater vertical channel measurement accuracy can be obtained using altimeter rather than GPS information. Note

that this drop angle is not a priori GDOP-dependent, although many of the same geometric arguments apply (see Section 3.3.2). The nominal airborne scenario described in Table 3.4-1 was used for this study.

The analysis results are illustrated in Fig. 3.4-6. As the signal elevation angle,  $\theta$ , increases beyond  $75^\circ$ , the acceleration error increases as  $1/\cos^2\theta$ , as predicted by the discussion in Section 3.3. However, between 30 and 75 deg the acceleration rms error changes by only 0.02 mgal and thus, the effect of signal elevation angle is inconsequential for the practical case which considers effective selection of available satellites.

### 3.4.3 Conclusions

TASC's analysis of moving-receiver radio interferometry indicates distance measurement accuracies of about 10 ppm

A-31067

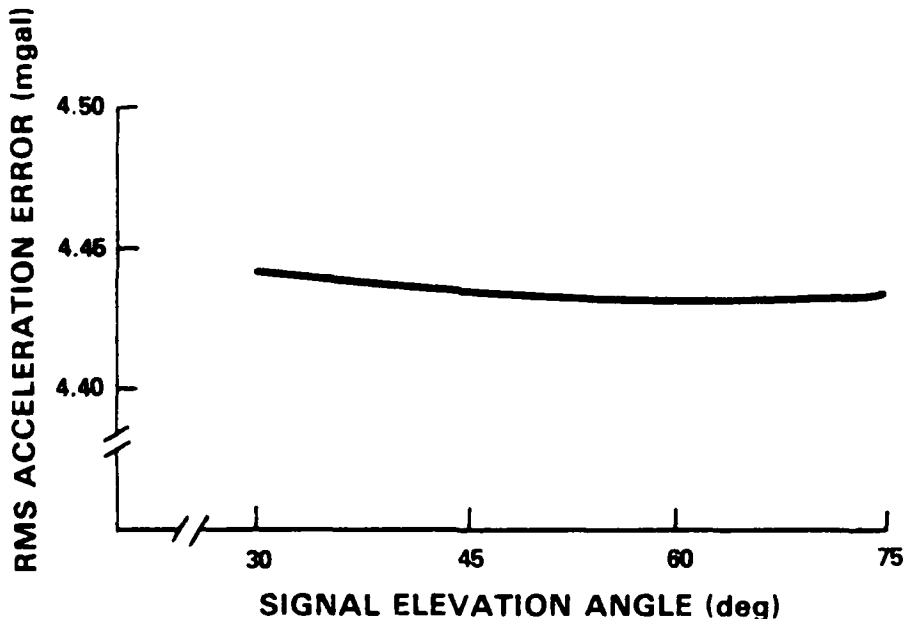


Figure 3.4-6 Sensitivity of Acceleration Measurement Accuracy to Signal Elevation Angle

rms and 70 ppm rms are currently feasible for surface and airborne surveys, respectively. These accuracy levels exceed those believed to be necessary for GGSS testing. In addition, acceleration can be measured to sub-milligal accuracy for vehicle speeds less than 100 km/hr, as shown in Fig. 3.4-2.

High-accuracy radio interferometry-derived measurements will depend on the manner in which tropospheric refractivity is measured and the accuracy with which observed propagation delay is treated in the system. Several refractivity monitors, including the class of experimental radiometers, were assessed and incorporated into simulations which replicated single- and dual-site atmospheric monitoring scenarios. Not surprisingly, refractivity monitoring at both receiver locations yields the more accurate measurements (compared with single-site monitoring); dual-site monitoring offers an improvement in navigation accuracy by a factor of two or three. Thus, for certain survey applications (e.g., surveys local to the monitoring site), detailed modeling of tropospheric refractivity errors may be preferable to dual-site recordings.

Accurate interferometrically derived acceleration measurements require precise and synchronized clocks to maintain data integrity. The analysis incorporated error models appropriate for atomic clock standards and examined the effects of clock jitter and relative drift on navigation accuracies. The study results indicate a need to synchronize the receiver clocks prior to survey operations and every eight hours thereafter, as appropriate. In addition, the recorded data must be compensated for the loss of clock synchronization prior to post-survey data reduction.

The study also investigated available GPS receivers to determine which is best suited for moving-receiver radio

interferometry use. Receivers were compared on the basis of hardware design and signal quantities measured. TASC's evaluation indicates that the Texas Instruments TI 4100 GPS receiver is uniquely qualified to support applications of moving-receiver radio interferometry. This result confirms the wisdom of the current baseline GGSS configuration which uses this particular receiver.

Based on these and other published results (Ref. 28), the inter-receiver distance and acceleration measurement accuracy levels presented herein can be maintained under actual survey conditions. Thus, it is reasonable to conclude that moving-receiver radio interferometry offers an attractive backup to the nominal airborne GGSS positioning system (i.e., GPS pseudorange) and furthermore, is a low-cost, low-risk alternative to the fifth-wheel mechanization planned for the GGSS surface vehicle. The results presented herein demonstrate the ability of radio interferometry to provide the stringent positioning accuracies which may be required for surface testing. In addition, for surface vehicle surveys, the acceleration measurements can be used to provide an independent measure of gravity (see below).

### 3.5 TECHNICAL RISK AND RECOMMENDATIONS

#### 3.5.1 Technical Risk

Many of the uncertainties associated with moving-receiver radio interferometry have been identified and quantified. These analysis results are presented in the foregoing sections.

Hardware considerations indicate that integration of moving-receiver interferometry with the GGSS can be accomplished with a minimal modification effort since the currently planned GPS receiver and GGSS data acquisition/monitoring system are adequate for providing the required phase measurements. The only other additions required consist of a second GPS receiver, atomic clock, and data recorder at a convenient fixed site, and at least one refractivity monitor at either the fixed site or aboard the moving receiver. Thus, radio interferometry employing a mobile GPS receiver promises to be an especially significant new approach for providing very accurate navigation and geodetic information, either in conjunction with the GGSS or as a stand-alone sensor.

### 3.5.2 Recommendations

TASC has studied the feasibility of using moving-receiver radio interferometry as a positioning backup for GGSS surface testing and survey operations and determined that the approach holds considerable promise. These results should be furthered by augmenting the GGSS surface test plan to accommodate this capability. The logical next step is a demonstration of interferometric acceleration and gravity measurements in surface vehicle surveys.

The accuracy potential for recovering the gravity vector via multiple sensor measurements bears further scrutiny. In particular, incorporating interferometrically derived position and velocity measurements with other GGSS aides (such as a vertical accelerometer or gravimeter) may reduce airborne acceleration uncertainties to sub-milligal levels (see Chapter 4). Identification of the gravity field wavelengths most observable via radio interferometry is an appropriate extension of this investigation.

Finally, the status of atmospheric refractivity monitoring technology should continue to be followed closely. The evaluation of rugged, portable dual-frequency microwave radiometers will further increase the capability of radio interferometry to provide very accurate measurements of navigation quantities.



4.

#### GRAVIMETER-AIDING ANALYSIS

The incorporation of a gravimeter into the airborne GGSS as currently configured will improve the quality of surface gravity disturbance vector recovery. A gravimeter is complementary to the GGSS since it measures the longer wavelengths of the gravity field, while the GGSS observes the shorter wavelengths. Current positioning techniques, such as those associated with conventional GPS pseudoranging, are capable of supporting a significant reduction in survey errors over the entire gravity field spectrum. A substantial improvement in navigation accuracy (horizontal velocity and vertical position, in particular), such as may be attainable using radio interferometric techniques (see Chapter 3), yields a reduction in gravity recovery errors over the shorter wavelengths of the spectrum (less than 500 km). The associated velocity accuracy is necessary to overcome the dominant Eötvös correction error.

##### 4.1 SYSTEM DESCRIPTION AND MECHANIZATION DETAILS

As noted in Section 2.1, the GGSS mechanization includes three gravity gradiometers mounted on a three-axis inertially stabilized platform. Control updates based on GPS-determined position are periodically provided to the platform to obtain adequate orientation and positioning. The GGSS platform was designed (for equipment growth potential) to accommodate the mounting of two Bell BGM-4 gravimeters to the pitch gimbal. Note that the Gravity Sensor System, which was developed for the U.S. Navy and is the basis for the GGSS design, includes two Bell BGM-3 gravimeters in its implementation

aboard the USNS Vanguard. In fact, for the GGSS, the only changes in the basic mechanization to support the addition of the gravimeters involve interfacing between the gravimeters and the platform, data monitoring/recording system, and onboard computer.

A LaCoste and Romberg air-sea gravimeter has been used as the gravity sensor in several test and operational airborne surveys. In June 1981, the Naval Research Laboratory tested an airborne gravimetry system aboard a P3-A Orion fixed-wing aircraft (Ref. 29). Since the start of this decade, Carson Geoscience Company (formerly Carson Helicopters, Inc.) has been conducting airborne gravity surveys aboard a Sikorski S61 helicopter to aid oil and gas exploration (Refs. 30 and 31). The choice of this particular gravimeter is based primarily on availability and cost. A brief description of this gravimeter and two other types which currently offer potential for accurately measuring gravity on a moving base follows.

The LaCoste and Romberg gravimeter uses a spring to support a pivoted beam containing a mass at its free end. The elements of the meter are designed so that gravitational force on the mass is balanced by a "zero-length" spring. Such a spring implies that the tension is proportional to the length of the spring, and theoretically, if all external forces were removed the spring would collapse to zero length. In practice, this gravity meter is used as a null instrument. An adjustable second spring is used to restore the pivoting beam to its original horizontal position. The external acceleration can then be determined by measuring this resultant restoring force and scaling appropriately. The moving system of the Worden gravimeter is similar to the LaCoste and Romberg design; however, the Worden instrument is small, lightweight, and contains an automatic temperature-compensation scheme. Further details of these two gravimeters are presented in Ref. 32.

The Bell Aerospace BGM-3 gravimeter consists of a forced feed-back accelerometer (Bell Model XI) mounted on a gyrostabilized platform. The sensor requires no cross-coupling correction and represents a significant improvement over the conventional spring-type gravimeters. A comparison of gravity data collected with both the BGM-3 and a conventional-type gravimeter yielded an rms discrepancy between free-air gravity anomaly values at ship-track crossings of 0.38 mgal for the BGM-3 and 1.35 mgal for the conventional type (Ref. 33). Based on these and other encouraging test results, the BGM-3 gravimeter is now routinely used by NAVOCEANO for gravity surveys over the ocean for DMA, and is also used to provide redundant gravity data in support of ongoing tests of new equipment. In addition, a special version of the the BGM-3 is included in the Gravimeter Module Assembly (GMA) of the U.S. Navy's Gravity Sensor System (GSS). Two GMAs will be mounted on the gravity sensor platform of each GSS. A prototype of this version of the GSS (Advanced Development Model II) is currently undergoing laboratory testing at Bell Aerospace. However, additional research is needed prior to incorporating this more accurate (and much more expensive) instrument in routine airborne survey applications.

## 4.2 ANALYSIS APPROACH AND RESULTS

### 4.2.1 Approach

Airborne gravimeter surveys are analyzed using TASC's Multisensor Survey Simulation (MSS) capability (Ref. 34). This analysis represents the gravity field as a two-dimensional random field process with known correlation characteristics, models sensor measurement errors as stationary gaussian processes independent of the gravity field, and accounts for all

significant geometrical and mechanization effects. Multi-dimensional Wiener smoothing is used to derive the average power spectral density of post-survey gravity residuals. Since the Wiener smoother is optimal in the sense of minimizing the mean-square survey error residuals, the MSS outputs represent the best possible use of the survey data.

An overview of the multisensor survey analysis methodology is presented in Fig. 4.2-1. The output is obtained by applying the analysis techniques described in Ref. 34. The results are the statistics of the post-survey residual gravity errors. The following quantities are required inputs to the analysis process:

- Statistical model for the unsurveyed anomalous field
- Gravimeter and GGSS error models appropriate for an airborne application
- Characteristics of the survey.

A-31071

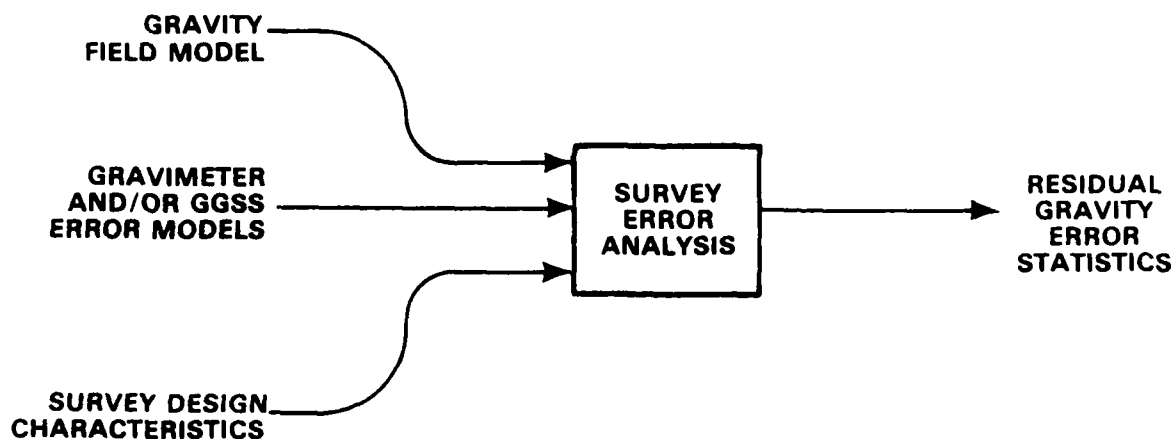


Figure 4.2-1 Overview of Multisensor Survey Analysis Methodology

For this study, a statistical model for gravity in the North Texas GGSS test area was employed. The model is an Attenuated White Noise (AWN) gravity field model which was specially tuned to the physiography of the GGSS test area. Additional details of this model are presented in Ref. 35.

#### 4.2.2 Survey Geometry and Measurement Error Models

Survey geometry refers to the position of the measurements and the orientation of the sensors with respect to the earth. Measurement error models, discussed in more detail below, are used to characterize the applicable error sources. The airborne gravimeter and GGSS error models were derived by appropriately extending the shipborne gravimetry and airborne gradiometry models documented in Ref. 34. The discussion below follows the development and conventions used in Refs. 34 and 36.

Airborne GGSS Survey - Figure 4.2-2 identifies the nominal GGSS airborne survey parameters which were used to estimate the statistics of the residual gravity errors. The cross-track spacing is  $\tau_2$  and the along-track spacing is

$$\tau_1 = Vt_g \quad (4.2-1)$$

where  $V$  is the nominal survey speed and  $t_g$  (10 sec) is the time interval between successive samples.

As shown in Fig. 4.2-3, the three gravity gradiometer instruments are symmetrically distributed about the vertical axis, with each gradiometer inclined at the same "umbrella" angle  $\alpha$ . Figure 4.2-3 also identifies the  $u,v,w$ , instrument axes and local-level  $x,y,z$  platform axes. Each gradiometer measures two elements of the gravity gradient tensor in the instrument  $u,v,w$  coordinate frame, i.e., the cross gradient

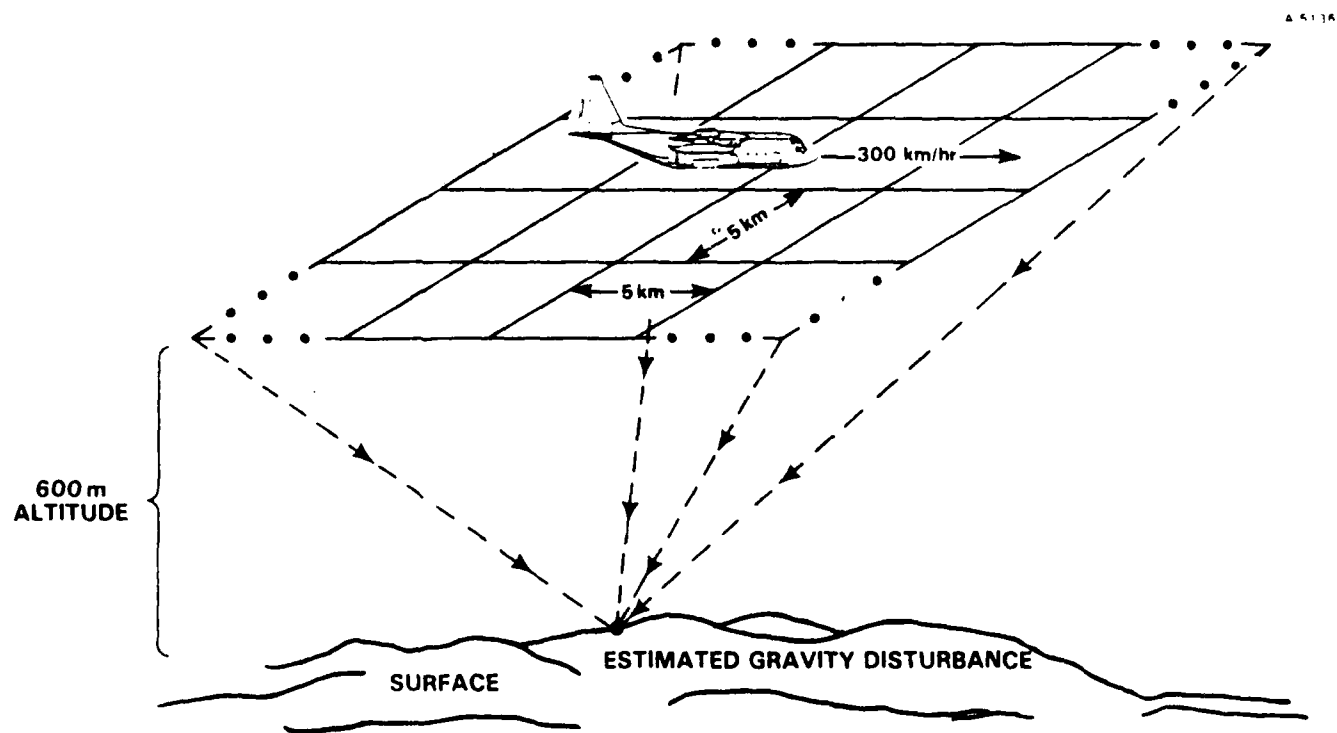


Figure 4.2-2 Nominal GGSS Airborne Survey Parameters

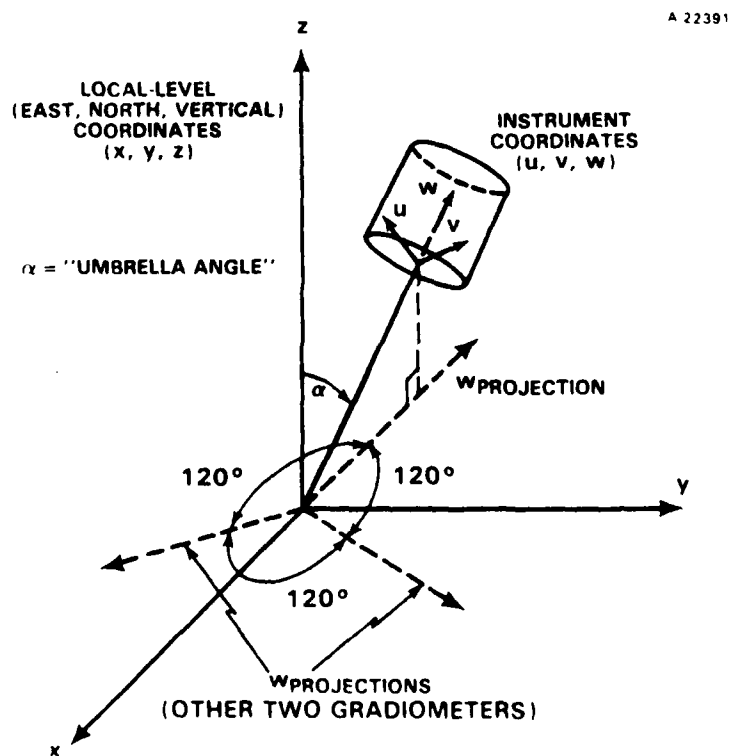


Figure 4.2-3 GGSS Geometry and Coordinate Systems

$T_{uv}$  and the difference of the two in-line gradients,  $T_{uu} - T_{vv}$ . Furthermore, each of these two gradiometer outputs is a certain linear combination of the gradients of the potential given by

$$\begin{bmatrix} T_{11} \\ T_{12} \\ T_{21} \\ T_{22} \\ T_{31} \\ T_{32} \end{bmatrix} = \begin{bmatrix} -1/4 & 1/4 & 0 & \sqrt{3}/6 & \sqrt{2}/2 & \sqrt{6}/6 \\ -1/3 & 0 & 1/3 & -\sqrt{3}/3 & -\sqrt{2}/6 & \sqrt{6}/6 \\ 1/4 & -1/4 & 0 & \sqrt{3}/6 & -\sqrt{2}/2 & \sqrt{6}/6 \\ -1/3 & 0 & 1/3 & \sqrt{3}/3 & -\sqrt{2}/6 & -\sqrt{6}/6 \\ 0 & 0 & 0 & -\sqrt{3}/3 & 0 & -\sqrt{6}/3 \\ 1/6 & -1/2 & 1/3 & 0 & \sqrt{2}/3 & 0 \end{bmatrix} \begin{bmatrix} T_{xx} \\ T_{yy} \\ T_{zz} \\ T_{xy} \\ T_{xz} \\ T_{yz} \end{bmatrix}$$

(4.2-2)

where  $T_{ij}$  represents the  $j^{\text{th}}$  output of the  $i^{\text{th}}$  gradiometer ( $j = 1, 2$ , and  $i = 1, 2, 3$ ) and  $T_{xx}$ ,  $T_{yy}$ ,  $T_{zz}$ ,  $T_{xy}$ ,  $T_{xz}$ , and  $T_{yz}$  are elements of the gravity gradient tensor in an east (x), north (y), up (z) reference frame.

The vector transfer function,  $\underline{F}$ , from anomalous surface potential to the measured quantities can be represented by

$$\underline{F}(\underline{s}) = \underline{B}\underline{H}(\underline{s}) \quad (4.2-3)$$

where  $\underline{s}$  is the vector of spatial frequencies ( $s_1$  and  $s_2$  are measured in the east and north directions, respectively);  $\underline{B}$  is the  $6 \times 6$  matrix of Eq. 4.2-2; and  $\underline{H}$ , the vector transfer function from anomalous potential at height  $h$  is given by

$$\underline{H}(\underline{s}) = 4\pi^2 e^{-2\pi s h} \begin{bmatrix} -s_1^2 \\ -s_2^2 \\ s^2 \\ -s_1 s_2 \\ -is_1 s \\ -is_2 s \end{bmatrix} \quad (4.2-4)$$

where  $s = (s_1^2 + s_2^2)^{1/2}$ .

The spectral density of the measurement errors is derived next. Analysis by Bell Aerospace of test data from the gradometers which make up the GGSS yielded the following analytic form for the self-noise spectra:

$$S_{N,N}(f) = r/f^{1.6} + w \quad (4.2-5)$$

where  $f$  is measured in Hz,  $r$  is the red-noise level in  $E^2 \times \text{Hz}$ , and  $w$  is the white-noise floor in  $E^2/\text{Hz}$ .

Temporal frequency,  $f$ , is transferred into spatial frequency,  $s_1$ , through the mapping

$$f = V s_1 \quad (4.2-6)$$

On different data tracks, measurement errors are taken to be independent to give a diagonal error spectral density matrix,  $\phi_{\underline{E},\underline{E}}(\underline{s})$ , with entries

$$\phi_{E_k, E_k}(\underline{s}) = \tau_2 V \left[ \frac{r_k/V^2}{s_1^2} + w_k \right] \quad (4.2-7)$$

for  $-1/(2\tau_1) < s_1 < 1/(2\tau_1)$  and  $k = 1, 2, \dots, 6$ . The values of  $r_k$  and  $w_k$  which were used in the simulation are presented in Table 4.2-1.



TABLE 4.2-1  
RED-NOISE AND WHITE-NOISE PARAMETERS

QUANTITY	DOUBLE-SIDED PSD	SINGLE-SIDED PSD
Red-Noise Level	$1.7 \times 10^{-4} E^2 \text{Hz}$	$1.0 \times 10^{-3} E^2 \text{ rad/sec}$
White-Noise Floor	$55 E^2/\text{Hz}$	$17.5 E^2/(\text{rad/sec})$

Note: The single-sided PSD,  $F_S$ , is defined for frequencies greater than zero. The double-sided PSD,  $F_D$ , is defined for both positive and negative frequencies, but is an even function. For positive frequencies, the relation between  $F_S$  and  $F_D$  is

$$\int_0^{\infty} \phi(\omega) d\omega = (1/\pi) \int_0^{\infty} \phi(f) df$$

or equivalently,  $F_S = F_D/\pi$ , where  $f$  and  $\omega$  are the frequency in Hz and rad/sec, respectively.

Airborne Gravimeter Survey - The geometry of an airborne gravimeter survey was selected to be identical to that of the bidirectional GGSS survey illustrated in Fig. 4.2-2. The cross-track spacing,  $\tau_2$ , is equal to 5 km and the along-track spacing is

$$\tau_1 = V \Delta t \quad (4.2-8)$$

where  $\Delta t$ , the time interval between successive samples, was chosen to be 12 sec. This sampling time corresponds to a 1-km data spacing in the along-track direction.

The transfer function,  $F(\underline{s})$ , from surface anomalous potential to the measured gravity quantities was derived in Ref. 34 for the shipborne gravimeter survey scenario and is identical in form to the aircraft case being considered here. The expression for  $F(\underline{s})$  is

$$F(\underline{s}) = (2\pi s - 2/R) + 2\Omega \cos\theta [i2\pi s_1] G(s_1) \quad (4.2-9)$$

where the two terms are the transfer functions from anomalous surface potential to gravity anomaly and east component of the gravity disturbance vector at the earth's surface, respectively, and

$R$  = the earth radius ( $6.378 \times 10^6$  m)

$\Omega$  = the earth rotation rate ( $0.7292 \times 10^{-4}$  rad/sec)

$\theta$  = the reference latitude

$G(s_1)$  = the navigation transfer function from sensed acceleration to indicated velocity as a function of distance in the east direction, given by

$$G(s_1) = \frac{s_1/(2\pi V)}{2\rho(f_o/V)s_1 + i[s_1^2 - (f_o/V)^2]} \quad (4.2-10)$$

$\rho$  = the navigator damping coefficient

$f_o$  = the Schuler frequency ( $1.971 \times 10^{-4}$  Hz).

The airborne survey measurement error model consists of three error source categories: 1) instrument errors, 2) vertical position uncertainty, and 3) Eötvös correction errors. These three categories are each discussed below.

The gravimeter recordings are corrupted by various error sources, including quantization and instrument noise.

These effects are combined into a single term, I, which is modeled as being independent from measurement point to point and track to track. Correlated error sources (e.g., errors in the Eötvös correction) are treated separately as indicated below. An appropriate rms value for the LaCoste and Romberg gravimeter in an airborne application is  $\sigma_I = 1.0$  mgal. The PSD of I is

$$\phi_{I,I}(\underline{s}) = \tau_1 \tau_2 \sigma_I^2 \quad (4.2-11)$$

Vertical position uncertainty affects the gravity survey results by corrupting the calculated vertical gradient of the field and the aircraft vertical acceleration correction as explained in Ref. 29. The combined effect of this error is represented by a single term, H, which is modeled as being independent from measurement point to point and track to track. An appropriate rms value for this source in the currently configured GGSS, where vertical position will be provided by a GPS-inertial or barometric altimeter mechanization is  $\sigma_H = 20$  m. The PSD of H is

$$\phi_{H,H}(\underline{s}) = \tau_1 \tau_2 (2g_0/R) \sigma_H^2 \quad (4.2-12)$$

where  $2g_0/R = 0.308$  mgal/m.

The Eötvös correction error is caused by the error in the estimate of the east component of velocity obtained from the inertial navigator aboard the survey aircraft. This east velocity error is attributable to the east component of the gravity disturbance vector sensed by the navigator along with random gyro and accelerometer errors. Thus, if airborne gravimetric data are viewed as gravity anomaly measurements, the measurement errors are correlated with the gravity field.

However, an equivalent formulation can be obtained when the data are viewed as noisy measurements of linear combinations of the gravity anomaly and the east component of the gravity disturbance vector modulated by the navigator response. This convention is adopted in Ref. 34 and is also used here since, in this formulation, measurement errors turn out to be independent of the gravity field (see Ref. 34).

Using this formulation, the Eötvös correction error source,  $C$ , is modeled as a white-noise sensed acceleration input with constant spectral density  $q$ . The magnitude of  $q$  is given by

$$q = 8\pi V f_o \rho \sigma_v^2 \quad (4.2-13)$$

where  $\sigma_v$  is the rms velocity error which is about 0.2 m/sec for the currently configured GGSS. Following the development in Ref. 34, the spectral density of the uncorrelated Eötvös correction errors in the interval  $-1/(2\tau_1) < s_1 < 1/(2\tau_1)$  is

$$\phi_{C,C}(\underline{s}) = 4\Omega^2 \cos^2 \theta \tau_2 q |G(s_1)|^2 \quad (4.2-14)$$

In summary, the spectral density of the airborne gravimeter survey measurement errors,  $\phi_{E,E}$ , is given by the sum of the spectral densities of the instrument-related errors (Eq. 4.2-11) and the errors due to vertical position uncertainty (Eq. 4.2-12) and velocity uncertainty (Eq. 4.2-14). Thus,

$$\phi_{E,E}(\underline{s}) = \phi_{I,I}(\underline{s}) + \phi_{H,H}(\underline{s}) + \phi_{C,C}(\underline{s}) \quad (4.2-15)$$

for  $-1/(2\tau_1) < s_1 < 1/(2\tau_1)$  and  $-1/(2\tau_2) < s_2 < 1/(2\tau_2)$ .

### 4.2.3 Results

This section describes the improvement in survey error which can be anticipated by incorporating a gravimeter into the nominal GGSS mechanization. The results which follow were obtained using the multisensor survey analysis and the engineering error models discussed in the previous section. Likewise, the nominal airborne scenario and the North Texas gravity field model were also identified in Section 4.2.2.

Table 4.2-2 contains the rms survey error for three particular survey configurations: 1) nominal GGSS, 2) nominal GGSS with gravimeter aiding, and 3) improved GGSS with gravimeter aiding. The nominal GGSS case is the baseline configuration described in Chapter 1 (i.e., GGSS with GPS aiding). The

TABLE 4.2-2  
GRAVIMETER-AIDING ANALYSIS RESULTS

SURVEY CONFIGURATION	POST-SURVEY RMS DEFLECTION OF THE VERTICAL ERROR (arc sec) (EACH AXIS)		POST-SURVEY RMS VERTICAL GRAVITY DISTURBANCE ERROR (mgal)	
	ALL WAVELENGTHS ( $\lambda$ )	$\lambda < 500$ km	ALL WAVELENGTHS ( $\lambda$ )	$\lambda < 500$ km
Performance Goal	0.20	0.18	1.0	0.90
Nominal GGSS*	0.53	0.12	3.5	0.75
Nominal GGSS with Gravi- meter Aiding	0.13	0.12	0.84	0.75
Improved GGSS with Gravi- meter Aiding	0.11	0.11	0.71	0.71

\*For the case in which no tie-point data are available.

nominal GGSS with gravimeter aiding case represents modifying the baseline GGSS mechanization (as discussed in Section 4.1) to accommodate implementation of a gravimeter on the GGSS platform. Finally, the improved GGSS with gravimeter aiding case reflects the incorporation of very accurate navigation information into the nominal GGSS with gravimeter aiding mechanization.

The post survey rms error represents the contribution of all known error sources, including sampling effects, downward continuation, finite extent, and data processing algorithm errors. The error allocation procedure outlined in Ref. 36 was used to obtain these results. Also indicated in this table for comparison purposes, is DMA's overall performance goal for estimation of the gravity disturbance vector components at the earth's surface. The entries in Table 4.2-2 are separated into two columns for post-survey rms errors over all wavelengths and for only wavelengths less than 500 km. This separation is consistent with DMA's performance goal which was imposed to accommodate manageable testing of the GGSS within its performance limits.

For gravity field wavelengths shorter than 500 km, adding a gravimeter to the nominal GGSS configuration offers no improvement to survey accuracy. However, a substantial improvement in survey accuracy is realized at longer wavelengths. In fact, DMA's overall performance goal (1.0 mgal rms recovery accuracy over all wavelengths) appears achievable with the gravimeter-aided GGSS configuration. This advantage attributes to the gravimeter being complementary to the GGSS. The gravimeter accurately measures the longer wavelengths of the gravity field while the GGSS accurately observes the shorter wavelengths\*.

---

\*Currently, GGSS surveys are envisioned to incorporate surface "tie-point" gravity data as a source of long-wavelength information.

Thus, it is not surprising that no improvement is obtained at the shorter wavelengths by adding a gravimeter to the GGSS mechanization. The GGSS already recovers this part of the gravity field spectrum accurately and a gravimeter does not.

Sensitivity analyses confirm that the vertical position uncertainty is a significant contributor to airborne gravimeter survey error. Furthermore, the Eötvös correction error is also an important and distinct error source. The fourth survey configuration in Table 4.2-2 is included to demonstrate the improvement in survey accuracy which can be expected when these two effects are reduced substantially. In this particular case, the vertical position rms error was reduced to below 1.0 cm and the velocity rms error to 2 cm/sec. These improvements in navigation accuracy yield about five percent improvement in survey accuracy for gravity field wavelengths shorter than 500 km and about 15 percent improvement over all wavelengths. The case in Table 4.2-2 with which these reductions are compared is the nominal GGSS with gravimeter aiding.

To attain the good navigation accuracies noted above, additional mechanization changes in the nominal GGSS are required. Discussions of the use of high-resolution radar, laser, and pressure altimeters, radar terrain clearance, and multiple electronic navigation tracking techniques to reduce the vertical position uncertainty, are presented in Refs. 29 and 31. The use of moving-receiver radio interferometry is another possibility which is especially promising since it offers an improvement in navigation accuracy in all three axes. Additional details of moving-receiver radio interferometry are presented in Chapter 3.

#### 4.3 TECHNICAL RISK AND RECOMMENDATIONS

The expected improvement in survey accuracy over all gravity field wavelengths, which would be realized by incorporating a gravimeter into the nominal GGSS configuration, motivates continuing research in this area. The primary technical risk area relates to the inclusion of an appropriate gravimeter on the GGSS inertially stabilized platform. The platform was designed to accept the Bell BGM-4 model gravimeter, but consideration has also been given to adapting the Bell BGM-3 model.

In addition, technical risk is associated with obtaining the navigation accuracies needed for an improvement in survey accuracy over the shorter wavelengths of the gravity field. Navigation accuracies of that level are currently possible only by exploiting state-of-the-art concepts. Additional analysis and demonstrations of these concepts are recommended.

In particular, TASC recommends that a demonstration of radio interferometry in a moving-receiver application be conducted in the near future. This demonstration would determine if the navigation accuracies predicted herein can be obtained in a practical manner under "real-world" operating conditions. Upon successful demonstration of the moving-receiver radio interferometric concept, consideration should be given to incorporating a gravimeter into the GGSS mechanization to determine if, in fact, relief can be obtained from the burden of emplacing surface gravity and deflection tie points in support of GGSS surveys.



5.

MASTER INS ANALYSIS

The advantages of a high-accuracy inertial navigation system (master INS) used to augment the airborne GGSS were examined as part of the aided-airborne GGSS study. The examination addressed both the aircraft navigation and gradiometer platform stabilization requirements. Several state-of-the-art inertial systems which possess position error rate specifications of better than 0.3 nm/hr CEP were considered as potential GGSS aides. A list of these systems and summary of their practicality for GGSS aiding are presented in Table 5-1.

TABLE 5-1  
SUMMARY OF MASTER INS EVALUATION

A 20450

SYSTEM	COMMENTS
AIRS	COSTLY; EXTENSIVE EFFORT REQUIRED FOR USE IN SURVEY AIRCRAFT
LN-37, CAROUSEL, N-73 AND SKN-2440	EVEN WITH VERTICAL DEFLECTION COMPENSATION, UNAIDED INERTIAL OPERATION WILL PROVIDE NAVIGATION ACCURACIES LESS THAN 200 m ONLY FOR ABOUT ONE HOUR
SPN/GEANS	SLIGHTLY BETTER THAN ABOVE; ABOUT 1.5 HOURS BEFORE NAVIGATION ERRORS EXCEED 200 m
NAS-26	BASED ON LIMITED VAN TEST RESULTS, ADEQUATE (UP TO 16 HOURS) OPERATIONS ARE THEORETICALLY POSSIBLE; FLIGHT TEST RESULTS YIELDED LESS ENCOURAGING RESULTS; AIRCRAFT WOULD HAVE TO BE CONFIGURED WITH STELLAR VIEWING APERTURE; CLOUD COVER WOULD LIMIT OPERATIONS

The key point associated with using a master INS is that in survey areas where the gravity disturbances are typical of the worldwide average, no purely inertial system can meet the GGSS' 100 m CEP requirement for the duration of a mission (at least four hours) without some form of compensation for those gravity effects. This is true even for a "perfect" astroinertial system. (Note that gravity-induced errors are not observable in the star sightings.) Moreover, even by using the gradiometer to perform real-time (or post-survey) vertical deflection compensation, the inherent accuracy of currently planned gradiometer instruments is not adequate to support long-term autonomous navigation. Under the most optimistic assumptions, only about one hour of sufficiently accurate unaided inertial navigation would be possible, compared with 5 to 10 minutes for the presently planned GPS-aided GGSS configuration. This modest extension in operating time does not justify the extensive hardware/software modifications which would be required to incorporate the master INS capability.

Thus, based on the results of this evaluation and on-going navigation analysis of the baseline GGSS configuration, use of a high-accuracy INS as a GGSS aide is unnecessary. Additional support material and technical details of the associated evaluation are presented in Ref. 1.

This report describes the currently planned GGSS implementation along with several variants which were considered to assure long-term success of the GGSS. In particular, a moving-receiver radio interferometer, gravimeter, and master INS are addressed. The sections which follow summarize TASC's key conclusions and identify the areas most promising for continued development.

#### 6.1 CONCLUSIONS

- Conventional GPS pseudoranging techniques are more than adequate for supporting test and operational GGSS missions (the short outages associated with the six-plane, 18-satellite constellation are due to poor geometry and are inconsequential to GGSS deployment as currently configured)
- GPS backup modes based on the use of an atomic clock and moderately accurate altimeter will provide adequate extended coverage and geometry appropriate for GGSS navigation during testing
- Moving-receiver radio interferometry offers a low-cost, low-risk backup position measurement capability especially well-suited for GGSS surface testing
- The GGSS Program offers a unique opportunity for demonstrating the gravity measurement capability associated with moving-receiver radio interferometry

- For short-wavelength gravity recovery, substantial improvements in navigation accuracy (such as would be provided by radio interferometry to GPS) are necessary for gravimeter aiding to yield better performance than that possible from a nominal GGSS survey, as well as a reduction in required surface tie-point data
- State-of-the-art master INSs offer diminished incremental returns in autonomous navigation compared with the baseline GPS-aided GGSS configuration.

## 6.2 RECOMMENDATIONS

TASC recommends the following next steps:

- Specify appropriate testing procedures to assure confidence in the GPS Navigator during GGSS testing (see Section 2.1)
- Incorporate moving-receiver radio interferometry into the GGSS Program as a backup position measurement capability during surface testing (see Section 3.4.2); to minimize program delays; at the present time, configure only the base station with the necessary hardware (GPS receiver/recorder, atomic clock, weather sensor) - the moving vehicle can be augmented later, if necessary
- Augment the GGSS test program to accommodate demonstrations of gravity measurement using radio interferometric principles (see Section 3.4.2)
- Support the development of weather sensors which will very accurately determine the spatial variations of tropospheric refractivity (see Section 3.4.2)
- Perform application-oriented analysis of moving-base gravimetric surveys (both theoretical analysis and data processing) - see Section 4.2.2.

## APPENDIX A

### GPS DESCRIPTION AND ANALYSIS RESULTS DISCUSSION

This appendix contains a detailed discussion of the Global Positioning System (GPS). Section A.1 describes the orientation of the satellites which make up the space segment and defines the attributes of the transmitted signals which will be received by the user segment. The conversion of these signals into positioning and navigation information is explained and the significance of satellite geometry on navigation accuracy is quantified.

Section A.2 treats the analytical problem of modeling GPS satellite orbits. Basic orbital relationships and parameters are established in terms of idealized elliptical orbits, and perturbation theory is introduced to account for the effect of the ellipsoidal shape of the earth on satellite orbits. Common features of GPS satellite orbits are examined, and the problem of simulating a constellation of satellites is considered.

Section A.3 presents GPS analysis results involving positioning and navigation accuracies which can be expected when the complete 18-satellite constellation is operational. Note that the GPS operational schedule corresponds to the currently planned timeframe for deployment of the GGSS for operational surveying. Predicted satellite visibility and geometry are emphasized throughout the discussion of the analysis results.

#### A.1 SYSTEM DESCRIPTION

The Space Segment - Current plans call for the deployment of 18 primary GPS satellites in six orbital planes. Each

plane will be inclined at 55 deg to the equator. In addition, three spares will be placed in orbit to insure a high degree of system availability. The current schedule for deployment is provided in Fig. A.1-1 and is based on material presented in Ref. 8. The current airborne GGSS testing schedule is also indicated on this figure. As is clear from Fig. A.1-1, back-up navigation modes must be considered to assure efficient and successful GGSS testing.

The current test configuration consists of six "system validation" or Block I satellites. These satellites are in orbits inclined at 63 deg and are positioned to provide good geometry for a user at the Yuma Proving Ground. Table A.1-1 summarizes the Block I GPS orbital parameters; Section A.2 defines the associated orbital parameters and explains their significance.

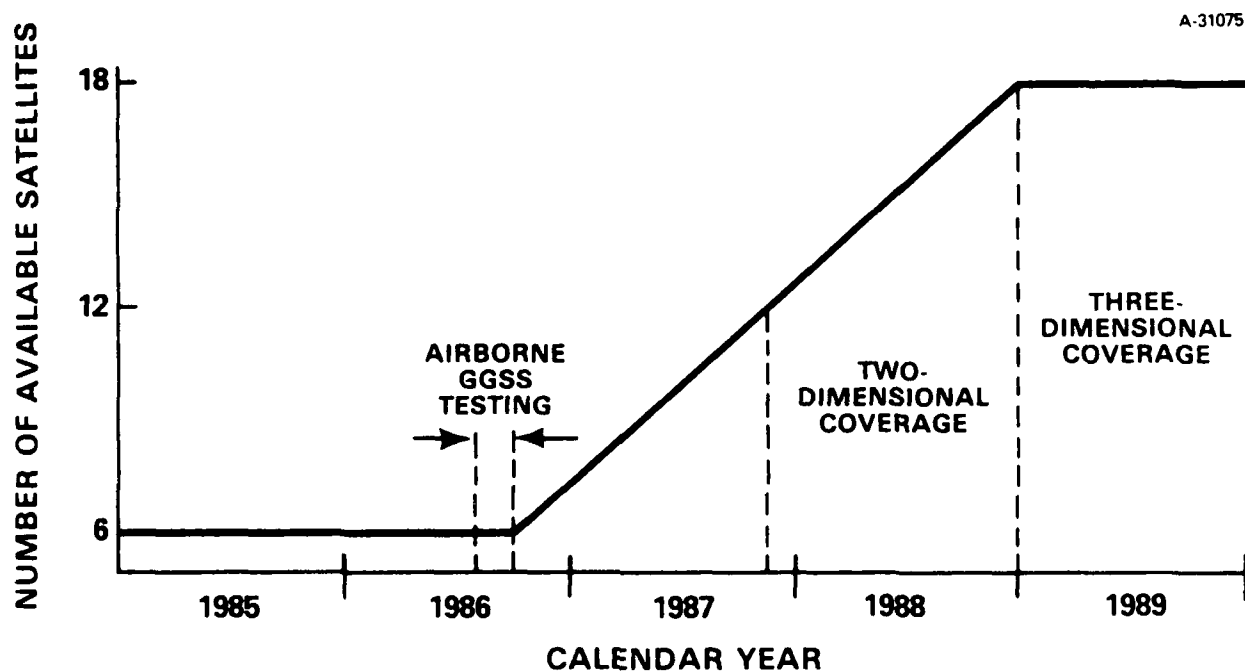


Figure A.1-1 GPS Satellite Deployment Schedule

TABLE A.1-1  
BLOCK I GPS ORBITAL PARAMETERS

T-5371

POSITION NUMBER	RIGHT ASCENSION OF NODE (deg $\pm$ 2 deg)	LONGITUDE OF NODE (deg E $\pm$ 2 deg)	TIME OF NODE (hr:min:sec:GMT $\pm$ 16 min)	INCLINATION (deg $\pm$ 1)	ANOMALY (deg $\pm$ 2 deg)
1	202	227.0	3:40:16	63	53
2	202	248.5	2:19:25	63	96
3	202	269.5	0:51:18	63	138
4	82	130.5	2:11:26	63	97
5	82	152.0	0:40:51	63	140
6	82	353.0	11:15:21	63	182

Note: Values apply to time at first ascending node referred to 1 July 1980.

Transition from the Block I to the operational (Block II) configuration involves considering an appropriate build-up strategy. This strategy must take into account ongoing testing requirements at Yuma and the launch windows associated with the planned missions of the space shuttle which currently is designated as the launch platform for these satellites. One such strategy is described in Ref. 37 and illustrated in Fig. A.1-2. The rephasing of the Block I satellites into their Block II positions shown in Fig. A.1-2 is based on this particular strategy.

Table A.1-2 summarizes the Block II orbital parameters. Three satellites will be deployed in each of six orbital planes which will be equally spaced 60 deg apart in longitude. The satellites in each plane will also be uniformly spaced 120 deg apart. The relative phasing of satellites from one plane to the next will be 40 deg (i.e., a satellite in one plane will have another satellite 40 deg "ahead" or North of it in the plane directly to the east, as shown in Fig. A.1-2. The benefits associated with this six-plane arrangement of satellites, in terms of continuous intervals of geographic coverage and

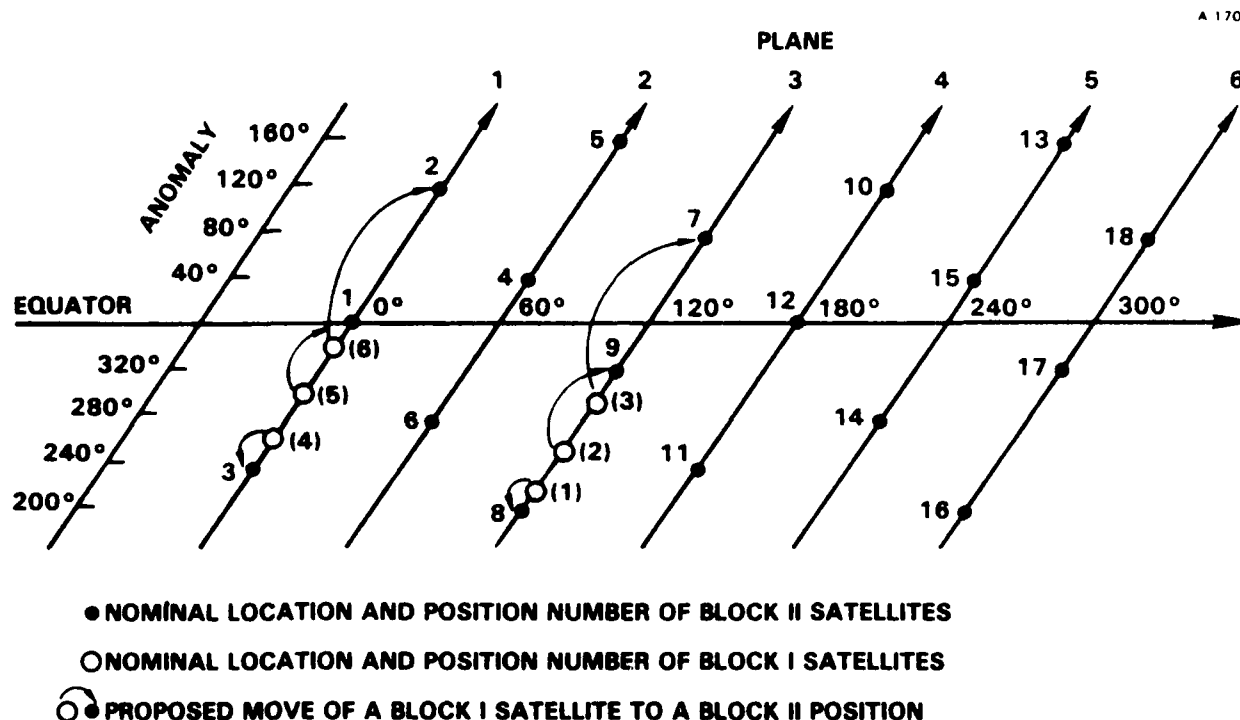


Figure A.1-2 A Strategy for Buildup of Operational GPS Configuration (Ref. 37)

geometry of the satellites in view relative to the users, are discussed in Refs. 38 and 39.

The satellites will be positioned in near-circular orbits at altitudes of approximately 20,183 km. This altitude was selected to provide a period exactly one-half synchronous (i.e., 11 hr 57 min 58.3 sec). Thus, each satellite will pass over the same point on the earth every 23 hr 55 min 56.6 sec (a sidereal day), or in other words the satellites will pass over the same location about four minutes earlier each day.

The User Segment - Each GPS satellite continuously broadcasts a unique navigation message which can be used by the user equipment to determine the navigation solution. The message consists of transmitted signals characterized by two components:



TABLE A.1-2  
BLOCK II GPS ORBITAL PARAMETERS

ORBITAL PLANE NUMBER	SATELLITE POSITION NUMBER	RELATIVE ANOMALY (deg)	RELATIVE RIGHT ASCENSION (deg)	RIGHT ASCENSION OF ASCENDING NODE (deg)*	LONGITUDE OF ASCENDING NODE (deg)
1	1	0	0	30	0,180
	2	120			240,60
	3	240			300,120
2	4	40	60	90	260,80
	5	160			320,140
	6	280			20,200
3	7	80	120	150	340,160
	8	200			40,220
	9	320			100,280
4	10	120	180	210	60,240
	11	240			120,300
	12	0			180,0
5	13	160	240	270	140,320
	14	280			200,20
	15	40			80,260
6	16	200	300	330	220,40
	17	320			280,100
	18	80			160,340
1	19	30	0	30	95,15
5	20	310	240	270	215,35
3	21	170	120	150	25,105

\*Referenced to astronomical coordinates of 1950.0 as of 0 hr 0 min GMT on 1 July 1985 and regressing at -0.04009 deg/day.

- (1) A coarse/acquisition (C/A) signal and a precise (P) signal centered about the Link 1 L-band ( $L_1$ ) carrier frequency
- (2) Either the C/A or P signal centered about the Link 2 L-band ( $L_2$ ) carrier frequency.

The carrier frequencies were selected to be integral multiples of the basic satellite clock frequency of 10.23 MHz. In particular,

$$L_1 = 1575.42 \text{ MHz (19-cm wavelength)} = 154 \times 10.23 \text{ MHz}$$

$$L_2 = 1227.60 \text{ MHz (24-cm wavelength)} = 120 \times 10.23 \text{ MHz.}$$

The dual-frequency operation is provided because the signals are delayed in passing through the ionosphere by an amount inversely proportional to the frequency squared. Measurements at two frequencies can be used to compensate for this ionospheric delay. Additional details relevant to the unique characteristics and attributes of these basic signals are provided in Ref. 4, 5, 6, and 40.

The navigation message includes the following information:

- Satellite status
- Satellite clock correction and ephemeris parameters
- Ionosphere propagation delay model coefficients
- Almanac information including the ephemerides and status of all other satellites.

This information is employed in the user equipment to make "pseudorange" measurements to the selected four satellites. The term pseudorange is used since the measurements contain a

bias error due to a user's lack of a precise time reference synchronized to GPS time, and is given by

$$R_i = r_i + c \Delta t_i + c(\Delta t_u - \Delta T_i) \quad (\text{A.1-1})$$

where

$r_i$  = true range to  $i^{\text{th}}$  satellite

$c$  = speed of light

$\Delta t_i$  = propagation delays

$\Delta t_u$  = user's clock offset from GPS time

$\Delta T_i$  =  $i^{\text{th}}$  satellite's clock offset from GPS time.

GPS receivers actually estimate both code phase and carrier phase while tracking a signal in their most accurate mode. By differencing beginning and ending pseudorange measurements made over a period when carrier phase lock is achieved, an "integrated doppler" measurement of "delta range" is possible. When the doppler processing period is short and the delta-range measurement is divided by the period, the measurement is termed pseudorange-rate. Pseudorange-rate is the time-derivative of pseudorange and is a measure of the rate at which the range from the user to the GPS satellite is changing, plus the frequency offset of the user clock. Just as clock phase offsets or time periods are measurable in units of distance, so frequency offsets are measurable in units of velocity, by multiplying by the speed of light.

Upon measuring the pseudorange to four satellites, the user equipment can compute the position of these satellites using the transmitted ephemeris data. Three-dimensional user position and precise time can then be derived from the pseudorange measurements and satellite positions. This is a straightforward matter involving the solution of four simultaneous nonlinear equations in four unknowns (see Ref. 6).

If the errors in the four simultaneous pseudorange measurements are independent and of equal variance, then the navigation errors resulting from the deterministic solution can be related to the pseudorange errors by the geometric dilution of precision (GDOP). GDOP refers to the four-dimensional root-sum-square (rss) combination of position and time errors,

$$\text{GDOP} = \sqrt{\sigma_N^2 + \sigma_E^2 + \sigma_D^2 + \sigma_t^2} \quad (\text{A.1-2})$$

where

$\sigma_N, \sigma_E, \sigma_D$  = rms user position errors in a local-level North, East, Down coordinate frame

$\sigma_t$  = rms user time offset.

Similar expressions exist for the dilution of precision in three-dimensional position (PDOP), horizontal position (HDOP), vertical position (VDOP), and time (TDOP). Furthermore, the standard deviation of the resultant navigation error is equal to the appropriate dilution of precision factor times the standard deviation of a single pseudorange error ( $\sigma_r$ ). Thus, the three-dimensional rms position error is given by

$$\sigma_p = \sigma_r \times \text{PDOP} \quad (\text{A.1-3})$$

The value of PDOP has a geometric interpretation as well. Consider a hexahedron-shaped figure with the user position located at the bottom indice and the position of four satellites located at the other indices (see Fig. A.1-3). The PDOP value is inversely related to the volume encompassed by this hexahedron. Thus, the volume is maximized (and PDOP is minimized) when one satellite is at the user's zenith and the other three are separated by 120 deg and are as low on the horizon as the user's antenna elevation angle permits (see Ref. 11).

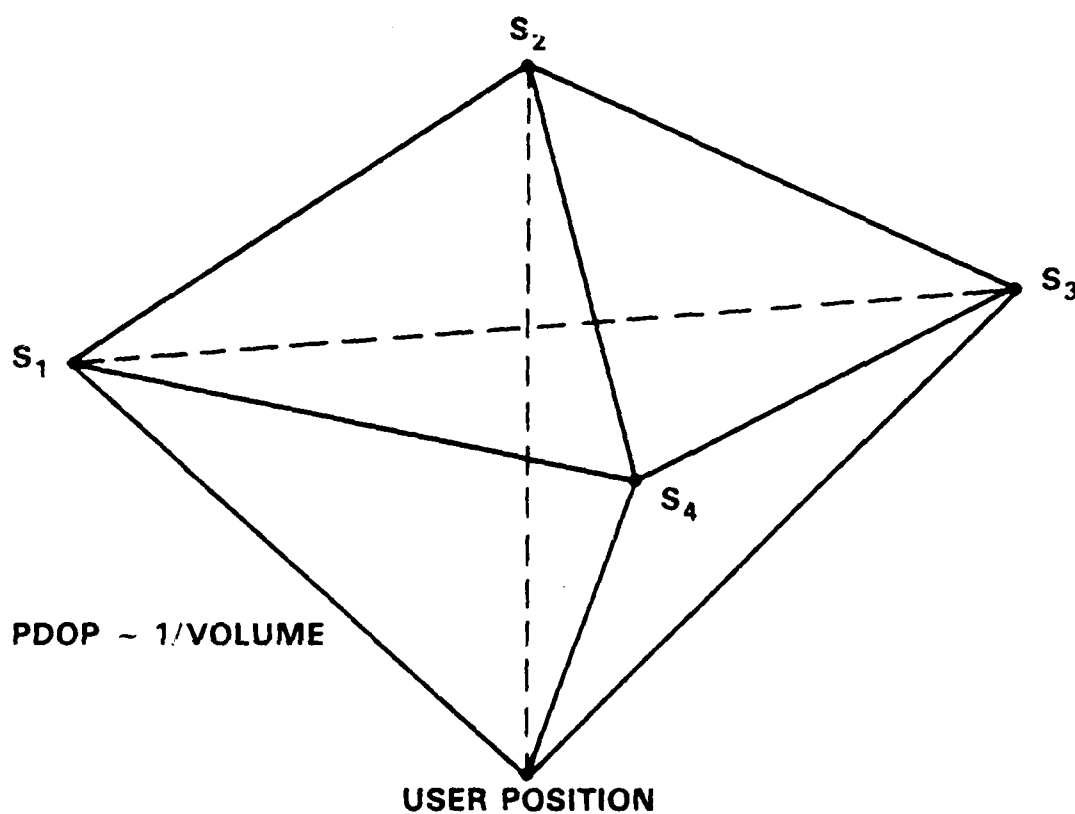


Figure A.1-3 A Geometric Interpretation of PDOP

As noted earlier in this section, during GGSS testing there will be only six satellites available. This situation will lead to limited viewing times when four satellites will be visible simultaneously. However, by equipping the user with a precise clock, three-satellite navigation can be realized. The stability of the clock is application-dependent and thus, necessarily a function of the maximum allowable rms position error and clock update interval. Techniques appropriate for updating the clock include (Refs. 41 and 42):

- Tracking four GPS satellites and deriving the nominal navigation solution
- Tracking a single GPS satellite from a known location and extracting the appropriate information from the navigation message

- Conventional time-transfer methods.

As expected, the resultant TDOP is dependent on the accuracy of the particular clock update technique. For example, for the four-satellite method,

$$\text{TDOP} = \sigma_b / \sigma_r \quad (\text{A.1-4})$$

where  $\sigma_b$  is the clock bias rms error associated with the last clock update. The mathematical basis for computing the rms user position error as a function of three-satellite geometry and clock stability is provided in Ref. 41.

The preceding discussion for the three-satellite case can be naturally extended to apply to situations when only two satellites are visible. Again, a precise clock is necessary, but now an altimeter must also be included to provide the vertical position information necessary for completing the full navigation solution. Analogous to Eq. A.1-4,

$$\text{VDOP} = \sigma_a / \sigma_r \quad (\text{A.1-5})$$

where  $\sigma_a$  is the rms error of the altimeter measurement.

## A.2 ORBIT CHARACTERISTICS

### A.2-1 General Orbital Relationships

Before discussing the orbital trajectories of GPS satellites, it is useful to review briefly the general properties of earth satellite orbits (Ref. 43). Of the several forces that combine to shape such orbits, by far the most important is the earth's gravitational attraction, with lesser

contributors including atmospheric drag, solar radiation pressure, and gravitational effects due to the sun, the moon, and the planets. The earth's gravitational attraction can be considered as a sum of terms, with the dominant, central term being the simple, inverse-square, point-mass attraction. If this central gravitational term were the only force on a small, relatively massless satellite, then the satellite orbit would be a perfect ellipse fixed in an earth-centered inertial space with one focus at the center of mass of the earth. Actual satellite orbits are nearly, but not exactly, ellipses, and the orbits tend not to remain fixed in inertial space over long periods of time.

It takes, in general, six parameters to describe the state of a point-mass satellite. One such set of parameters consists of the vector components of satellite position and velocity in either an inertial or an earth-fixed coordinate frame. Such a set of parameters is very useful in computations involving the relative geometry between the satellite and other points in space. But it is not a useful set for conceptualizing the satellite orbit or for understanding orbital propagation (evolution), because all six vector components change rapidly in a complex manner. A mathematically equivalent set of six parameters is more useful in describing the satellite orbit, a set of parameters related to the perfectly elliptical orbit.

Three of the parameters describe the size and shape of the ellipse and the position of the satellite in the ellipse. These parameters are the semimajor axis length  $a$ , the eccentricity  $e$ , and the (time-varying) true anomaly angle  $f$ , all illustrated in Fig. A.2-1. The remaining three angular parameters describe the orientation of the ellipse with respect to the inertial coordinate frame. They are the orbital

inclination  $I$ , the right ascension of the ascending node  $\Omega$ , and the argument of perigee  $\omega$ , all illustrated in Fig. A.2-2. It should be noted that in this appendix the right ascension of the ascending node (the node is the point where the satellite orbit crosses the earth's equator going from south to north) is measured from the x-axis of a basic inertial coordinate frame defined in Fig. A.2-3. The orientation of this x-axis with respect to the fixed stars is somewhat arbitrary, depending on where the Greenwich meridian is at the epoch ( $t_0$ ) when the inertial coordinate frame is conceptually established as coincident with earth-fixed coordinates. Most works (including Ref. 44) measure the right ascension from the vernal equinox (which is the ascending node of the sun under the fictitious concept that the sun is orbiting the earth).

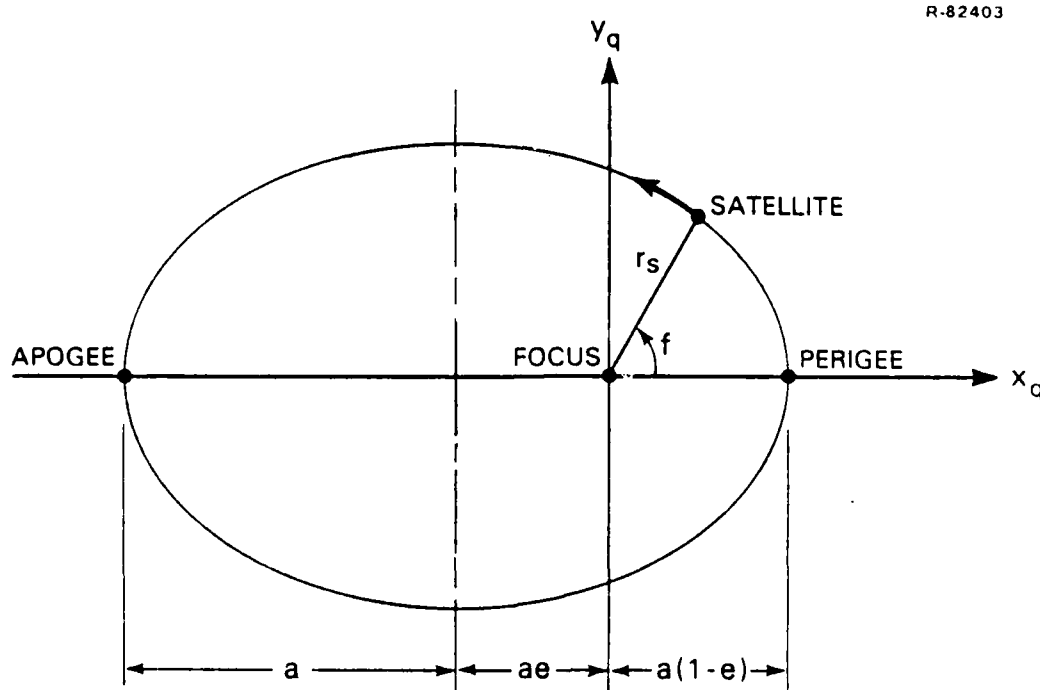


Figure A.2-1 Orbital Ellipse



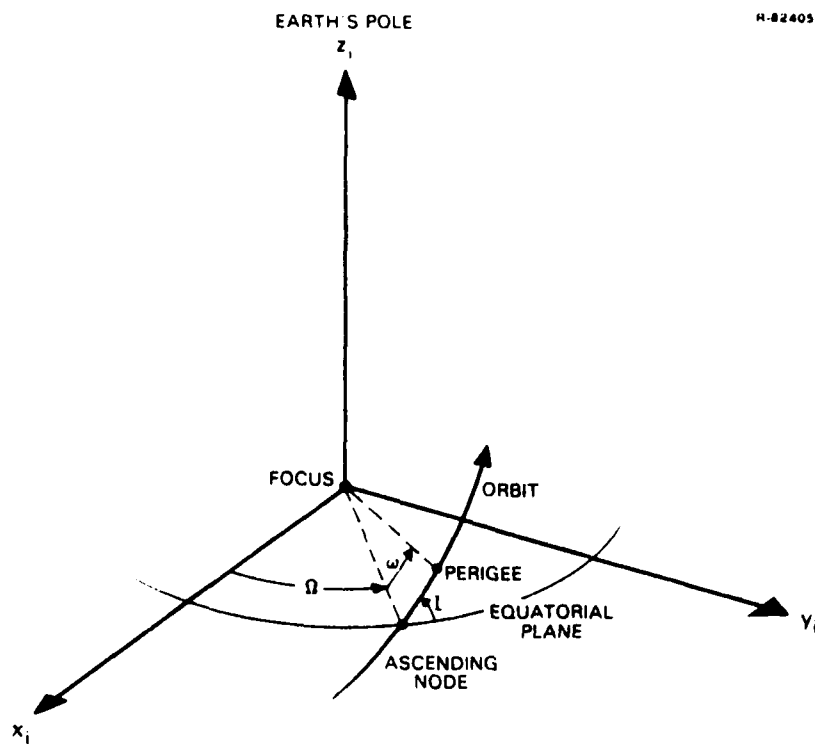


Figure A.2-2 Orbital Orientation

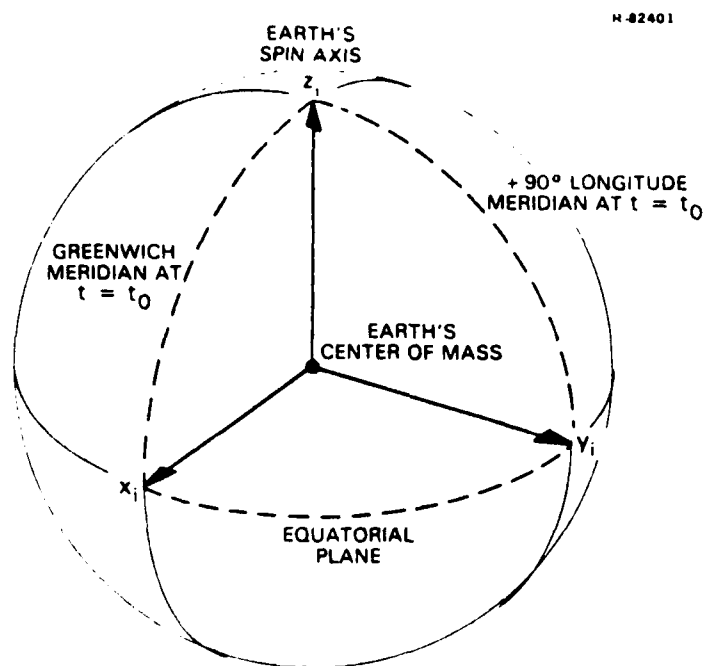


Figure A.2-3 Inertial Coordinates

Also noted in Fig. A.2-1 are coordinate axes of the "q" frame. The relationship between the q-frame and the basic inertial frame is provided by the three orientation parameters, and the matrix that transforms vectors expressed in the i-frame to an expression in the q-frame is given by

$$R_{qi} = R_3(\omega)R_1(I)R_3(\Omega) \quad (A.2-1)$$

Explicitly,

$$R_{qi} = \begin{bmatrix} C_\Omega C_\omega - S_\Omega C_I S_\omega & S_\Omega C_\omega + C_\Omega C_I S_\omega & S_I S_\omega \\ -C_\Omega S_\omega - S_\Omega C_I C_\omega & -S_\Omega S_\omega + C_\Omega C_I C_\omega & S_I C_\omega \\ S_\Omega S_I & -C_\Omega S_I & C_I \end{bmatrix} \quad (A.2-2)$$

where the C and S designations represent the cosine and sine trigonometric functions, respectively.

The motion of the satellite in its elliptical orbit will not be derived (see Ref. 44), but key results will be summarized. The position vector from the center of mass of the earth (the focus of the elliptical orbit) to the satellite is given by

$$(\bar{r}_s)_q = \begin{bmatrix} r_s C_f \\ r_s S_f \\ 0 \end{bmatrix}_q \quad (A.2-3)$$

where  $r_s$  is the magnitude of the radius vector. In terms of the elliptical parameters

$$r_s = \frac{a(1-e^2)}{(1+eC_f)} \quad (A.2-4)$$

Of the six parameters describing the satellite in its idealized elliptical orbit, five are constants, and only one, the true anomaly ( $f$ ) changes with time. The way in which the true anomaly changes with time is somewhat complex, and is best described by defining two new terms: the eccentric anomaly  $E$ , and the mean anomaly  $M$ . All of the three anomalies are defined to be zero when the satellite is at perigee.

The mean anomaly changes at a constant rate

$$M = n(t - t_p) \quad (\text{A.2-5})$$

where  $t_p$  is the time of perigee, and  $n$  is the mean motion to be discussed later. The eccentric anomaly is related to the mean anomaly via Kepler's Equation

$$E - eS_E = M \quad (\text{A.2-6})$$

The relationship between the eccentric and the true anomalies is best provided by the equations

$$r_s C_f = a(C_E - e) \quad (\text{A.2-7})$$

$$r_s S_f = a \sqrt{1 - e^2} S_E \quad (\text{A.2-8})$$

A geometric justification for the definition of the eccentric anomaly is provided in Ref. 43. An important point to note here is that if the satellite orbit is circular then the eccentricity  $e$  is zero, and the true anomaly, the eccentric anomaly, and the mean anomaly are all identical.

The rate of the mean anomaly, the mean motion ( $n$ ), is related to the earth's gravitational constant in the assumed central force term ( $\mu_e$ ) and to the orbit semimajor axis ( $a$ ) as

$$n = \sqrt{\mu_e/a^3} \quad (\text{A.2-9})$$

The mean motion shows up in the expression for the satellite (inertial) velocity vector in the q-frame

$$(\underline{v}_s)_q = \frac{na}{\sqrt{1-e^2}} \begin{bmatrix} -S_f \\ e + C_f \\ 0 \end{bmatrix}_q \quad (\text{A.2-10})$$

Anticipating the fact that GPS satellite orbits are nominally circular, the foregoing expressions can be simplified in two ways. The first way is by setting the orbital eccentricity to zero. The second simplification comes from the fact that there is no perigee in a circular orbit, so the arbitrary argument of perigee can also be set to zero, and the various anomalies (now all identical) can be measured from the ascending node. For a reminder, denote the anomalies all by the symbol A. The desired expressions are the satellite position and velocity components in the inertial coordinate frame in terms of the elliptic orbit parameters. They are:

$$r_s = a \quad (\text{A.2-11})$$

$$(\underline{r}_s)_i = r_s \begin{bmatrix} C_\Omega C_A - S_\Omega C_I S_A \\ S_\Omega C_A + C_\Omega C_I S_A \\ S_I S_A \end{bmatrix}_i \quad (\text{A.2-12})$$

$$v_s = na \quad (\text{A.2-13})$$

$$(\underline{v}_s)_i = v_s \begin{bmatrix} -C_\Omega S_A - S_\Omega C_I C_A \\ -S_\Omega S_A + C_\Omega C_I C_A \\ S_I C_A \end{bmatrix}_i \quad (\text{A.2-14})$$

The equivalent expressions in earth-fixed coordinates are identical except that the right ascension  $\Omega$  must be replaced by  $\Omega'$ , where

$$\Omega' = \Omega - \theta_e \quad (\text{A.2-15})$$

$\theta_e$  being the earth's sidereal angle defined by

$$\theta_e = \omega_e(t - t_0) \quad (\text{A.2-16})$$

where  $\omega_e$  denotes the angular velocity of the rotating earth with respect to inertial space.

The next step in this argument is to connect idealized elliptical orbits with real, nearly elliptical orbits. The connection is provided, on an instantaneous basis, by the relationship between the elliptical orbit parameters and the satellite position and velocity components in inertial space just derived. At any instant in time the satellite has some definite position and velocity components in the basic inertial frame. There is, at the same instant, some set of elliptical orbit parameters that correspond to the same position and velocity components via the relationships above. This elliptical orbit is termed an instantaneous osculating orbit. Thus, any real orbit (of the nearly elliptical category -- as opposed to the nearly hyperbolic) can be defined in terms of a set of elliptical orbit parameters. In an idealized elliptical orbit, five of the six orbit parameters are constants, while one changes with time. In a real orbit described by elliptical orbit parameters, all six parameters are subject to change with time. The advantage of using the elliptical parameters is that five of the parameters should change very slowly.

The chief disturbance of the elliptical orbits of most high-altitude satellites (those of reasonably high density) is

the term in the earth's gravitational field resulting from the ellipsoidal figure of the earth. The coefficient of this term, often noted as  $C_{20}$  (or  $-J_2$ ), is over 100 times as great as the coefficient of any other (except the central) term in the spherical harmonic expansion of the earth's gravitational potential. The effect of the earth's equatorial bulge on satellite orbits can be computed approximately by orbital perturbation theory. Ignoring small cyclic effects during a single orbit and concentrating on long-term trends, the results are that the bulge does not alter the orbit semimajor axis, the eccentricity, or the inclination angle, but does cause trends in the argument of perigee and the right ascension, and alters the value of the mean anomaly rate slightly. Directly from Ref. 44, simplified for a circular orbit, the perturbed results are

$$\dot{\omega} = \frac{3nC_{20}a_e^2}{4r_s^2} (1-5C_I^2) \quad (\text{A.2-17})$$

$$\dot{\Omega} = \frac{3nC_{20}a_e^2}{2r_s^2} C_I \quad (\text{A.2-18})$$

$$\dot{M} = n - \frac{3nC_{20}a_e^2}{4r_s^2} (3C_I^2 - 1) \quad (\text{A.2-19})$$

It might seem strange to express a rate of change of the argument of perigee for a circular orbit that has no perigee and for which it was previously assumed that the argument of perigee was zero. A better way to think about the previous manipulations in this perturbed case is that the argument of perigee is initialized at zero, and the "common" anomaly ( $A$ ) is actually the sum of the argument of perigee and the mean anomaly (or the eccentric anomaly, or the true anomaly). Now

$$\dot{A} = \dot{M} + \dot{\omega} \quad (\text{A.2-20})$$

$$\dot{A} = n - \frac{3nC_{20}a_e^2}{4r_s^2} (4C_I^2 - 1) \quad (\text{A.2-21})$$

The values of the two gravitational constants involved in the above relationships, the gravitational constant  $\mu_e$  and the second degree zonal coefficient  $\bar{C}_{20}$ , are defining parameters of the WGS 72 ellipsoid, and are

$$\mu_e = 3.986005 \times 10^{14} \text{ m}^3/\text{sec}^2$$

$$\bar{C}_{20} = -4.841605 \times 10^{-4}$$

The unnormalized coefficient used in Ref. 44 and in the above equations is related to the normalized version by

$$C_{20} = \sqrt{5} \bar{C}_{20} \quad (\text{A.2-22})$$

so that

$$C_{20} = -1.0826158 \times 10^{-3}$$

Because this value is negative, it is apparent from Eq. A.2-18 that all orbits with inclination angles less than 90 deg will have a decreasing right ascension. That is, their orbit planes will rotate slowly in a direction opposite to the earth's rotation rate. To proceed further, it is necessary to know more about the nominal orbit parameters, so this discussion will be suspended until some details of the GPS satellite orbits are introduced.

### A.2.2 Common Features of GPS Satellite Orbits

In the Global Positioning System (GPS), essentially line-of-sight (L-band) navigation signals are broadcast by a

number of earth orbiting satellites. The set of satellites is termed the GPS constellation. Specific characteristics of the current test and planned operational GPS constellations are identified in Section A.1.

All of the GPS satellites will be in nominally circular "12-hour" orbits. The common orbital radius of the satellites is chosen, as will be shown, to yield an orbital period of very nearly one-half of a sidereal day. A sidereal day is the time required for the earth to complete one full rotation with respect to the fixed stars, and since the satellites complete two orbital revolutions in the same time, the positions of the satellites relative to the earth are periodic, with a period of very nearly one sidereal day (one ordinary day less about four minutes). The "very nearly" qualifier is added because, as was noted in the previous section, the satellite orbits are not quite fixed with respect to the stars, but the orbital planes rotate slowly due primarily to the oblateness of the earth.

The GPS satellites will all have the same nominal orbital inclination of 55 deg (it is 63 deg in the current test constellation). Using the approximate perturbation results of the previous section, it is possible to compute the nominal radius and period of the GPS satellite orbits. The key equation can be deduced from the fact that the satellite ground tracks must be periodic. Thus, Eqs. A.2-12 and A.2-14 (with  $\Omega'$  replacing  $\Omega$  so that they refer to the earth-fixed frame rather than the inertial frame) must be periodic. This can only happen if the anomaly  $A$  and the earth relative "right ascension"  $\Omega'$  share a common period. For the "12-hour" orbits, the anomaly rate must be twice the effective rate of the earth rotation with respect to the GPS satellite orbit planes. In symbols,



$$\dot{A} = -2 \dot{\Omega}' = 2(\dot{\theta}_e - \dot{\Omega}) \quad (\text{A.2-23})$$

Upon substituting Eq. A.2-21 for  $\dot{A}$  and Eq. A.2-18 for  $\dot{\Omega}$ , recalling that the rate of change of the sidereal angle  $\theta_e$  is just the sidereal earth rate  $w_e$ , using Eq. A.2-9 for the mean motion  $n$ , and rearranging yields

$$\frac{2w_e}{\sqrt{\mu_e/a_e}^3} = \left(\frac{a_e}{r_s}\right)^{3/2} \left[ 1 - \left(\frac{a_e}{r_s}\right)^2 \frac{3C_{20}}{2} (4C_I^2 - 2C_I - 1) \right] \quad (\text{A.2-24})$$

Everything in this relationship is known except the GPS satellite radius  $r_s$ . Numerically solving for the ratio  $(r_s/a_e)$  yields

$$(r_s/a_e) = 4.1642875$$

or

$$r_s = 26560387 \text{ m}$$

Having the GPS satellite allows some other relevant quantities to be computed. The satellite orbital rate is

$$\dot{A} = 1.4585797 \times 10^{-4} \text{ rad/sec}$$

the orbital period is

$$T_{\text{GPS}} = 2\pi/\dot{A} = 11^{\text{h}} 57^{\text{m}} 57.42^{\text{s}} \quad (\text{A.2-25})$$

the ground track period is

$$2T_{\text{GPS}} = 23^{\text{h}} 55^{\text{m}} 54.84^{\text{s}}$$

the right ascension rate is

$$\dot{\Omega} = -7.834 \times 10^{-9} \text{ rad/sec}$$

$$\dot{\Omega} = -14.17 \text{ deg/yr}$$

the mean motion is

$$n = 1.4585366 \times 10^{-4} \text{ rad/sec}$$

and the satellite orbital velocity is

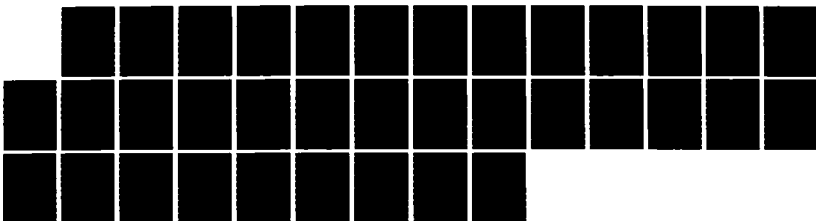
$$v_s = 3873.93 \text{ m/sec}$$

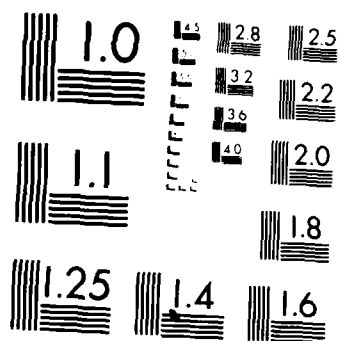
An extensive computer simulation, accounting for numerous disturbing effects, beyond the major one of the earth's oblateness, would result in values for the key parameters that differ very little from those presented above.

#### A.2.3 Simulating the GPS Satellite Constellation

The longitude and time connections between the operational GPS satellite constellation and earth-fixed coordinates are not yet finalized. In order to parameterize these connections and understand them more fully, it is useful to introduce a new parameter: the longitude of the ascending node. Up to this point, the location of the ascending node of a satellite orbit has been described by its right ascension angle measured from the  $x_i$  axis of the basic inertial frame (the location of the Greenwich meridian at some arbitrary time  $t_0$ ). The right ascension parameter is most useful when dealing with idealized elliptic orbits where the right ascension does not vary with time. For GPS satellite orbits, whose most constant aspect is their repeating ground tracks, the longitude of the ascending

AD-A170 749 AIDED-AIRBORNE GRAVITY GRADIMETER SURVEY SYSTEM (AGSS) 2/2  
STUDY(U) ANALYTIC SCIENCES CORP READING RA  
S J BRZEZOWSKI ET AL. MAR 86 TASC-TR-4769-2  
UNCLASSIFIED AFGL-TR-86-8059 F19628-83-C-0146 F/G 1777 NL





MICROCOPY RESOLUTION TEST CHART  
NATIONAL BUREAU OF STANDARDS 1963-A

node is more useful. It is defined to be the satellite longitude, measured from the Greenwich meridian, at the instant when the satellite is at its ascending node. Since the satellite is at its ascending node once each 12 hours or so, there is a sequence of longitudes of the ascending nodes. But for GPS satellites, this sequence is just two values, differing by 180 deg, repeated alternately. One of these two values, the one greater than or equal to zero and less than 180 deg, can arbitrarily be selected as the primary longitude of the ascending node. The longitude of the ascending node for the #1 GPS Satellite is used to parameterize the longitude connection between the satellite constellation and the earth, and is denoted here by  $\lambda_{\text{GPS}}$ .

The time connection parameter is the time of the ascending node of the #1 GPS Satellite, denoted by  $t_{\text{GPS}}$ . Of course, there is a sequence of such times, separated by approximately 24 hours, since it is the times of the primary nodes that have longitude  $\lambda_{\text{GPS}}$  that are being considered. Any member of the sequence will serve to establish the time connection. It is often easiest to use that member closest to the "time zero" that establishes the basic inertial reference system with respect to earth-fixed coordinates.

In terms of these new parameters, the right ascension of the ascending node of the #1 GPS Satellite, at the time  $t_{\text{GPS}}$ , is given by

$$\Omega_{\text{GPS}} = \lambda_{\text{GPS}} + w_e(t_{\text{GPS}} - t_0) \quad (\text{A.2-26})$$

At any time  $t$ , the right ascension of the  $j^{\text{th}}$  GPS satellite is given by

$$\Omega_j(t) = \Omega_{\text{GPS}} + \Omega_{rj} + \dot{\Omega}(t - t_{\text{GPS}}) \quad (\text{A.2-27})$$

where  $\Omega_{rj}$  is the relative right ascension of the  $j^{\text{th}}$  satellite (tabulated in Table A.1-2 or otherwise known from the constellation), and  $\dot{\Omega}$  is the constant, very small, right ascension rate given following Eq. A.2-25.

The anomaly of the  $j^{\text{th}}$  GPS satellite at any time  $t$  is given by

$$A_j(t) = A_{rj} + \dot{A}(t-t_{\text{GPS}}) \quad (\text{A.2-28})$$

where  $A_{rj}$  is the relative anomaly (tabulated in Table A.1-2 or otherwise known from the constellation), and  $\dot{A}$  is the not-so-small, constant value given just prior to Eq. A.2-25.

Table A.2-1 summarizes the data and calculations necessary to simulate a GPS constellation in terms of the positions and velocities of its satellites in the basic inertial frame. For short time period simulations, the propagation equation for the satellite right ascensions can be used to initialize the right ascension values which can subsequently be treated as constants, avoiding the reevaluation of numerous trigonometric functions as time passes. Further, for a fixed time-step simulation, the sine and cosine addition formulas can be used to propagate the sines and cosines of the satellite anomalies, again avoiding the trigonometric function computations. That is, over a fixed time step  $\Delta t$ , each satellite anomaly advances by an amount

$$\Delta A = \dot{A} \Delta t \quad (\text{A.2-29})$$

TABLE A.2-1  
COMPUTATIONAL SUMMARY FOR GPS CONSTELLATION SIMULATION

T-517

<p><u>INPUT DATA</u></p> <p><math>t_0</math>: time when Greenwich meridian is along <math>x_0</math> axis</p> <p><math>t_{GPS}</math>: time when reference satellite is at ascending node</p> <p><math>\lambda_{GPS}</math>: longitude of reference satellite ascending node</p> <p><math>\Omega_{rj}</math>: relative right ascension of the <math>j^{th}</math> GPS satellite</p> <p><math>A_{rj}</math>: relative anomaly of the <math>j^{th}</math> GPS satellite</p>
<p><u>CONSTANTS</u></p> <p><math>\omega_e = 7.292115147 \times 10^{-5}</math> rad/sec</p> <p><math>\Omega_{GPS} = \lambda_{GPS} + \omega_e(t_{GPS} - t_0)</math></p> <p><math>\dot{\Omega} = -7.834 \times 10^{-9}</math> rad/sec</p> <p><math>\dot{A} = 1.4585797 \times 10^{-4}</math> rad/sec</p> <p><math>r_s = 26560387</math> m</p> <p><math>v_s = 3873.93</math> m/sec</p> <p><math>I = 55</math> deg (Block II)</p> <p><math>I = 63</math> deg (Block I)</p>
<p><u>RIGHT ASCENSION AND ANOMALY</u></p> <p><math>\Omega_j(t) = \Omega_{GPS} + \Omega_{rj} + \dot{\Omega}(t - t_{GPS})</math></p> <p><math>A_j(t) = A_{rj} + \dot{A}(t - t_{GPS})</math></p>
<p><u>INERTIAL POSITION AND VELOCITY</u></p> $(\underline{r}_j(t))_i = r_s \begin{bmatrix} C_{\Omega_j} C_{A_j} - S_{\Omega_j} C_I S_{A_j} \\ S_{\Omega_j} C_{A_j} + C_{\Omega_j} C_I S_{A_j} \\ S_I S_{A_j} \end{bmatrix}_i$ $(\underline{v}_j(t))_i = v_s \begin{bmatrix} -C_{\Omega_j} S_{A_j} - S_{\Omega_j} C_I C_{A_j} \\ -S_{\Omega_j} S_{A_j} + C_{\Omega_j} C_I C_{A_j} \\ S_I C_{A_j} \end{bmatrix}_i$

and the sine and cosine functions advance as

$$S_{(A_j+\Delta A)} = S_{A_j} C_{\Delta A} + C_{A_j} S_{\Delta A} \quad (\text{A.2-30})$$

$$C_{(A_j+\Delta A)} = C_{A_j} C_{\Delta A} - S_{A_j} S_{\Delta A} \quad (\text{A.2-31})$$

Thus, the sine and cosine of the fixed anomaly step can be computed but once, as can the sines and cosines of the initial anomalies for all the satellites. Subsequently, four multiplies and two adds serve to propagate the sine and cosine of each satellite anomaly. Another possible simplification of the simulation computations comes from the fact that the satellite anomalies of the various satellites are sometimes equal or separated by integral quadrants, making for especially simple relationships among the sines and cosines.

Besides computing the position and velocity vectors of the GPS satellites, it is sometimes desired to compute the acceleration and jerk (acceleration rate) vectors. Because of the circular orbits, the acceleration and jerk are related to the position and velocity by

$$\underline{a}_s = -\dot{A}^2 \underline{r}_s \quad (\text{A.2-32})$$

$$\underline{j}_s = -\dot{A}^2 \underline{v}_s \quad (\text{A.2-33})$$

### A.3 ANALYSIS RESULTS

Satellite visibility is a key issue which must be investigated when analyzing the ability of GPS to satisfy GGSS positioning and navigation requirements. In this section, various visibility factors are considered and analysis results are presented for the complete 18-satellite constellation.



The orbit relationships of the operational GPS constellation are presented in Section A.1. Current plans call for the GPS antenna to be mounted on the top of the aircraft fuselage. In such an arrangement, the earth is not a factor in signal blockage. In addition, while the gravity gradient data are collected during an individual survey sortie (see Fig. A-3-1 for a typical pattern), the antenna field of view is not limited. As the plane turns and banks to begin another data-gathering leg of the sortie, the wing can block the signal temporarily. However, this condition should not matter since the positioning data are not needed in this area beyond the survey region and the GGSS navigation system dynamics are being designed to recover quickly from a situation such as this.

Using the relative Block II orbit parameters listed in Table A.1-2, a GGSS user's latitude, longitude, and nominal 600 m altitude, an appropriate user elevation mask angle of

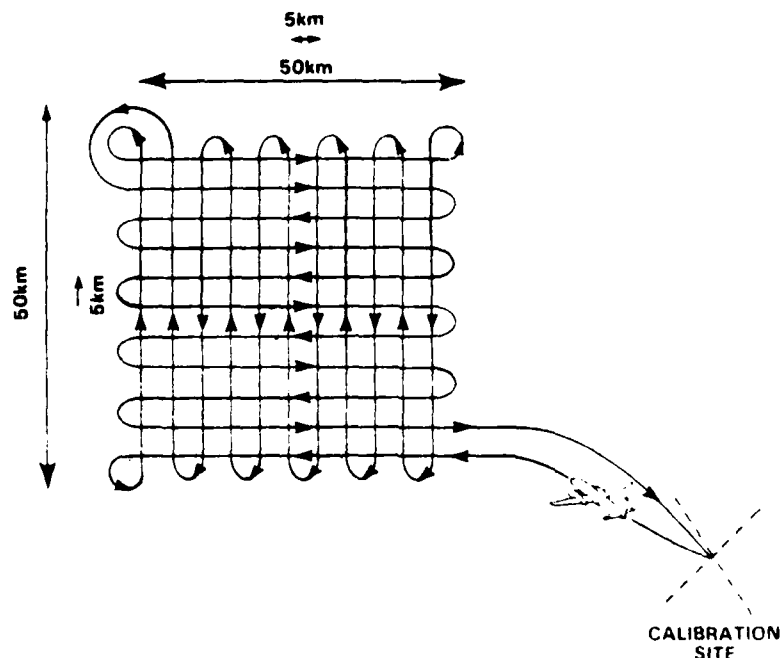


Figure A.3-1 A Proposed GGSS Survey Sortie

5 deg, and the methodology described in Section A.2 for simulating the satellite constellation, the visibility patterns and associated geometry can be determined. A typical daily pattern for a user in the continental U.S. is presented in Fig. A.3-2. Although the rising and setting times of the satellites will vary depending on the time of year and user's geodetic location, the overall pattern exhibited in this figure is common for all users. Note that for the complete constellation, at least four satellites are always visible. Thus, continuous GPS coverage can be anticipated when the full constellation is in place and operational.

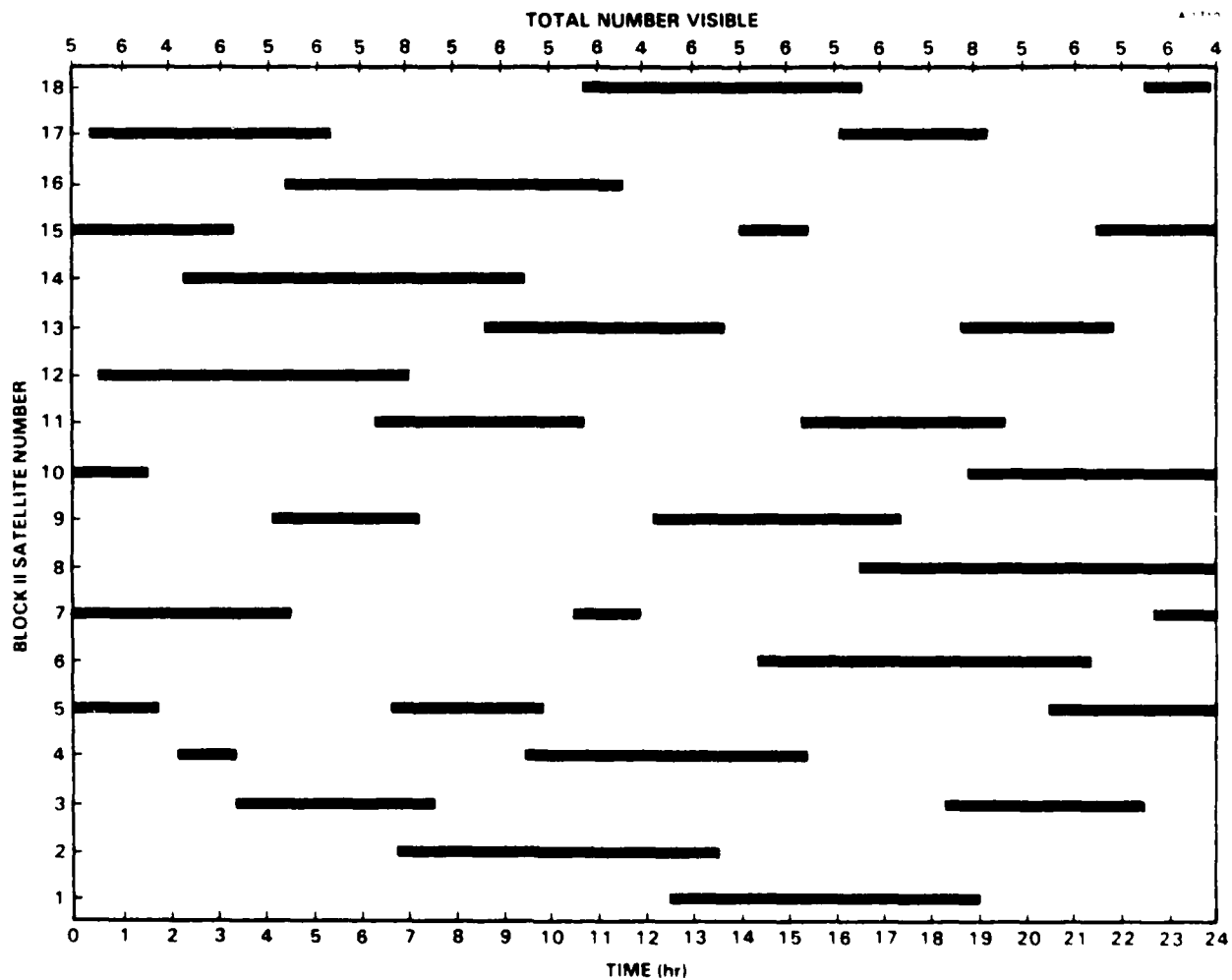


Figure A.3-2 Typical Visibility Pattern for 18-Satellite Constellation

However, to completely characterize the effectiveness of using GPS as a GGSS-aiding sensor, the geometry associated with the satellite visibility pattern must also be determined. Figure A.3-3 is a plot of the PDOP which is associated with the pattern depicted in Fig. A.3-2. Since there were several instances when more than four satellites are visible, the PDOP which reflects the selection of the four "best" satellites (i.e., those which result in the minimum value of PDOP) is plotted. The statistics (mean and standard deviation) of this curve are also indicated on the figure. Recall that the PDOP is directly proportional to the three-dimensional rms position error, i.e.,

$$\sigma_p = \text{PDOP} \times \sigma_r \quad (\text{A.3-1})$$

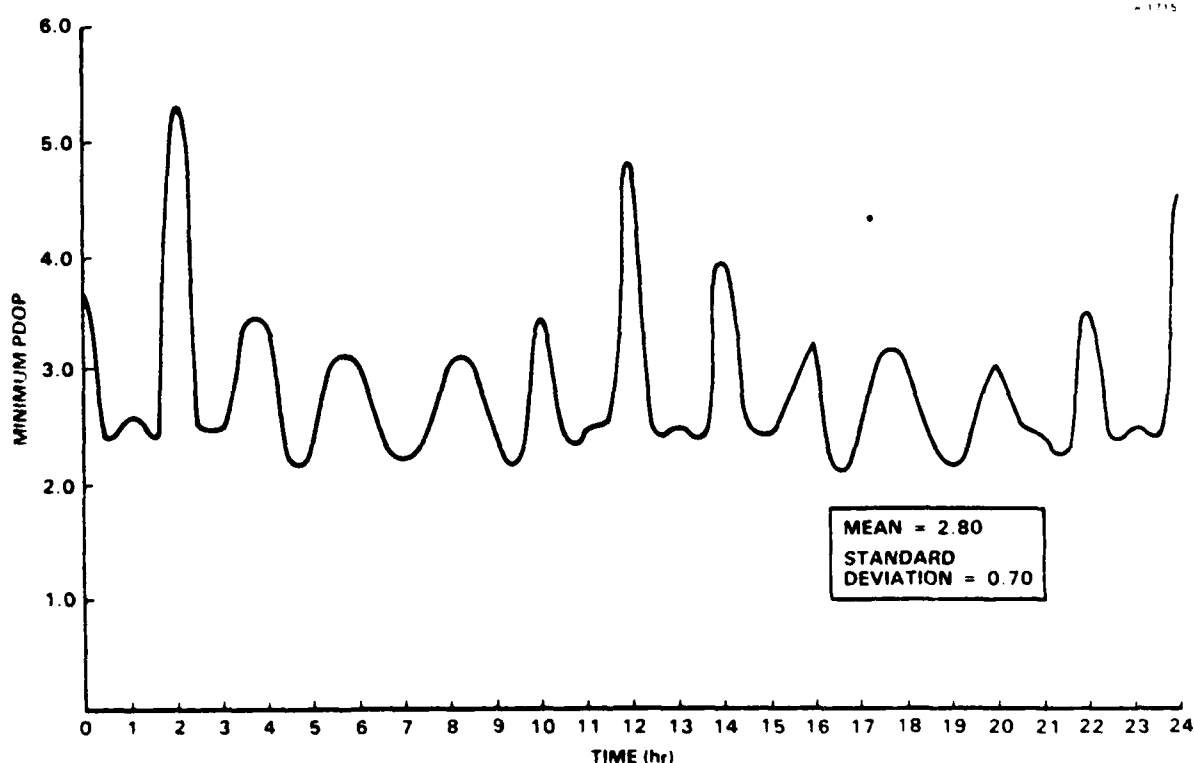


Figure A.3-3 PDOP Characteristics Associated with Visibility Pattern of Fig. A.3-2

where  $\sigma_r$  is the rms user-to-satellite range error which is commonly assumed to be 7 m. This value is consistent with test results to date (Refs. 38 and 39). Thus, for the case depicted in Fig. 2.2-3,  $\sigma_p \sim 20$  m rms which is well within the 100 m rms GGSS positioning accuracy goal identified in Section 2.1.

As pointed out in Ref. 39, a user will experience short periods of poor accuracy even with the complete 18-satellite constellation operational. These "outages" are due solely to poor geometry since at least four satellites will always be in view. Only one set of four widely separated, predictable outages exists at any time and the time duration of an outage at any of the particular locations is quite short (e.g., 5 to 20 min). The outages repeat twice a day at these locations, disappear, and then appear 40 min later at four other locations.

A composite of all outages which will occur during a given day is presented in Fig. A.3-4. For an arbitrary starting time, the set of four labeled 1 occurs first, followed 40 min later by the set designated 2, etc. Within the circled outage regions, the PDOP will be very large (on the order of thousands) and result in unacceptable four-satellite navigation accuracy levels. A plot of the PDOP for a user at one of these outage locations is presented in Fig. A.3-5. As is apparent from this figure and the included PDOP statistics, since the outage intervals are predictable and short, they are inconsequential to the currently configured GGSS.

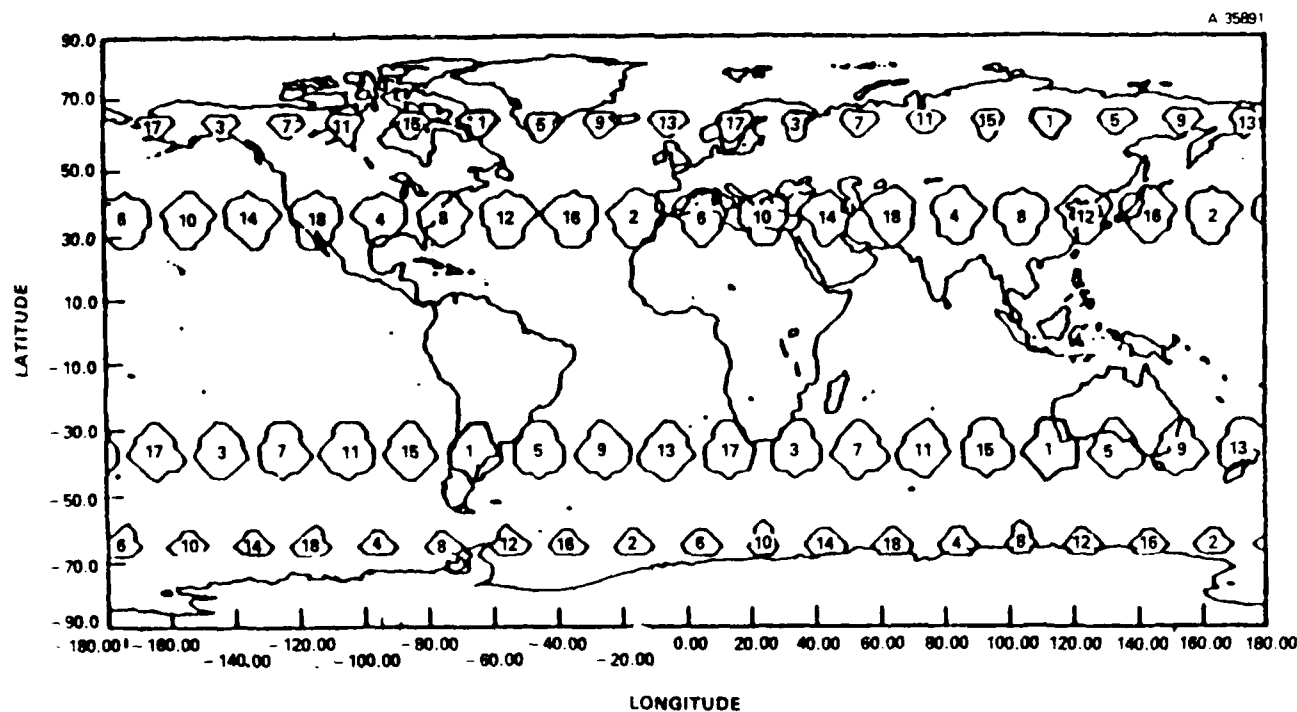


Figure A.3-4 Composite Outages for the 18-Satellite Constellation (Extracted from Ref. 39)

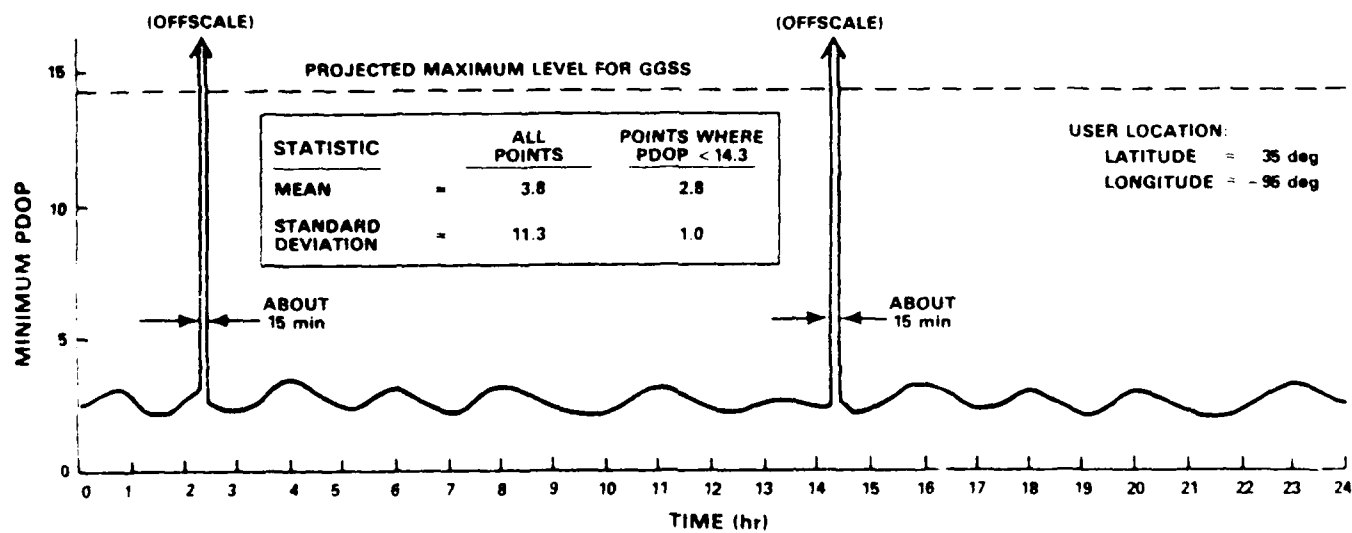


Figure A.3-5 Typical PDOP Characteristics at an Outage Location

APPENDIX B

DERIVATION OF DOPPLER-SHIFT OBSERVABLE AND ASSOCIATED  
VEHICLE ERROR DYNAMICS FOR APPLICATIONS OF  
MOVING-RECEIVER RADIO INTERFEROMETRY

B.1 INTRODUCTION

This appendix details the derivations of: 1) the doppler-shift measurement equation (Eq. 3.2-5) and 2) an expression for the vehicle velocity error (Eq. 3.4-2). Both equations depend on the basic doppler-shift definition

$$f' = f \left[ \frac{1 + nv \cos \theta / c}{1 - nv \cos \theta / c} \right]^{1/2} \quad (B.1-1)$$

where

$f'$  = doppler-shifted frequency observed at the moving-receiver

$f$  = frequency observed at the fixed-site receiver

$n$  = index of refraction

$c$  = free-space light speed

$v$  = moving-receiver velocity

$\theta$  = satellite signal incidence angle.

B.2 DERIVATION OF DOPPLER-SHIFT OBSERVABLE

Equation B.1-1 can be easily expanded using a Mac-laurin series:

$$z(x) = z(x=0) + x \left. \frac{dz}{dx} \right|_{x=0} + \frac{x^2}{2!} \left. \frac{d^2z}{dx^2} \right|_{x=0} + \dots \quad (\text{B.2-1})$$

Expanding Eq. B.1-1 in terms of  $y = v/c$  yields

$$f'(y=0) = f \quad (\text{B.2-2})$$

$$\frac{df'}{dy} = \frac{fn \cos \theta}{(1-y \cos \theta)^{3/2} (1+y \cos \theta)^{1/2}} \quad (\text{B.2-3})$$

$$\frac{d^2f'}{dy^2} = \frac{fn^2 \cos^2 \theta (1+2y \cos \theta)}{(1-y \cos \theta)^{5/2} (1+y \cos \theta)^{3/2}} \quad (\text{B.2-4})$$

Substitution of Eqs. B.2-2, B.2-3, and B.2-4 into B.2-1 leads to

$$f' = f[1 + nv \cos \theta / c + 1/2(nv \cos \theta / c)^2] + O(10^{-11}) \quad (\text{B.2-5})$$

Finally, the difference in the doppler-shift,  $\Delta f$ , as recorded at moving- and fixed-site receivers, can be written as

$$\Delta f = f' - f = \frac{fnv \cos \theta}{c} \left[ 1 + \frac{nv \cos \theta}{2c} \right] \quad (\text{B.2-6})$$

Thus, an expression for the doppler-shift difference, which is one of the observables associated with moving-receiver radio interferometry, has been derived. Note that vehicle velocity explicitly appears in this expression.

### B.3 DERIVATION OF VEHICLE ERROR DYNAMICS

Equation B.1-1 can be inverted to obtain the following relationship for vehicle velocity in terms of frequency:

$$v = \frac{c}{n \cos \theta} \left[ \frac{f'^2 + f^2}{f'^2 - f^2} \right] \quad (\text{B.3-1})$$

Following a first-order perturbation of Eq. B.3-1, the error in velocity can be written as

$$\delta v = - \left( \frac{v}{n} \right) \delta n + v \tan \theta \delta \theta + \frac{4 f f' c}{n \cos \theta (f'^2 - f^2)} \delta f \quad (\text{B.3-2})$$

Note that the last term in Eq. B.3-2 can also be written in terms of velocity; hence

$$\delta v = \delta \dot{p} = - \left( \frac{v}{n} \right) \delta n + v \tan \theta \delta \theta + \frac{v [c^2 - (n v \cos \theta)^2]}{f (c n \cos \theta)} \delta f \quad (\text{B.3-3})$$

Letting  $\xi = [c^2 - (n v \cos \theta)^2] / (c n \cos \theta)$ , Eq. B.3-3 can be rewritten as

$$\delta \dot{p} = - \left( \frac{v}{n} \right) \delta n + v \tan \theta \delta \theta + \left( \frac{\xi v}{f} \right) \delta f \quad (\text{B.3-4})$$

Equation B.3-4 provides the relationship between the time rate of change of position error ( $\delta \dot{p}$ ), vehicle velocity, and measured values of refractivity, incidence angle, and signal frequency.



APPENDIX C  
ATMOSPHERIC PROPAGATION DELAY

C.1 BACKGROUND

Passage of electromagnetic waves through the atmosphere is described by the branch of wave mechanics known as geometrical optics. In this field of science, electromagnetic energy is transported along light rays and the velocity propagation of these rays is described by

$$v = c/n \qquad (C.1-1)$$

where  $n$  is the index of refraction and  $c$  is the free-space light speed ( $2.9978 \times 10^8$  m/sec). Depending on the dielectric properties of the medium, the refractive index is greater than or less than unity.

The dielectric properties of the atmosphere produce refractive indices which are very region-dependent. The lower 40 km (called the troposphere) consists of isotropic, neutral gases which yield a refractive index greater than unity and which is independent of wave polarization or propagation direction. The upper atmosphere (collectively termed the ionosphere) comprises anisotropic, charged gases which produce two refractive indices (both less than unity) and two characteristic polarizations. The values of the indices and polarizations depend on the wave propagation direction.

A change in the atmospheric refractive index of only a few parts per million can have a significant effect on radio-waves. Since refractive values are very near unity (typically

$n = 1.00035$ ) meteorologists have defined the term refractivity,  $N$ , to be

$$N = (n-1) \times 10^6 \quad (C.1-2)$$

The means by which atmospheric properties are measured to yield refractivity is the subject of this Appendix. Section C.2 describes the methods employed in recording tropospheric refractivity; Section C.3 details the physics of ionospheric signal delay; and Section C.4 describes methods to correct for ionospheric refraction.

## C.2 TROPOSPHERIC REFRACTIVITY

It is in the troposphere that changes of temperature, humidity, and pressure, as well as clouds and rain, influence the way in which radio waves propagate. Spot measurements of the tropospheric refractive index are made using a variety of application-dependent techniques.

For airborne GGSS survey monitoring, ruggedness, repeatability without frequent calibration, and a wide range of sensor response are more important than high accuracy. If a system is needed to measure rapid index fluctuations (at a rate of several tens of Hertz), only instruments which record the refractive index directly have an adequate speed of response; such instruments are referred to as "refractometers." If a lower sampling rate can be permitted, or a lightweight system is essential, the refractive index can be determined indirectly through measurements of atmospheric properties.

Microwave refractometers are the most common means of measuring the refractive index directly. The principle of

operation is to measure the change in the resonant frequency,  $\delta f$ , of a cavity with partly open ends. This change occurs due to a variation in the refractive index of the air passing through the cavity. Then, for a fixed cavity, the index variation,  $\delta n$ , is

$$\delta n = -\delta f/f \quad (C.2-1)$$

Refractometers have been used successfully since 1950 in aircrafts, on tall masts, and suspended from tethered balloons. With solid-state circuitry and solid-state microwave sources, the weight of the sensors has been substantially reduced and the short-term errors have been lowered to typically less than 0.01 N-unit. Stability of one part in  $10^7$  per month has been reported (Ref. 45).

Measurement of temperature, water vapor content, and air pressure can also be used to determine refractivity indirectly. The empirical formula relating these quantities to the refractive index is (Ref. 20)

$$N = 77.6 P/T + 3.73 \times 10^5 e/T^2 \quad (C.2-2)$$

where  $P$  is the total air pressure (in mbar),  $e$  is the partial pressure of water vapor (in mbar), and  $T$  is the temperature (in Kelvin). This equation has an inherent accuracy of  $\pm 0.5$  percent for atmospheric pressures between 200 and 1100 mbar, air temperatures between 240 and 310 K, water vapor pressures less than 30 mbar, and radio frequencies less than 30 GHz. For GPS applications (with a maximum frequency of 1.5754 GHz), typical atmospheric conditions near ground are  $P = 1000$  mbar,  $T = 288$  K, and  $e = 11.9$  mbar (which implies 70% humidity).

Conventional radiosondes, as used for weather forecasting, have been developed as moderately robust, low-cost,

throw-away devices to measure pressure, temperature, and humidity at heights up to 40 km. However, the sensitivities and rapidity of response are often inadequate for radio-meteorological studies. This has prompted the development of specialized radiosondes which are suspended below tethered or free balloons. Many of these sondes have employed direct measurement of dewpoint temperatures to achieve rms refractivity errors as low as 1 N-unit, with 1.3-second time constants (Ref. 20).

An important point to remember about radiosonde measurements of the refractive index is the local nature of the recordings; both types of sensors record the atmosphere in the vicinity of the monitor. However, refractivity varies with altitude as well as with horizontal distance separation. Until recently, this contribution to tropospheric signal delay was compensated only by approximate modeling. Water-vapor radiometers now exist which can measure the delay time directly.

Dual-frequency microwave radiometers measure the thermal atmospheric emission at 22.2 GHz (for water vapor resonance) and 31.4 GHz (for liquid water contribution) to determine the line-of-sight signal path delay. These instruments have been used successfully in the Crustal Dynamics Program (Ref. 26) and in NGS tests at Boulder, Colorado (Ref. 27). While current radiometers are not portable, ongoing research at JPL involves developing a lightweight, easily movable version. A prototype version is anticipated soon.

### C.3 IONOSPHERIC REFRACTIVITY

The refractive index of the upper atmosphere is a function of radio frequency and free-electron density. Using magneto-ionic theory (Ref. 46) a relationship can be derived between  $n$  and the radio frequency  $f$ :

$$n_{\ell,r} = [1 - f_p^2/(f^2 \pm f f_g |\cos \theta|)]^{1/2} \quad (C.3-1)$$

where

$f_p$  = plasma frequency;  $f_p = AN_e$

$A = 80.6 \text{ m}^3/\text{sec}^2$

$N_e$  = number density of free electrons ( $\text{m}^3$ )

$f_g$  = frequency of gyration (gyro frequency) of free electrons;  $f_g = eB/(2\pi m)$

$B$  = geomagnetic induction ( $\text{v-sec}/\text{m}^2$ )

$\theta$  = angle between the phase propagation and geomagnetic induction vectors.

The positive sign corresponds to the left-handed ( $\ell$ -subscripted) circular component of polarization in the northern geomagnetic hemisphere. Expanding the square root in Eq. C.3-1 leads to

$$\begin{aligned} n_{\ell,r} = 1 - f_p^2/(2f^2) \pm f_p^2 f_g |\cos \theta|/f^3 - f_p^4/(8f^4) \\ - f_p^2 f_g^2 (\sin^2 + 2\cos^2 \theta)/(4f^4) \pm \dots \end{aligned} \quad (C.3-2)$$

which is complete to order  $(1/f^4)$ .

Equation C.3-2 can be separated into angular and non-angular dependent terms. The two angular-dependent terms account for the effect of wave propagation in the geomagnetic field and are functions of electron content and signal polarization. (Circular polarization yields the extreme positive or negative values of the  $1/f^3$  term.)

Plasma modeling of the ionosphere is required to evaluate accurately Eq. C.3-2. This modeling requires definition of the "effective electron thickness,"  $\tau$ . In terms of the electron density,  $N_m$ ,

$$\tau = \int_0^{h_s} N_e dh / N_m = I / N_m \quad (C.3-3)$$

where  $h_s$  is the altitude of the satellite,  $I$  is the total electron content, and  $N_e$  is the number density of free electrons. This last parameter is a function of geographic and geomagnetic coordinates, solar activity, season, time of day, and geomagnetic activity;  $N_e$  varies from  $1 \times 10^{16} \text{ m}^{-2}$  to  $2 \times 10^{18} \text{ m}^{-2}$ . The uniformity or "shape" of the electron content can be modeled by

$$y = \frac{1}{\tau} \int_0^{h_s} \left( \frac{N_e}{N_m} \right)^2 dh \quad (C.3-4)$$

In general, it is not possible to gain accurate information on the height distribution of free electrons and the "worst-case" scenario implies a shape factor of  $y = 1$ , i.e., a uniform electron density throughout the ionosphere with a thickness of  $\tau = 200 \text{ km}$  (Ref. 47).

The delay of electromagnetic signals propagating through the ionosphere is directly related to the medium's refractive index. For radio signals of  $f = 2 \text{ GHz}$  propagating along the direction of geomagnetic induction (i.e.,  $\theta = 0$ ), the associated ionospheric range errors are:

$$1 - f_p^2 / (2f^2) = 20.15 \text{ m} \quad (C.3-5)$$

$$f_p^2 f_g |\cos \theta| / f^3 = 2.82 \times 10^{-2} \text{ m} \quad (C.3-6)$$

$$f_p^4/(8f^4) = 1.01 \times 10^{-3} \text{m} \quad (\text{C.3-7})$$

$$f_p^2 f_g^2 (\sin^2 \theta + 2 \cos^2 \theta)/(4f^4) = 9.87 \times 10^{-6} \text{m} \quad (\text{C.3-8})$$

Because the first-order contribution to the ionospheric range error is four orders of magnitude greater than the next correction term, the first-order ( $1/f^2$ ) contribution to the ionospheric range error is a sufficient approximation for a radio interferometric system operating in the gigahertz frequencies.

#### C.4 CORRECTIONS FOR IONOSPHERIC REFRACTIVITY DELAYS

To correct for the delay of electromagnetic signals propagating through the ionosphere, upper atmospheric modeling or dual-frequency measurements can be used. Modeling the ionosphere, as noted in the previous section, requires well-studied and predictable electron behavior. In the northern mid-latitude regions, the ionosphere has been exhaustively researched and is better understood than the polar or equatorial areas. Thus, in these well-studied areas, signal delay can be reduced by 50 to 70 percent compared with uncorrected measurements, on an rms basis. Alternatively, since the delay is proportional to the inverse square of the signal frequency, two frequencies, transmitted coherently and sufficiently far apart, can also be used to reduce the ionospheric delay. The remainder of this section addresses the uncertainty associated with this method.

The signal path difference,  $p$ , which is used to determine the relative receiver distance, is shown in Fig. C.4-1. Measurement of this difference yields

$$m_i = p + d + (K/f_i^2) + n_i \quad (\text{C.4-1})$$

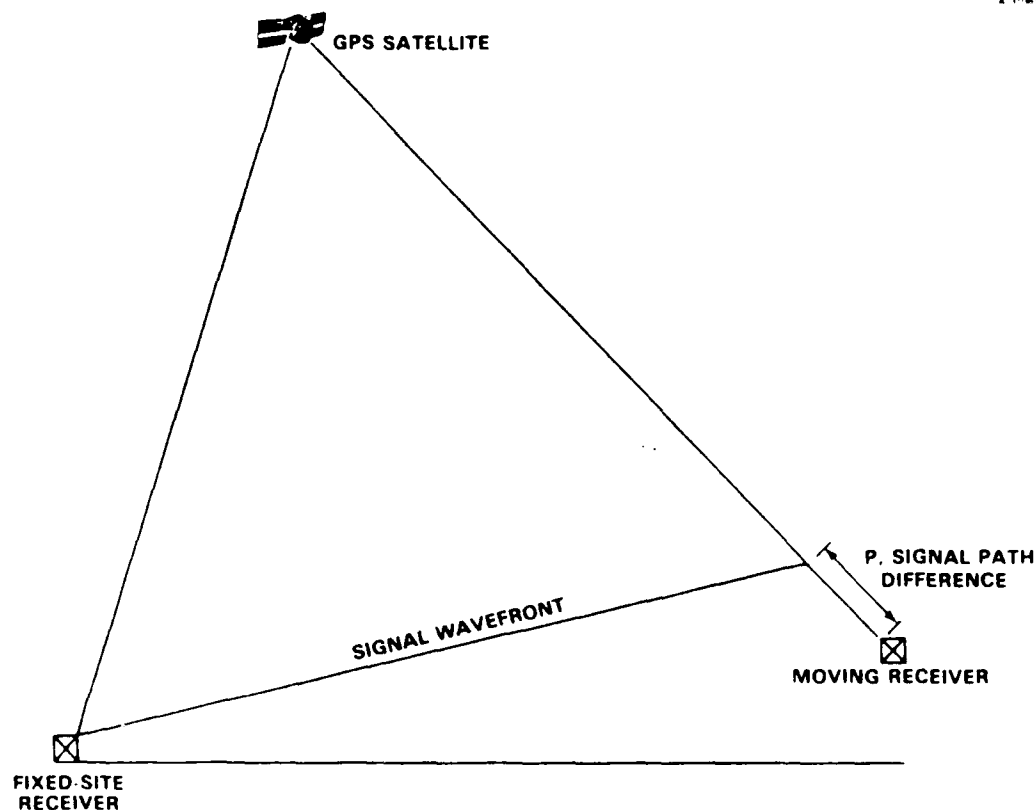


Figure C.4-1 Interferometric Signal Path Difference

where

$m_i$  = signal path difference measurement using channel  $i$

$d$  = tropospheric and mechanical uncertainties,  
independent of frequency and receiver noise

$K$  = parameter proportional to the difference in the  
total electron content along the signal paths

$f_i$  = signal frequency of channel  $i$

$n_i$  = receiver noise in channel  $i$ .



Tropospheric and mechanical uncertainties are ignored in this discussion. Measurement in two channels yields an equation for the true signal path difference

$$p = (m_i - n_i) + f_2^2[(m_1 - n_1) - (m_2 - n_2)]/(f_1^2 - f_2^2) \quad (C.4-2)$$

The second term in Eq. C.4-2 stems from the algebraic elimination of  $K$ , whereas the first term is the single-channel difference measurement uncorrected for ionospheric delays. The receiver noise,  $n_i$ , is an unknown by definition, so the estimate of the true path difference is

$$\hat{p} = m_i + f_2^2(m_1 - m_2)/(f_1^2 - f_2^2) \quad (C.4-3)$$

and the error in this estimate is given by

$$\delta p = \hat{p} - p = n_i + f_2^2(n_1 - n_2)/(f_1^2 - f_2^2) \quad (C.4-4)$$

If the receiver noise,  $n_i$ , in both receivers' channels have equal standard deviations,  $\sigma_n$ , and correlation factor  $\rho$ , then the standard deviation in the signal path difference error is

$$\begin{aligned} \sigma &= \sigma_n [f_2^4 + f_1^4 - 2\rho f_1^2 f_2^2]^{1/2} \\ &= \sigma_n \{1 + [\sqrt{2} f_1 f_2 / (f_2^2 - f_1^2)]^2 (1 - \rho)\}^{1/2} \end{aligned} \quad (C.4-5)$$

The first term in the braces of Eq. C.4-5 represents the single-channel contribution to the measurement error. The second term arises from the ionospheric calibration process. Figure C.4-2 is a plot of the signal path difference error estimate,  $\delta p$ , as well as the standard deviation in the signal path difference error estimate given by Eq. C.4-5 for the case involving uncorrelated channels. Using the current GPS transmitted frequencies, the total receiver measurement error is

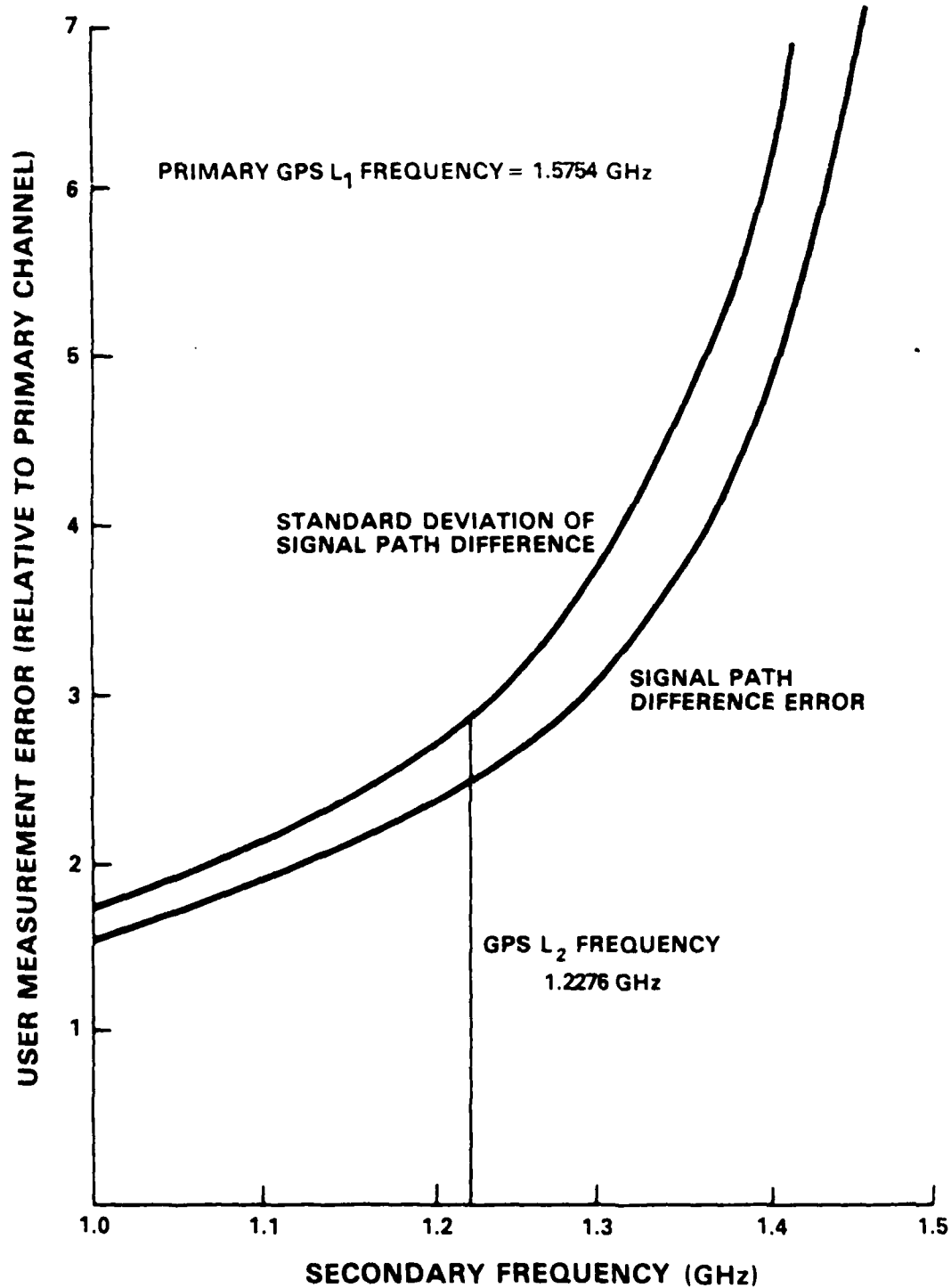


Figure C.4-2 Frequency Dependence of Receiver Measurement Error

approximately three times the single-channel receiver noise. Although the ionospheric delay is not exactly proportional to the wavelength squared, higher-order terms constitute a negligible source of error (see Section C.1). Ionospheric signal delay error will not contribute to radio interferometric measurement errors until the inter-receiver distances are large enough to cause two distinct signal paths from satellite to receivers (receiver separations are greater than 1000 km). For these very long distances, dual-frequency receivers will offer corrections to the signal delay; the error associated with the corrections is given by Eq. C.4-5.

APPENDIX D  
THIRD-ORDER MARKOV PROCESSES FOR  
ATMOSPHERIC REFRACTIVITY MODELING

D.1 INTRODUCTION

Since the lower atmosphere is not static, any tropospheric model is geographically localized. A first approximation to tropospheric modeling requires exponential correlation of site atmospheric conditions. A third-order Markov process was selected to model tropospheric refractivity effects at varying distances from a weather monitor station. This choice was made to ensure distance correlation of atmospheric conditions after double-differentiation of inter-receiver length: i.e., to obtain acceleration. For completeness, a full derivation of the state-space representation for a third-order Markov process and the associated covariance matrices is presented. The dynamics matrix is derived in Section D.2; Sections D.3 and D.4 define the spectral density and initial covariance matrices, respectively.

D.2 DERIVATION OF THE DYNAMICS MATRIX

The autocorrelation function for a critically damped third-order Markov process is given by (Ref. 22)

$$\phi(\tau) = \sigma^2 e^{-\beta\tau} [1 + \beta\tau + (\beta\tau)^2/3] \quad (D.2-1)$$

where

$\sigma$  = rms error

$\beta$  = correlation time

$\tau$  = time-shift parameter.

A linear, state-space model which generates the random process with the correlation process defined by Eq. D.2-1 has the following form:

$$\dot{\underline{x}} = \underline{F}\underline{x} + \underline{w} \quad (\text{D.2-2})$$

where

$\underline{x}$  = state vector

$\underline{F}$  = dynamics matrix

$\underline{w}$  = vector of zero-mean, white-noise elements.

To derive the state-space form for the third-order Markov process, begin by defining a variable  $x_1$  as

$$x_1 = e^{-\beta\tau} [1 + \beta\tau + (\beta\tau)^2/3] \quad (\text{D.2-3})$$

Taking the first derivative of  $x_1$  (with respect to  $\tau$ ) yields:

$$\dot{x}_1 = -\beta e^{-\beta\tau} [\beta\tau/3 + \beta^2\tau^2/3] \quad (\text{D.2-4})$$

For convenience, a variable  $x_2$  can be defined as

$$x_2 = \dot{x}_1/\beta \quad (\text{D.2-5})$$

and thus,

$$x_2 = -e^{-\beta\tau} [\beta\tau/3 + \beta^2\tau^2/3] \quad (\text{D.2-6})$$

Equation D.2-6 can be rewritten in terms of  $x_1$  by replacing the  $\tau^2$  term with an equivalent expression obtained from Eq. D.2-3. Thus,

$$x_2 = -x_1 + e^{-\beta\tau} [1 + 2\beta\tau/3] \quad (\text{D.2-7})$$

The derivative (again with respect to  $\tau$ ) of  $x_2$  yields:

$$\dot{x}_2 = -\dot{x}_1 - \beta e^{-\beta\tau} [1/3 + 2\beta\tau/3] \quad (D.2-8)$$

A new variable,  $x_3$ , can be defined as

$$x_3 = \dot{x}_2/\beta \quad (D.2-9)$$

so that

$$x_3 = -\dot{x}_1/\beta - e^{-\beta\tau} [1/3 + 2\beta\tau/3] \quad (D.2-10)$$

Rewriting Eq. D.2-10 explicitly in terms of  $x_2$  and  $x_1$  results in

$$x_3 = -x_1 - 2x_2 + 2e^{-\beta\tau}/3 \quad (D.2-11)$$

where use has been made of Eq. D.2-5 and an equivalent expression for the  $\tau$  term was obtained by rearranging Eq. D.2-7.

The time derivative of  $x_3$  is given as

$$\dot{x}_3 = -\dot{x}_1 - 2\dot{x}_2 - 2\beta e^{-\beta\tau}/3 \quad (D.2-12)$$

or equivalently,

$$\dot{x}_3 = -\beta x_1 - 3\beta x_2 - 3\beta x_3 \quad (D.2-13)$$

after substituting the appropriate expressions for  $\dot{x}_1$ ,  $\dot{x}_2$ , and  $2e^{-\beta\tau}/3$  from Eqs. D.2-5, D.2-9, and D.2-11, respectively.

Finally arranging Eqs. D.2-5, D.2-9, and D.2-13 in the form of D.2-2 results in

$$\begin{bmatrix} \dot{x}_1 \\ \dot{x}_2 \\ \dot{x}_3 \end{bmatrix} = \beta \begin{bmatrix} 0 & 1 & 0 \\ 0 & 0 & 1 \\ -1 & -3 & -3 \end{bmatrix} \begin{bmatrix} x_1 \\ x_2 \\ x_3 \end{bmatrix} \quad (\text{D.2-14})$$

where the dynamics matrix is given by

$$F = \beta \begin{bmatrix} 0 & 1 & 0 \\ 0 & 0 & 1 \\ -1 & -3 & -3 \end{bmatrix} \quad (\text{D.2-15})$$

The block diagram representation for this third-order Markov process model is presented in Fig. D.2-1.

A 31059

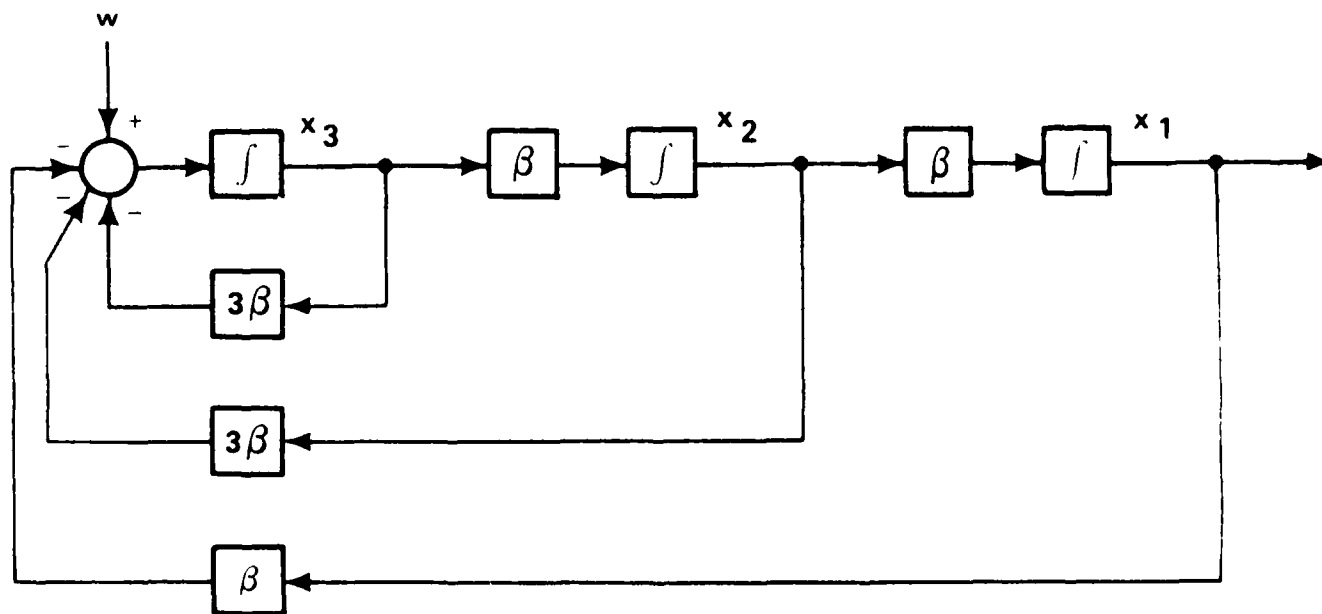


Figure D.2-1 Third-Order Markov Process Model

### D.3 THE SPECTRAL DENSITY MATRIX

The white-noise vector,  $\underline{w}$ , from Eq. D.2-2 has a spectral density matrix  $Q$  defined by

$$E[\underline{w}(t)\underline{w}(\tau)] = q \delta(t-\tau) \quad (D.3-1)$$

where  $\delta(\cdot)$  is the Dirac delta function; i.e.,  $Q$  is diagonal. An appropriate expression for  $Q$  can be written as (Ref. 22)

$$Q = \beta \sigma_x^2 \begin{bmatrix} 0 & 0 & 0 \\ 0 & 0 & 0 \\ 0 & 0 & 16 \end{bmatrix} \quad (D.3-2)$$

### D.4 INITIALIZATION OF THE COVARIANCE MATRIX

The covariance of the state vector, denoted by  $P$ , is governed by the differential equation

$$\dot{P} = FP + PF^T + Q \quad (D.4-1)$$

where superscript  $T$  indicates the matrix transpose operator. In steady-state,  $\dot{P} = 0$ . Hence, defining  $P$  as

$$P = \sigma^2 \begin{bmatrix} a & b & c \\ d & e & f \\ g & h & i \end{bmatrix} \quad (D.4-2)$$



in steady state, Eq. D.4-1 yields

$$0 = \begin{bmatrix} d & e & f \\ g & h & i \\ -(a+3d+3g) & -(b+3e+3h) & -(c+3f+3i) \end{bmatrix} + \begin{bmatrix} b & b & -(a+3b+3c) \\ e & f & -(d+3e+3f) \\ h & i & -(g+3h+3i) \end{bmatrix} + Q \quad (\text{D.4-3})$$

Solving the linear equations of D.4-3 simultaneously results in

$$P_O = \sigma^2 \begin{bmatrix} 3 & 0 & -1 \\ 0 & 1 & 0 \\ -1 & 0 & 3 \end{bmatrix} \quad (\text{D.4-4})$$

## REFERENCES

1. Heller, W.G., and Shipp, R.F., "Airborne Gravity Gradiometer Survey System Aided by a High-Accuracy Master Inertial Navigation System," The Analytic Sciences Corporation, Technical Report TR-4769-1, May 1984.
2. Elson, B.M., "Transoceanic Flight Shows GPS Uses," Aviation Week & Space Technology, 25 July 1983, pp. 45-48.
3. Wooden, W.H., "NAVSTAR Global Positioning System: 1985," Proceedings First International Symposium on Precise Positioning with the Global Positioning System, Rockville, MD, April 1985, pp. 23-32.
4. Eckhardt, D.H., "Global Positioning System - Geodetic Applications," Air Force Geophysics Laboratory, Report No. AFGL-TR-84-0209, August 1984, ADA144904.
5. Parkinson, B.W., and Gilbert, S.W., "NAVSTAR: Global Positioning System - Ten Years Later," Proceedings of the IEEE, Vol. 71, No. 10, October 1983, pp. 1177-1186.
6. Milliken, R.J., and Zoller, C.J., "Principle of Operation of NAVSTAR and System Characteristics," Global Positioning System: Papers Published in Navigation, The Institute of Navigation, Washington, D.C., 1980, pp. 3-14.
7. Henson, D.J., Collier, E.A., and Schneider, K.R., "Geodetic Applications of the Texas Instruments TI 4100 GPS Navigator," Proceedings First International Symposium on Precise Positioning with the Global Positioning System, Rockville, MD, April 1985, pp. 191-200.
8. Bossler, Rear Admiral J.D., and Challstrom, C.W., "GPS Instrumentation and Federal Policy," Proceedings First International Symposium on Precise Positioning with the Global Positioning System, Rockville, MD, April 1985, pp. 1-10.
9. Goad, C.C., Sims, M.L., and Young, L.E., "A Comparison of Four Precise Global Positioning System Geodetic Receivers," IEEE Transactions on Geoscience and Remote Sensing, Vol. GE-23, No. 4, July 1985, pp. 458-466.

#### REFERENCES (Continued)

10. Heller, W.G., and Shipp, R.F., "Gravity Gradiometer Mapping System Platform Performance," American Geophysical Union Spring Meeting, Baltimore, MD, The Analytic Sciences Corporation, Slide Presentation SP-4423-2, June 1983.
11. Farr, J.E., "Space Navigation Using the NAVSTAR Global Positioning System (GPS)," Guidance and Control 1979, Volume 39, Advances in the Astronautical Sciences, American Astronautical Society, 1979.
12. Seeber, G., Egge, D., Schuohardt, A., Siebold, J., and Wuebbena, G., "Experiences with TI 4100 NAVSTAR Navigator at the University of Hanover," Proceedings First International Symposium on Precise Positioning with the Global Positioning System, Rockville, MD, April 1985, pp. 215-225.
13. Bock, Y., "Centimeter-Level Baseline Estimation with GPS Interferometry," Marine Geodesy, Vol. 9, No. 2, May 1985, pp. 187-197.
14. Bock, Y., Abbot, R.I., Counselman, C.C., Gourevitch, S.A., King, R.W., and Paradis, A.R. "Geodetic Accuracy of the Macrometer Model V-1000," Bulletin Geodesique, Vol. 58, 1984, pp. 211-221.
15. Goad, C., and Remondi, B., "Initial Relative Positioning Results Using the Global Positioning System," Bulletin Geodesique, Vol. 58, 1984, pp. 193-210.
16. Brzezowski, S.J., "Recommended Acceptance Test Procedures for the Surface and Airborne Gravity Gradiometer Survey System (GGSS)," The Analytic Sciences Corporation, Technical Information Memorandum TIM-4423-7, May 1985.
17. MacDoran, P.F., Miller, R.B., Buennagel, L.A., and Whitcomb, J.H., "Codeless System for Positioning with NAVSTAR-GPS," Proceedings First International Symposium on Precise Positioning with the Global Positioning System, Rockville, MD, April 1985, pp. 181-190.
18. Ladd, J.W., Counselman, C.C., and Gourevitch, S.A., "The Macrometer II Dual-Band Interferometric Surveyor," Proceedings First International Symposium on Precise Positioning with the Global Positioning System, Rockville, MD, April 1985, pp. 175-180.

# REFERENCES (Continued)

19. Delikaroglou, D., Beck, N., McArthur, D., and Lockhead, K., "On the Establishment of 3-D Geodetic Control by Interferometry with the TI 4100 GPS Receiver," Proceedings First International Symposium on Precise Positioning with the Global Positioning System, Rockville, MD, April 1985, pp. 645-656.
20. Hall, M., Effects of the Troposphere on Radio Communication, The Institute of Electrical and Electronic Engineers, New York, 1979.
21. Mealy, G., "Sensor Data Bank Development: Time Standard Error Models and Data File," The Analytic Sciences Corporation, Report No. AFAL-TR-75-65, 1975.
22. Gelb, A., ed., Applied Optimal Estimation, MIT Press, Cambridge, MA, 1974.
23. Hewlett-Packard Measurement Computations Systems, Hewlett-Packard Co., 1985.
24. McCaskill, T., and Buisson, J., "On-Orbit Frequency Stability Analysis of NAVSTAR GPS Clocks and the Importance of Frequency Stability to Precise Positioning," Proceedings First International Symposium on Precise Positioning with the Global Positioning System, Rockville, MD, April 1985, pp. 37-50.
25. Martin, E.H., "GPS User Equipment Error Models," Global Positioning System: Papers Published in Navigation, The Institute of Navigation, Washington, D.C., 1980, pp. 109-118.
26. Janssen, M., "A New Instrument for the Determination of Radio Path Delay Due to Atmospheric Water Vapor," IEEE Transactions on Geoscience and Remote Sensing, GE-23, 1985, pp. 485-490.
27. Ware, R.H., Rocken, C., and Snider, J.B., "Experimental Verification of Improved GPS-Measured Baseline Repeatability Using Water Vapor Radiometer Corrections," IEEE Transactions on Geoscience and Remote Sensing, GE-23, 1985, pp. 467-473.

# REFERENCES (Continued)

28. Bock, Y., Abbot, R.I., Counselman, C.C., King, R.W., and Gourevitch, S.A., "Three-Dimensional Geodetic Control By Interferometry with GPS: Processing of GPS Phase Observables," Proceedings First International Symposium on Precise Positioning with the Global Positioning System, Rockville, MD, April 1985, pp. 255-262.
29. Brozena, J.M., "A Preliminary Analysis of the NRL Airborne Gravimetry System," Geophysics, Vol. 49, No. 7, July 1984, pp. 1060-1069.
30. Gumert, W.R., Wertz, G.F., and Iverson, R.M., "An Application Study for Using Differential GPS in Airborne Gravity Surveying," Proceedings First International Symposium on Precise Positioning with the Global Positioning System, Rockville, MD, April 1985, pp. 829-832.
31. Hammer, S., "Airborne Gravity Is Here," Geophysics, Vol. 48, No. 2, February 1983, pp. 213-223.
32. Telford, W.M., Geldart, L.P., Sheriff, R.E., and Keys, D.A., Applied Geophysics, Cambridge University Press, 1976, pp. 31-43.
33. Bell, R., and Watts, A.B., "Evaluation of the BGM-3 Marine Gravity Meter System," American Geophysical Union Spring Meeting, Baltimore, MD, May 1985.
34. Goldstein, J.D., "Analysis and Simulation of Multisensor Gravity Surveys, Vol. I," The Analytic Sciences Corporation, Technical Report TR-4423-4 (AFGL-TR-81-0018(I)), December 1980, modified April 1985, ADA160388.
35. White, J.V., "A Statistical Gravity Model for Northern Texas," The Analytic Sciences Corporation, Technical Information Memorandum TIM-4423-5 (AFGL-TR-85-0037), November 1984, ADA160474.
36. Brzezowski, S.J., "Gravity Gradiometer Survey Errors," The Analytic Sciences Corporation, Technical Report TR-4423-3 (AFGL-TR-85-0066), March 1985. ADA165575
37. Kruh, P., Brady, W.F., and Schmitt, D.L., "A Strategy for Buildup to the Operational NAVSTAR GPS Constellation," Institute of Navigation National Aerospace Meeting, March 1983, pp. 43-48.

# REFERENCES (Continued)

38. Brady, W.F., and Jorgensen, P.S., "Worldwide Coverage of the Phase II NAVSTAR Satellite Constellation," Institute of Navigation National Aerospace Meeting, Travose, PA, April 1981.
39. Kruh, P., "The NAVSTAR Global Positioning System Six-Plane, 18-Satellite Constellation," NTC Record-1981, New Orleans, LA, November 1981, pp. E9.3.1-8.
40. Spilker, J.J., Jr., "GPS Signal Structure and Performance Characteristics," Global Positioning System: Papers Published in Navigation, The Institute of Navigation, Washington, D.C., 1980, pp. 29-54.
41. Sturza, M.A., "GPS Navigation Using Three Satellites and a Precise Clock," Navigation: Journal of the Institute of Navigation, Vol. 30, No. 2, 1983, pp. 146-156.
42. Van Dierendonck, A.J., and Melton, W.C., "Application of Time Transfer Using NAVSTAR GPS," Navigation: Journal of the Institute of Navigation, Vol. 30, No. 2, 1983, pp 157-170.
43. Macdonald, T.J., Matchett, G.A., and Myers, W.L., "Integrated Navigation System Simulation, Volume II: Technical Appendices," Technical Report AFWAL-TR-85-1088, October 1985.
44. Kaula, W.H., Theory of Satellite Geodesy, Blaisdell, 1966.
45. Vetter, M., and Thompson, M., "Direct Reading Microwave Refractometer with Quartz-Crystal Reference," IEEE Transactions on Information Management, IM-20, 1971, pp. 58-62.
46. Jackson, J.D., Classical Electrodynamics, 2nd. Edition, John Wiley and Sons, Inc., New York, 1975.
47. Risbeth, H., and Garriot, D., Introduction to Ionospheric Physics, Academic Press, New York, 1969.

END

DTIC

9-86